

IN-07  
63546

# Heat Transfer Experiments in the Internal Cooling Passages of a Cooled Radial Turbine Rotor

B.V. Johnson and J.H. Wagner  
*United Technologies Research Center  
East Hartford, Connecticut*

May 1996

Prepared for  
Lewis Research Center  
Under Contract NAS3-25952



National Aeronautics and  
Space Administration

## **FOREWORD**

This report covers work performed under NASA Contract NAS-25952 to investigate heat transfer characteristics of rotating coolant passages of a cooled radial turbine rotor. The NASA Program Manager is Kestutis Civinskas, NASA Lewis Research Center. Seyf Tanrikut served as the Technical Program Manager at Pratt & Whitney. Acknowledgments are given to S. Orr, J. Nycz, and the assistance of colleagues at Pratt & Whitney and UTRC for their contributions to the program.



# **HEAT TRANSFER EXPERIMENTS IN THE INTERNAL COOLING PASSAGES OF A COOLED RADIAL TURBINE ROTOR**

## **TABLE OF CONTENTS**

	<u>Page</u>
1.0 Summary	1
2.0 Introduction	2
2.1 Background	2
2.2 Objectives	3
3.0 Description of Apparatus and Experiment	6
3.1 Heat Transfer Model	6
3.2 Model Instrumentation	7
3.3 Rotating Heat Transfer Facility	11
3.4 Experimental Procedures	16
4.0 Experimental Parameters and Test Matrix	27
4.1 Flow Parameters	27
4.2 Geometric Parameters	28
4.3 Test Conditions	28
4.4 Outline for Presentation of Results	31
5.0 Heat Transfer Results from Thermocouples	32
5.1 Data and Results for Medium Coolant Flow Rate	32
5.2 Effects of Rotation on Local Heat Transfer	47
5.3 Summary of Results from Thermocouple Measurements	58
6.0 Heat Transfer Results from Liquid Crystals	59
6.1 Results for Stationary Tests	59
6.2 Results for Rotating Tests	64
7.0 Comparison with Previous Analysis	73
8.0 References	74
9.0 Appendix	79
9.1 Nomenclature	80

		<u>Page</u>
9.2	Tables of Flow Conditions for Full Scale NASA Radial Turbine and 1.15 Scale Model Coolant Passage	81
9.3	Sample Data Table for Stationary Test Condition and Medium Flowrate (Test # 6.2, TC 2)	93
9.4	Adjusted Thermocouple Results	97

## LIST OF TABLES

<u>Table</u>		<u>Page</u>
Table 3-1	Locations of Wall Thermocouples in Model	14
Table 4-1	Flow Conditions for Transient Heat Transfer Tests	29

## LIST OF FIGURES

<u>Figure</u>		<u>Page</u>
Figure 2-1	Sketch of Internal Coolant Passage for NASA LeRC Cooled High Temperature Radial Turbine Program	5
Figure 3-1	Internal Passages of NASA LeRC Cooled Radial Turbine Rotor	8
Figure 3-2	Nomenclature for Internal Passages of NASA LeRC Cooled Turbine Rotor	9
Figure 3-3	Photograph of Leading and Trailing Surfaces of Coolant Passage Before Assembly	10
Figure 3-4	Thermocouple Instrumentation for Internal Passages of NASA LeRC Cooled Turbine Rotor	13
Figure 3-5	Photograph of Model Mounted in Rotating Heat Transfer Facility (with cover removed)	15
Figure 3-6	Schematic of Rotating Heat Transfer Facility	15
Figure 3-7	Optics Arrangement for Rotating Heat Transfer Measurements With Liquid Crystals	20
Figure 3-8	Optical Test Section With Previous Four Pass Model Installed	20
Figure 3-9	Frame of Video Recording Before Start of Transient Heat Transfer Test	21
Figure 3-10	Frame of Video Recording During Transient Heat Transfer Test	22
Figure 3-11	Processed Frame of Video Data From Transient Heat Transfer Test	23
Figure 3-12	Uncertainty Analysis Results	26
Figure 4-1	Comparison of Test Matrix With NASA LeRC Full Scale Operating Conditions	30
Figure 5-1	Thermocouple Data for Liquid Crystal Test on Leading Surface with $\Omega = 0$ RPM	33
Figure 5-2	Results From Thermocouple Data for Liquid Crystal Test on Leading Surface with $\Omega = 0$ RPM	34

<u>Figure</u>		<u>Page</u>
Figure 5-3	Thermocouple Data for Liquid Crystal Test on Trailing Surface with $\Omega = 0$ RPM	35
Figure 5-4	Results From Thermocouple Data for Liquid Crystal Test on Trailing Surface With $\Omega = 0$ RPM	36
Figure 5-5	Thermocouple Data for Liquid Crystal Test on Leading Surface with $\Omega = 450$ RPM	39
Figure 5-6	Results From Thermocouple Data for Liquid Crystal Test on Leading Surface with $\Omega = 450$ RPM	40
Figure 5-7	Thermocouple Data for Liquid Crystal Test on Trailing Surface with $\Omega = 450$ RPM	41
Figure 5-8	Results From Thermocouple Data for Liquid Crystal Test on Trailing Surface With $\Omega = 450$ RPM	42
Figure 5-9	Thermocouple Data for Liquid Crystal Test on Leading Surface with $\Omega = 750$ RPM	43
Figure 5-10	Results From Thermocouple Data for Liquid Crystal Test on Leading Surface with $\Omega = 750$ RPM	44
Figure 5-11	Thermocouple Data for Liquid Crystal Test on Trailing Surface with $\Omega = 750$ RPM	45
Figure 5-12	Results From Thermocouple Data for Liquid Crystal Test on Trailing Surface With $\Omega = 750$ RPM	46
Figure 5-13	Dimensional and Dimensionless Heat Transfer Results From Thermocouple Data for Region 1	48
Figure 5-14	Dimensional Heat Transfer Results From Thermocouple Data for Region 2 and $Re = 13,000$	49
Figure 5-15	Dimensionless Heat Transfer Results From Thermocouple Data for Region 2	50
Figure 5-16	Dimensional Heat Transfer Results From Thermocouple Data for Region 3 and $Re = 13,000$	53
Figure 5-17	Dimensionless Heat Transfer Results From Thermocouple Data for Region 3	54
Figure 5-18	Dimensional Heat Transfer Results From Thermocouple Data for Region 4 and $Re = 13,000$	55
Figure 5-19	Dimensionless Heat Transfer Results From Thermocouple Data for Region 4	56
Figure 6-1	Video Records of Liquid Crystal Isotherms for Test 8.1	60
Figure 6-2	Video Records of Liquid Crystal Isotherms for Test 6.2	61
Figure 6-3	Nomograph for Evaluating Liquid Crystal Data for $Re = 13,000$ and $\Omega = 0$ RPM	62
Figure 6-4	Heat Transfer Coefficients From Liquid Crystal Isotherms for $Re = 13,000$ and $\Omega = 0$ RPM	63
Figure 6-5	Video Records of Liquid Crystal Isotherms for Test 16.3	65
Figure 6-6	Video Records of Liquid Crystal Isotherms for Test 10.2	66

<u>Figure</u>		<u>Page</u>
Figure 6-7	Nomograph for Evaluating Liquid Crystal Data for Re = 13,000 and $\Omega$ = 450 RPM	67
Figure 6-8	Heat Transfer Coefficients From Liquid Crystal Isotherms for Re = 13,000 and $\Omega$ = 450 RPM	68
Figure 6-9	Video Records of Liquid Crystal Isotherms for Test 16.4	69
Figure 6-10	Video Records of Liquid Crystal Isotherms for Test 12.2	70
Figure 6-11	Nomograph for Evaluating Liquid Crystal Data for Re = 13,000 and $\Omega$ = 750 RPM	71
Figure 6-12	Heat Transfer Coefficients From Liquid Crystal Isotherms for Re = 13,000 and $\Omega$ = 750 RPM	72
Figure 9.4-1	Thermocouple Data for Liquid Crystal Test on Leading Surface with $\Omega$ = 0 RPM	98
Figure 9.4-2	Results From Thermocouple Data for Liquid Crystal Test on Leading Surface with $\Omega$ = 0 RPM	99
Figure 9.4-3	Thermocouple Data for Liquid Crystal Test on Trailing Surface with $\Omega$ = 0 RPM	100
Figure 9.4-4	Results From Thermocouple Data for Liquid Crystal Test on Trailing Surface With $\Omega$ = 0 RPM	101
Figure 9.4-5	Thermocouple Data for Liquid Crystal Test on Leading Surface with $\Omega$ = 450 RPM	102
Figure 9.4-6	Results From Thermocouple Data for Liquid Crystal Test on Leading Surface with $\Omega$ = 450 RPM	103
Figure 9.4-7	Thermocouple Data for Liquid Crystal Test on Trailing Surface with $\Omega$ = 450 RPM	104
Figure 9.4-8	Results From Thermocouple Data for Liquid Crystal Test on Trailing Surface With $\Omega$ = 450 RPM	105
Figure 9.4-9	Thermocouple Data for Liquid Crystal Test on Leading Surface with $\Omega$ = 750 RPM	106
Figure 9.4-10	Results From Thermocouple Data for Liquid Crystal Test on Leading Surface with $\Omega$ = 750 RPM	107
Figure 9.4-11	Thermocouple Data for Liquid Crystal Test on Trailing Surface with $\Omega$ = 750 RPM	108
Figure 9.4-12	Results From Thermocouple Data for Liquid Crystal Test on Trailing Surface With $\Omega$ = 750 RPM	109





## **1.0 SUMMARY**

An experimental study was conducted (1) to experimentally measure, assess and analyze the heat transfer within the internal cooling configuration of a radial turbine rotor blade and (2) to obtain heat transfer data to evaluate and improve CFD procedures and turbulent transport models of internal coolant flows. A 1.15 times scale model of the coolant passages within the NASA LeRC High Temperature Radial Turbine was designed, fabricated of Lucite and instrumented for transient heat transfer tests using thin film surface thermocouples and liquid crystals to indicate temperatures. Transient heat transfer tests were conducted for Reynolds numbers of one-fourth, one-half, and equal to the operating Reynolds number for the NASA Turbine. Tests were conducted for stationary and rotating conditions with rotation numbers in the range occurring in the NASA Turbine.

Results from the experiments showed the heat transfer characteristics within the coolant passage were affected by rotation. In general, the heat transfer increased and decreased on the sides of the straight radial passages with rotation as previously reported from NASA-HOST-sponsored experiments. The heat transfer in the tri-passage axial flow region adjacent to the blade exit was relatively unaffected by rotation. However, the heat transfer on one surface, in the transitional region between the radial inflow passage and axial, constant radius passages, decreased to approximately 20 percent of the values without rotation. Comparisons with previous 3-D numerical studies indicated regions where the heat transfer characteristics agreed and disagreed with the present experiment.

## 2.0 INTRODUCTION

NASA Lewis Research Center (LeRC), the US Army and US gas turbine manufacturers have been developing light weight, radial gas turbines for over 20 years. NASA LeRC and the US Army Aviation Systems Command, in conjunction with gas turbine contractors, have a Cooled High-Temperature Radial Turbine Program with a cooled turbine designed and manufactured by the Allison Gas Turbine Division (Snyder, 1992), an analytical and experimental program at the LeRC, and analytical efforts at ADAPCO and Carnegie Mellon University. The present study supports the NASA LeRC program by experimentally determining the heat transfer characteristics in the coolant passages of a model similar to the LeRC rotor (Snyder, 1992).

### 2.1 Background

Axial Flow Turbines - Heat transfer in rotating radial internal coolant passages, typical of turbine airfoils of large gas turbine aircraft engines, has been investigated experimentally and analytically for the past ten to fifteen years. The experimental studies have been sponsored by national and private laboratories (e.g. USA/NASA, USSR, UK/RAE, France, Germany/DLR, Japan, Taiwan, USA/DOE, and USA/EPRI) and the large gas turbine manufacturers (e.g. PW, GE, and RR). The pioneering studies were reported by Morris, 1981. More recent studies up to 1991, with a wider range of flow and geometric parameters, are reported in the authors' previous papers by Wagner et al., 1991, and Johnson et al., 1992, and in NASA contractors reports, Hajek et al., 1991, and Johnson et al., 1993. Other recent references include Han et al., 1992, El-Husayni et al., 1992, and Mochizuki et al., 1992, and contain most references from the studies sponsored by GE, EPRI, and RAE. The results from these studies are bringing an understanding to the turbine blade durability designer of the effects of many parameters on heat transfer in rotating radial coolant passages including such flow parameters as Reynolds number, rotation number, wall-to-bulk density ratio, and buoyancy in addition to such geometric parameters as trip geometry, passage aspect ratio, and flow direction. The understanding developed by the authors in their previous studies of heat transfer in rotating internal coolant passages will be used to interpret the results of the present study.

Radial Flow Turbines - Internal cooling of radial turbines is more complex than that for axial turbines because of the large surface area of the coolant passages, the large variations in coolant passage cross-sectional area from inlet to exit, and the changes in flow direction, axially and azimuthally, as the blade contour varies. A summary of work to 1992 (Roelke, 1992) describes the previous cooled radial turbine efforts at Garrett (Vershure et al., 1980), Pratt and Whitney (Calvert et al., 1971), and Solar

(Hammer et al., 1986). The previous heat transfer studies have been primarily analytic or have measured the overall performance of the turbine.

The analytical heat transfers studies to date have been conducted with one and three dimensional analyses. The one dimensional analyses have used heat transfer relationships and a flow network analysis for multi-path flows. The three dimensional analyses have used 3-D Navier Stokes codes and have been focused on the configuration used in the NASA LeRC Cooled High Temperature Radial Turbine Program. The 3-D studies include those by Ippolito, 1991, at ADAPCO using the STAR-CD code, Dawes, 1992, using a code with an unstructured grid, Steinthorsson et al., 1993, and Stephens et al., 1993. Results from the analytical studies vary, however, all studies show regions with low convective velocities which can be expected to produce low heat transfer rates and low heat transfer coefficients.

## 2.2 Objectives

The principal objectives of this project are (1) to experimentally measure, assess, and analyze the heat transfer within the internal cooling passage of a radial turbine rotor blade and (2) to obtain heat transfer data to evaluate and improve CFD procedures and turbulent transport models in internal coolant flows.

The model used for the experiments was a 1.15 times scale of the coolant passages in the NASA LeRC Cooled Radial Turbine (Figure 2-1). The model was constructed from a Lucite block and was instrumented for transient heat transfer experiments with surface and air temperature thermocouples and liquid crystal paints. Based on (1) UTC previous experience (e.g. Hajek et al., 1991, and Johnson et al., 1993) in the NASA HOST and in corporate sponsored research programs on heat transfer in rotating models for axial flow turbines and (2) the flowrates and operating conditions of the LeRC turbine, it is expected that the rotation number ( $Ro = \omega d/V$ ) and the coolant passage Reynolds numbers ( $Re = \rho V d/\mu$ ) will be the principal parameters affecting heat transfer in the model. In addition, because of the reasonably high Reynolds numbers, it is expected that the heat transfer will scale approximately as  $Re^{0.8}$ . The test matrix was developed using these assumptions.

The transient heat transfer data, which was obtained in this program and which will be used to evaluate CFD codes, is difficult to present in report form because of its three-dimensional, time dependent nature. In addition, the data was obtained on a model at flow conditions that were not identical to those used to predict the performance of the NASA rotor. Therefore, an approximate heat transfer coefficient was deduced from the results based on the time dependent heat flux from the wall, the time dependent inlet temperature, and the local wall temperature. This coefficient will be used to

evaluate the effects of rotation and to make qualitative comparisons with the available numerical predictions.

The transient heat transfer results obtained from the surface thermocouple data will be discussed first. These data obtained at approximately one second intervals for the 150 second tests, are smoothed and used to produce more accurate results than the liquid crystal data. The liquid crystal data will be subsequently discussed and used, in conjunction with the surface thermocouple data, to determine isotherms (at specific times) and iso-heat transfer coefficient contours. These results will be qualitatively compared with 3-D Navier Stokes calculations.

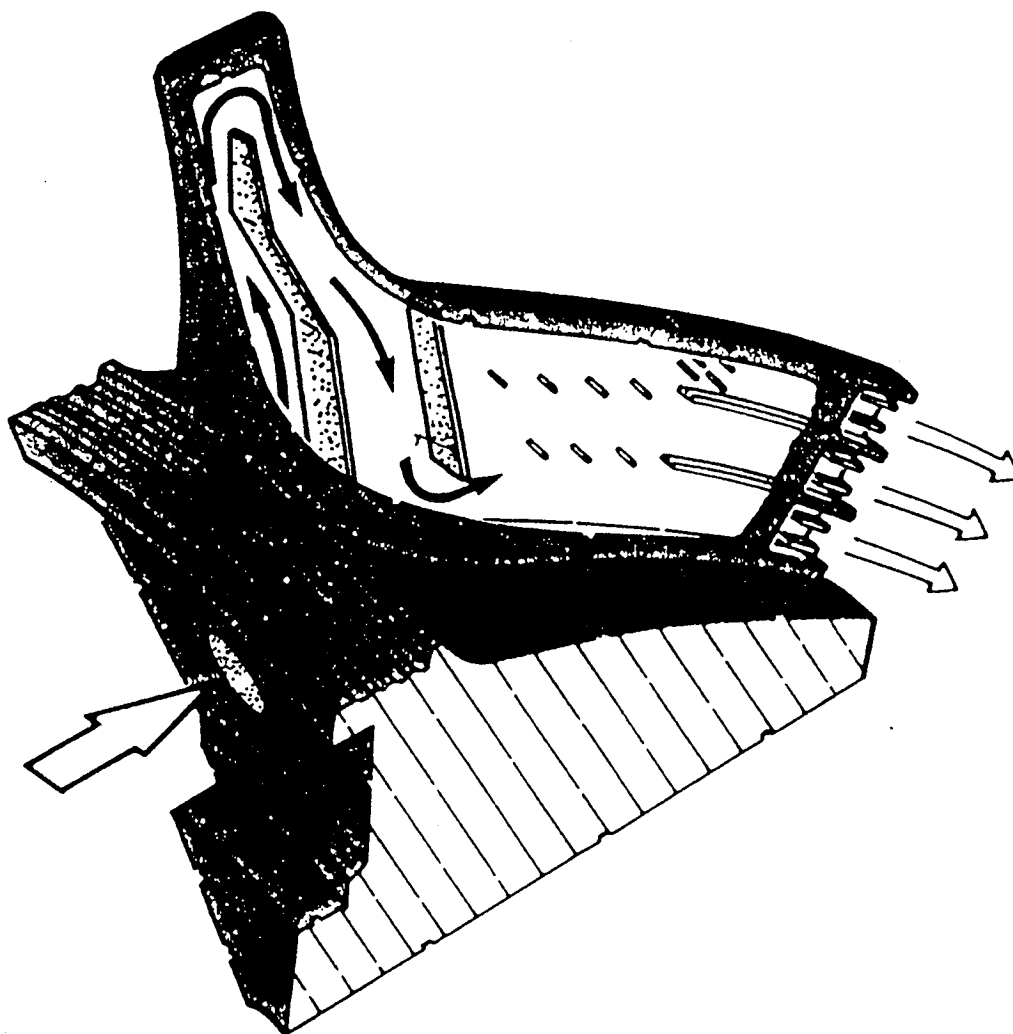


Figure 2-1. Sketch of Internal Coolant Passage for NASA LeRC Cooled High Temperature Radial Turbine Program.

### 3.0 DESCRIPTION OF APPARATUS AND EXPERIMENT

#### 3.1 Heat Transfer Model

A Lucite model of the coolant passages in the NASA LeRC High-Temperature, Cooled, Radial Turbine was constructed for the experiments. The model was 1.15 times the actual scale and was constructed using surface coordinates obtained from the LeRC (Roelke, 1991) and drawings from the Allison Division, General Motors (Anon, 1989).

The views of the coolant passage with the coordinate grid, the flow dividers, and pedestals are shown in Figure 3-1. The coolant inlet passage of the full-scale rotor was simulated in the 1.15 scale Lucite model. The coolant exit geometry was modified to account for the relatively small radial pressure gradient at the model exit plenum due to the larger radial location of the model compared to the full scale model. The exit plane of the coolant passage was selected to be the streamwise location where the coolant passage is faired into the trailing edge on the pressure side of the blade (Figure 3-2). Based on flow estimate information from the LeRC, a discharge flow-control plate with selected orifices was used at the model exit plane to approximate the exit flow distribution. Twelve orifices were used to regulate the distribution of trailing edge flow. Six were located at the exit of the inner trailing edge passage and three were located at each exit of the middle and outer trailing edge passages. The orifices were evenly spaced in the radial direction in patterns of three. The inner passage required the pattern to be staggered to obtain a more uniform discharge area distribution. The discharge areas of the inner exit passage was twice that of the middle and outer exit passages (see Figure 3-2 and table below). Consequently, the configuration is expected to have 50 percent of the total coolant flow in the inner exit passage and 25 percent of the total coolant flow in each of the middle and outer exit passages.

	Exit Plane Orifices	
	No. Used	Diameter, mm(in.)
Inner passage	6	1.5 (0.059)
Middle passage	3	1.5 (0.059)
Outer passage	3	1.5 (0.059)

The leading and trailing surfaces of the coolant passages were machined in blocks of Lucite as shown in Figure 3-3. The coolant passage was oriented 32.7 degrees from the plane of the test section. This required that the test section with the model be rotated that amount to conduct the experiment with the same relative orientation (i.e. axial alignment) as the full scale rotor.

The design and fabrication of the model were accomplished using Computer Aided Design and Computer Aided Machining Technology. The assembly drawing for the model and installation is UTRC Drawing 1896-30.

### **3.2 Model Instrumentation**

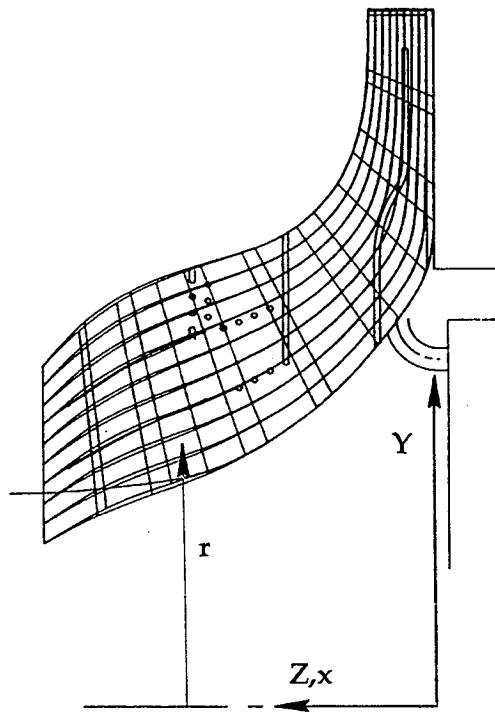
The coolant passage model was instrumented with thermocouples and liquid crystal temperature indicating paints as discussed in the following paragraphs.

**Thermocouple Instrumentation** - Chromel-Alumel, thin-film surface thermocouples were installed on the leading and trailing test surfaces at selected locations as shown in Figure 3-4. The thin-film thermocouples used were 13 microns (0.0005 in.) thick which resulted in minimal disturbance to the coolant flow. These surface thermocouples provide an on-board calibration for the liquid crystals and are also used to obtain local heat transfer rates with numerous time-temperature data points. The locations of the wall thermocouples are presented in Table 3.1. Fine-wire (36 gage) thermocouples with small beads were used to measure the inlet air temperature and the exit air temperatures. Four thermocouples were installed in the inlet duct by suspending the thermocouple from the sides of the duct. A thermocouple was also suspended in the air stream downstream of a central orifice used to control the relative flowrate through each of the three Region 4 channels. Inspection of all the air thermocouples after the experiments indicated that all the thermocouple junctions were in the same position as at the onset of the experiments.

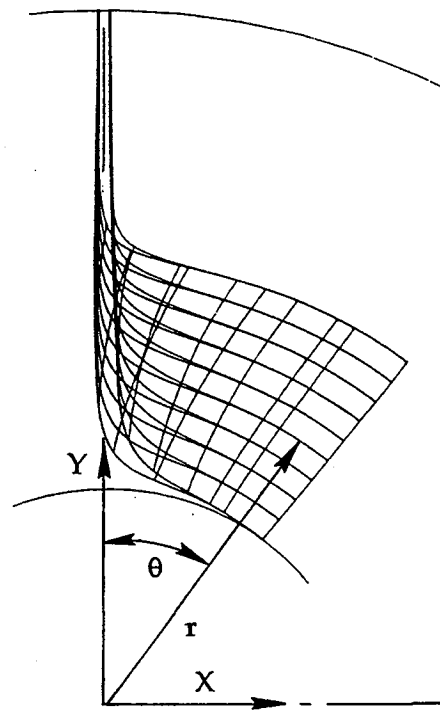
**Liquid Crystal** - Mixtures of encapsulated, chiral-nematic paints for color changes at 47C(116F), 43C(110F), 38C(100F), 32C(90F), and 27C(80F) were sprayed on the test surfaces after the surface thermocouples were installed. A layer approximately 13 microns (0.0005 in.) thick was used for these tests. A second layer, approximately 13 microns thick, of black, water-based paint was sprayed over the liquid crystal to provide optical separation between the leading and trailing surfaces. These thicknesses provide adequate liquid crystal signals (i.e. color change) and do not require a large correction in the data analysis due to the temperature drop across the liquid crystal and black paints.



a) Y-Z View



b) Y-X View



c) Perspective View

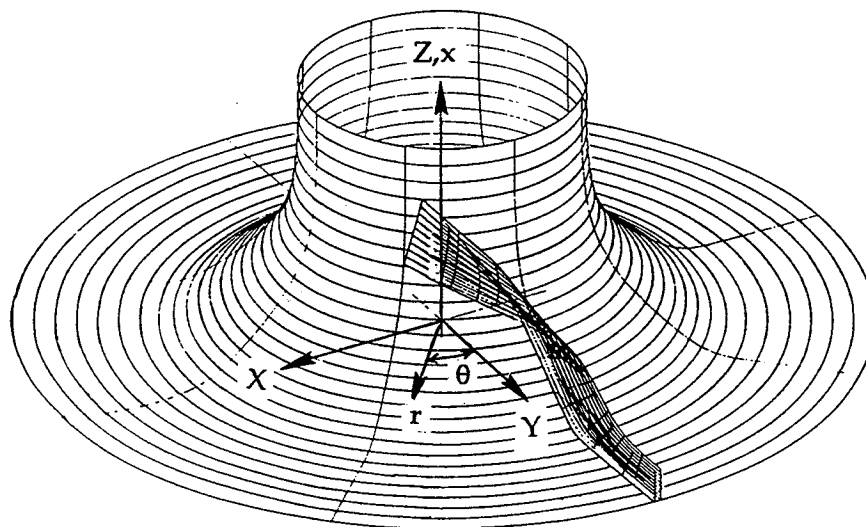


Figure 3-1. Internal Passages of NASA LeRC Cooled Radial Turbine Rotor.

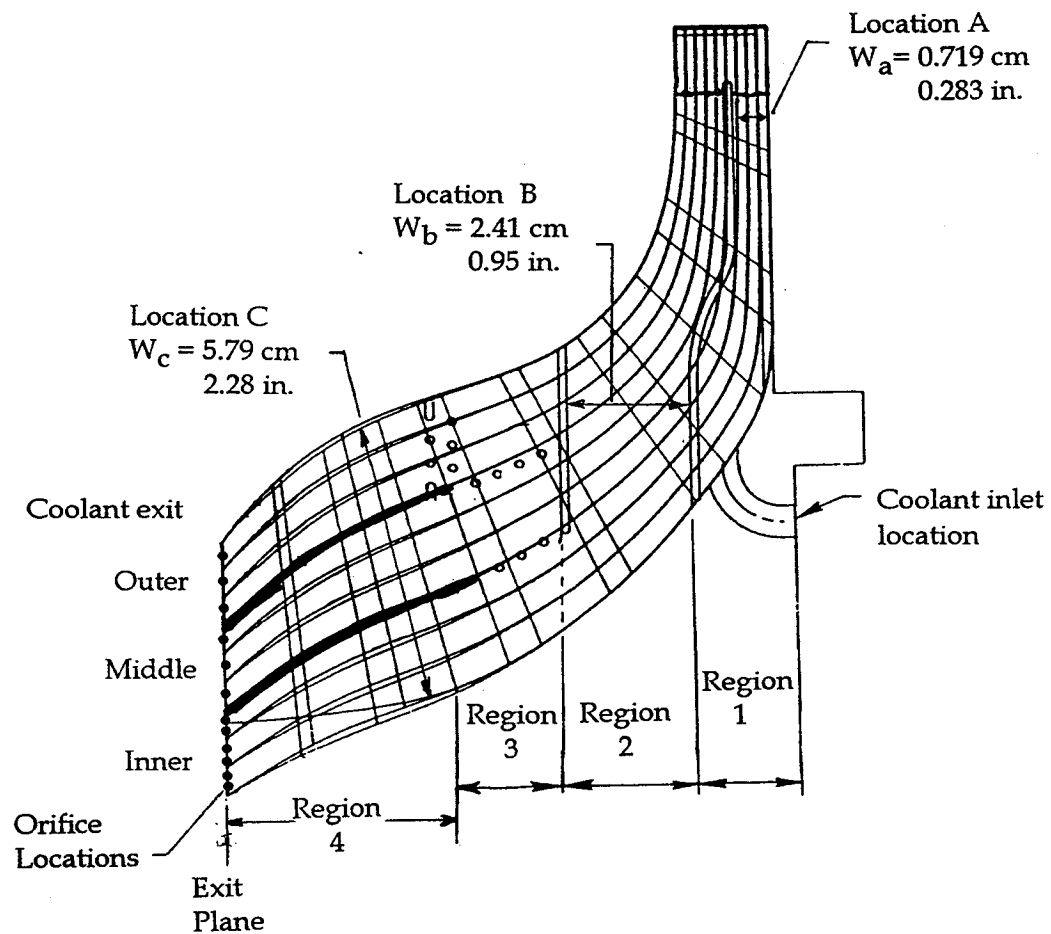


Figure 3-2. Nomenclature for Internal Passages of NASA LeRC Cooled Turbine Rotor.

UTRC Drawing 1896-30-66913  
Trailing Surface

UTRC Drawing 1896-30-66912  
Leading Surface

10

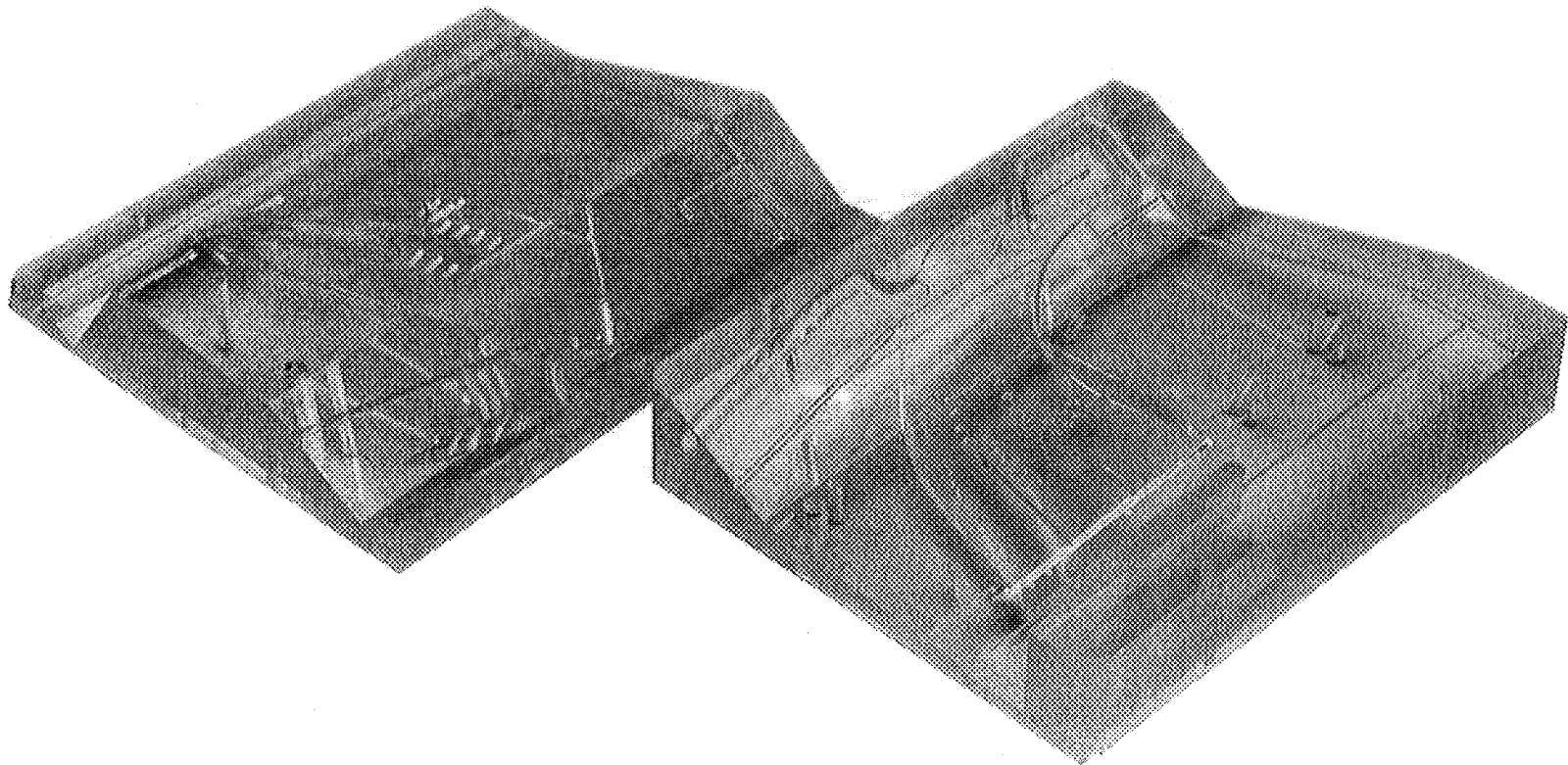


Figure 3-3. Photograph of Leading and Trailing Surfaces of Coolant Passage Before Assembly.

### 3.3. Rotating Heat Transfer Facility

**Rotating Components** - The Rotating Heat Transfer Facility (RHTF) (Figures 3-5 and 3-6) consists of the containment vessel with the integral arm assembly and motor with associated controller. The containment vessel is 1.83 m (6.0 ft) in diameter and was designed to withstand a destructive failure of the rotating assembly. The vessel was designed for operation at a pressure of 5 to 13 mm of Hg absolute to reduce the power required to rotate the arm. The rotating arm assembly is driven by a 11 KW (15 Hp) DC motor via a toothed belt. Shaft RPM is controlled by an adjustable feedback electronic controller. Maximum shaft speed is approximately 3,500 RPM producing body forces on the model of approximately 14,000 g's at the tip of the model and approximately 10,000 g's at the root. However, the flash lamps used to illuminate the model were found to not work properly when the pressure was below atmospheric. Therefore, the vessel was operated at near atmospheric pressure and the maximum shaft speed for the present program was 750 RPM. A safety shutdown interlock circuit is used to turn off the drive motor and model heater power supplies, turn on a magnetic brake and open the containment vessel vacuum chamber vent. The safety shutdown system prevents damage to the model or the facility in the event of a leak in the model or an imbalance in the rotating assembly.

The shaft assembly comprises a main outer shaft with two shorter inner shafts. This shaft arrangement was designed for dual fluid paths from each rotary union mounted on the ends of the shaft to the rotating assembly. For the present program, a single fluid path was utilized to provide coolant air to and from the heat transfer model. Grooves located on the exterior surface of the outer shaft allow instrumentation and power leads to extend from the rotating arm to the rotating portion of the instrumentation slipring. Two slipring assemblies (a 40 channel unit located on the upper end of the shaft and a 200 channel unit located on the lower end of the shaft) are used to transfer heater power and instrumentation leads between the stationary and rotating frames of reference.

**Thermocouple Data Acquisition System** - The data acquisition system contains two major components; the computer and the data acquisition control unit. The computer consisted of a DEC PDP 11/03 processor unit with 128k memory, two 20 cm (8 in) floppy disk drives, and a DECWRITER III terminal. The Hewlett Packard 3497A data acquisition system can be controlled from the front panel or through the interface connected to the computer. Upon completion of the acquisition of voltage data through the acquisition control unit and the computer, results are calculated and printed in engineering units. Flow parameter and raw data are stored on disk for future reduction.

**Heater Power Sources** - A variable DC power supply was used to provide current to the model inlet heater assembly. The air inlet, electrical-resistance-type, heater assembly consisted of a thin-wall

tube bundle connected in series. Model inlet coolant air flowed through the tubes which were aligned in the flow direction. The model air was heated to the initial temperature for each experiment by passing current through the tubes. The thin-wall tubes were subsequently heated by the tube resistance and provided an efficient method of heating the inlet air. The thin-wall tubes also provided a relatively short time constant response due to low total mass of the system. The current from the power supply was switched on and off by a computer controlled, high current capacity relay. Additional low power supplies were used to heat resistance film heaters mounted to the model pressure containment shell. These auxiliary heaters were used to help provide isothermal initial test conditions.

**Flow Supply System** - Model coolant air is supplied continuously by the UTRC 27 atm (400 psig) air system which is regulated to approximately 10 atm (150 psig) at the RHTF. The air flowrate to the model is measured with variable area flow meters. The model coolant return air flows through an additional flow meter to determine a mass flow balance on the system. Model pressure is controlled by back pressuring the model air flow system with a return air control valve. The maximum mass flowrate available is dependent on the model operating pressure and the total pressure loss of the system including the heat transfer model. For typical models, the maximum air flowrate is approximately 0.02 kg/sec (0.044 lbm/sec).

The model air is cooled to approximately  $-12^{\circ}\text{C}$  ( $10^{\circ}\text{F}$ ) before flowing to the shaft rotary union with a chilled-liquid/air heat exchanger. Heat pickup in the shaft and air supply lines on the rotating arm increase the model air temperature to approximately  $10^{\circ}\text{C}$  ( $50^{\circ}\text{F}$ ) at the location just before entering the model inlet heater system.

- + Air TC
- Wall TC
- Exit orifice locations

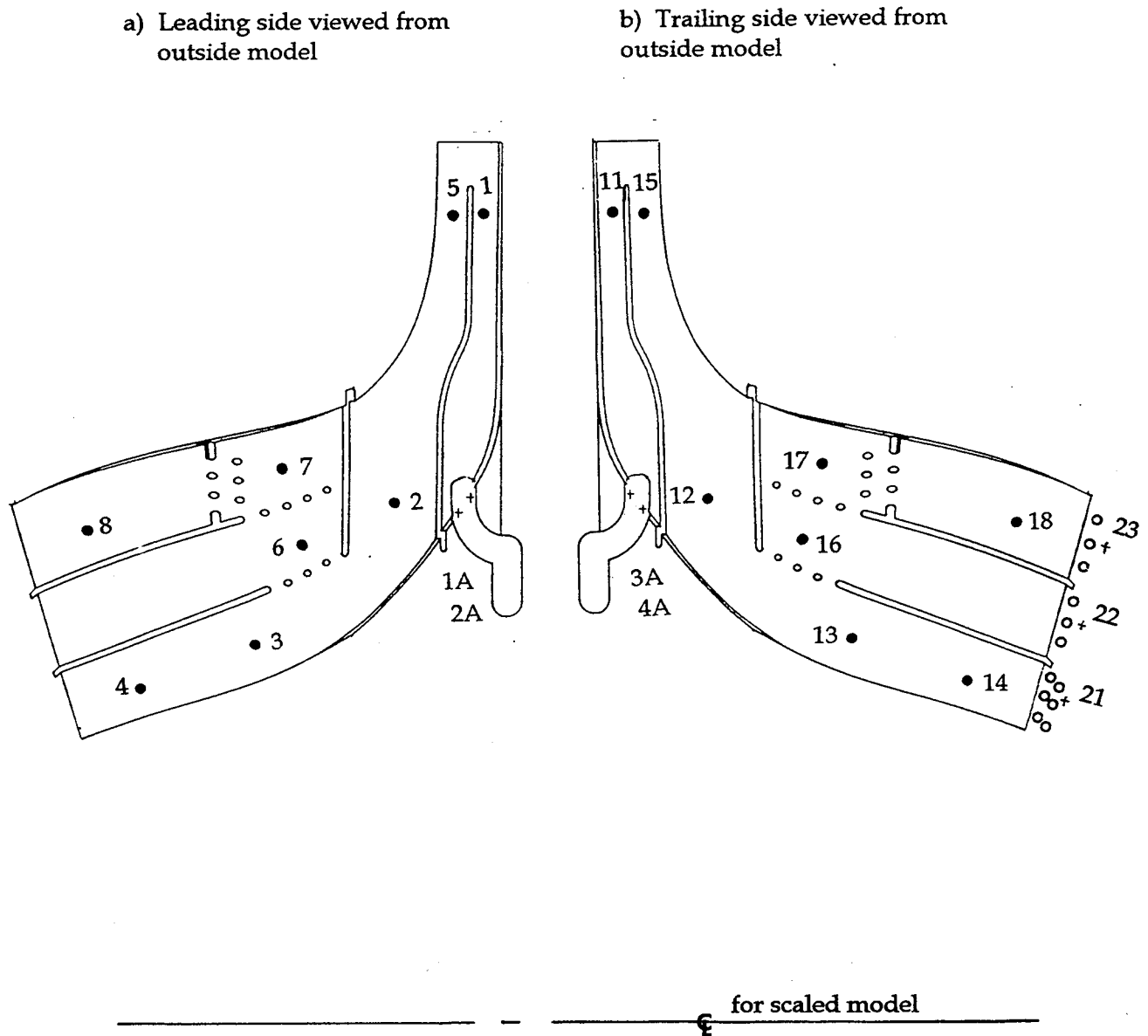


Figure 3-4. Thermocouple Instrumentation for Internal Passages of NASA LeRC Cooled Turbine Rotor. (Note: model centerline was moved 22.85 inches from the center of rotation of the test facility.)

**TABLE 3-1 LOCATIONS OF WALL THERMOCOUPLES IN MODEL**

NASA LeRC Radial Turbine Rotor

Thermocouple Locations reference to UTRC Drawings Nos. 1896-30-66913 & 66912

Note: Axial reference point is the upstream tip of the coolant passage

(See Figures 3-1 and 3-4 for coordinate systems)

Location	TC#	1.15 Scale Model In facility coordinates			1.15 Scale Model In rotor coordinates			Full Scale NASA LeRC Model		
		x (in.)	R (in.)	θ (deg.)	x (in.)	r (in.)	θ (deg.)	X (in.)	Y (in.)	Z (in.)
Leading	1	0.125 *	30.145 *	-0.530 *	0.125 *	7.300 *	-0.530			
Leading	5	0.520	30.160	-0.530	0.520	7.315	-0.530	-0.068	6.361	0.452
Leading	2	1.169	27.328	-1.010	1.169	3.383	-1.010	-0.079	3.899	1.017
Leading	7	2.293	27.845	4.370	2.293	5.012	4.370	0.381	4.358	1.994
Leading	3	2.375	26.369	4.120	2.375	3.532	4.120	0.254	3.071	2.065
Leading	8	3.380	28.323	19.360	3.380	4.699	19.360	1.558	4.086	2.939
Leading	4	3.242	25.830	16.120	3.242	3.092	16.120	0.858	2.689	2.819
Trailing	11	0.125 *	30.045 *	.57*	0.125 *	7.200 *	0.570			
Trailing	15	0.492	30.077	0.570	0.492	7.232	0.570	0.072	6.289	0.428
Trailing	12	1.144	27.190	1.550	1.144	4.346	1.550	0.118	3.779	0.995
Trailing	17	2.340	27.901	6.390	2.340	5.082	6.390	0.566	4.419	2.045
Trailing	13	2.419	26.016	8.550	2.419	3.202	8.550	0.476	2.784	2.103
Trailing	18	3.380	27.127	20.710	3.380	4.527	20.710	1.601	3.937	2.939
Trailing	14	3.278	25.704	19.830	3.278	3.018	19.830	1.024	2.624	2.850

\* = Approximate location

x = axial distance relative to

r = radial distance relative to the scaled rotor centerline before mounting in the rotating facility

R = radial distance relative to model centerline of rotation after mounted in the rotating facility

θ = angular location relative to the

X,Y,Z = cartesian coordinates for the fullscale NASA LeRC Model

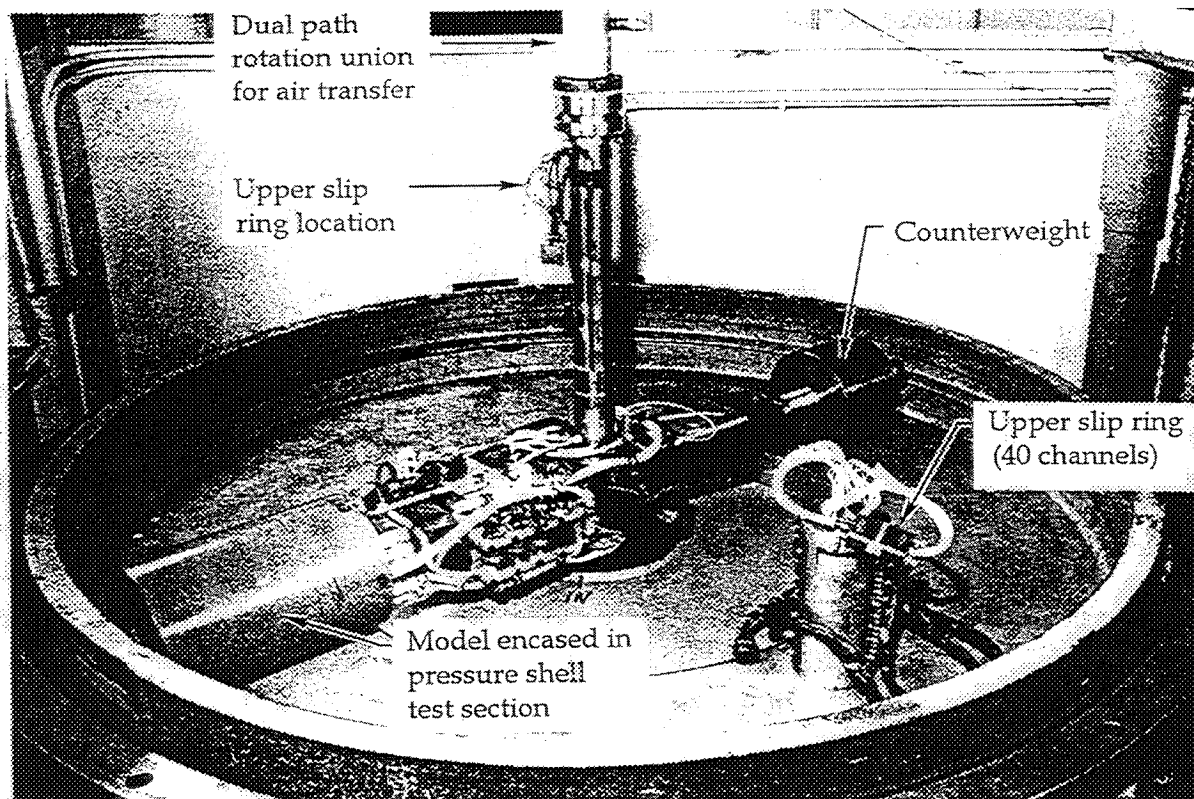


Figure 3-5. Photograph of a Model Mounted in Rotating Heat Transfer Facility. (Rotating heat transfer facility with cover removed).

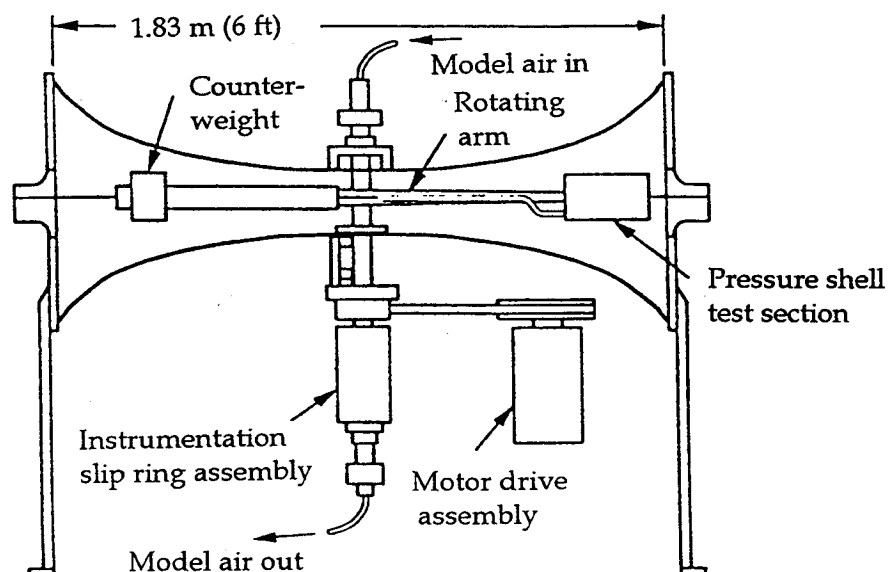


Figure 3-6. Schematic of Rotating Heat Transfer Facility.



### 3.4 Experimental Procedures

**Thermocouple Data Acquisition** - The EMF for each thermocouple was measured and recorded using laboratory computers and the HP3497A data acquisition system. The data acquisition system was configured to repeatedly measure the EMF from a sequence of thermocouples in the model. The data was stored in a memory buffer in the HP3497 and transferred to a data file for the specific test number.

Some unsteadiness was noted for some thermocouples. Typical time variations of measured temperature are presented in Section 5. The time variations of temperature indicate an approximately  $\pm 0.5^{\circ}\text{C}$  ( $1^{\circ}\text{F}$ ) random noise component added to the expected temperature variation. The probable sources for this unsteadiness were (1) rotating instrumentation leads through magnetic flux lines generated by the DC motor, (2) motor power controller noise, and (3) lead, slipping, and instrumentation contact irregularities. The temperature data were smoothed by performing a second order, least squares fit to the closest seven data points around each time point of interest. This technique effectively removed the random noise component but allowed the fit temperature to follow the experimental transient.

**Thermocouple Data Reduction** - Transient heat transfer measurement techniques are well documented (e.g., Schultz, et al., 1973, Clifford, et al., 1983, Metzger and Larson, 1986, Saabas et al., 1987, and Metzger et al., 1989). A typical approach to obtaining transient heat transfer data involves solving the one-dimensional transient heat conduction equation subject to a semi-infinite wall boundary condition with a uniform initial wall temperature and a step change in a convection boundary condition on the surface exposed to the coolant flow (e.g., Kreith, 1973, Metzger and Larson, 1986, Metzger et al., 1989). A single, time-temperature pair (typically from phase change paints, wall mounted thermocouples or liquid-crystal paints) is then used to determine the heat transfer coefficient for each separate point on the test surface. Different points on a test surface will have differing time-temperature histories. Implicit in this solution is that the heat transfer coefficient is a constant with time. However, when heat transfer coefficient is known to be a function of the temperature difference, such as in rotating coolant passages, this technique may not be appropriate (see Wagner et al., 1989, for more discussion of the combined effects of Coriolis and buoyancy forces on heat transfer in rotating passages).

The one-dimensional, time dependent heat conduction equation was solved to obtain a time dependent heat flux and a time dependent heat transfer coefficient. The formulation for time dependent heat transfer coefficients is required because of the variations in the heat transfer coefficient during the transient test due to changing buoyancy effects as the wall-to-bulk temperature difference decreases. 2-D effects of lateral conduction have been studied and reported by Metzger et al., 1989; Metzger and Larson, 1986, and Saabas et al., 1987, and will not be discussed here. In general, the 1-D assumption has

been shown to be valid for a judicious choice of test surface material and test times. Following is a description of the UTRC data analysis procedure from Blair et al., 1991, solved to obtain a relationship for the heat flux from the prescribed surface temperature boundary condition at a particular point in the coolant passage. The 1-D transient heat conduction equation subject to a semi-infinite wall boundary condition and a time dependent prescribed surface temperature is shown below.

$$\frac{\delta^2 T(x, t)}{\delta x^2} = \frac{1}{\alpha} \frac{\delta T(x, t)}{\delta t}$$

with boundary and initial conditions:

$$T(x, 0) = m^* x + T_i$$

$$\frac{\delta T(\infty, t)}{\delta x} = m$$

$$T(0, t) = \text{experimentally determined}$$

Solution:

$$Q(t) = \frac{k}{\sqrt{\alpha\pi}} \int_0^t \frac{T'_w(0, t-\tau)}{\sqrt{\tau}} \delta\tau - m^* k$$

An analysis showed that the first temporal derivative of the wall temperature is a continuous function, therefore, the evaluation of the integral was accomplished by assuming an average derivative,  $T'(0, t-\tau)$ , for a given time increment. This reduced the integral to a series of summations for equally spaced time increments which were evaluated as shown below.

$$Q(t) = \sum_{i=2}^j \left[ \sqrt{t(i)} - \sqrt{t(i-1)} \right] * \left[ T'_w(j+2-i) - T'_w(j+1-i) \right]$$

A term was included in the solution to allow for an initial temperature gradient in the model wall due to the difficulty of obtaining a perfect isothermal initial condition during the warm-up phase of the experiment. For the case of an isothermal wall initial condition, this term is zero.

These tests had heaters in the space between the model and the Lucite windows which formed the transparent walls of the Optical Test Section (Figures 3-7 and 3-8). The heaters were used to bring the average temperature on the outer wall of the model to the same temperature as the inlet air temperature at the start of the test. In general, isothermal conditions (i.e. inlet flow and model surface temperature within  $\pm 1^\circ\text{C}(2^\circ\text{F})$ ) were obtained for the stationary test conditions. However, test conditions with rotation had larger temperature variations (i.e. on the order of  $\pm 3^\circ\text{C}(6^\circ\text{F})$ ) especially on the trailing surface and at the model coolant air exit plane. The procedure to obtain isothermal conditions consisted of flowing heated air through the model coolant passages with the external auxiliary heaters on for approximately two hours prior to the initiation of the transient portion of the test. It is likely that the combination of rotating the model and the thicker model walls on the trailing side resulted in a need for an increase in the thermal soak time which was not recognized at the time of the test. With limited external surface instrumentation (3 external thermocouples on each side) and a fairly complex 3-D thermal initial condition an acceptable initial temperature gradient could not be determined. Therefore, no initial temperature gradient term was used for the analysis of the data in this study. A discussion of the effect of initial wall temperature gradient is included in subsequent paragraphs where experimental uncertainties of the data are presented.

**Video Data Acquisition** - The typical pre-test procedure consisted of heating the air flowing through the rotating model coolant passages until the acrylic heat transfer model walls reached approximately isothermal conditions. Note, the experimental methods described by Metzger and Larson, 1986, and Saabas et al., 1987, utilized an initially cold model wall subject to a suddenly heated mainstream flow. However, for the rotating heat transfer problem, the model walls must be hot with a cold coolant flow in order to give the proper sense to the rotation-induced buoyancy force effects (see Clifford, 1985, and Wagner et al., 1989). The test was then initiated by switching off the power to the coolant passage inlet heater. A video imaging system was utilized to record the changing liquid crystal paint on the coolant passage surface. Concurrently, the inlet and exit coolant temperatures and surface temperatures were recorded as described in the thermocouple data acquisition section.

The video data was acquired using the optics arrangement shown in Figure 3-7. The video was recorded on 3/4 inch magnetic tape. The time reference was superimposed on each frame using a time/date generator. The start of each transient test (Time = 0.0 sec) occurred when the heater power was shut off. Typical test times recorded were 5 seconds prior to the start of the test and 150 to 200

seconds after the start. The camera and lighting system were timed by a 1/REV signal such that the model was recorded in approximately the same position each revolution. (i.e. +/- 1 degree of rotation).

**Video Data Analysis** - Video imaging processing equipment was used to analyze selected video frames. The image processing equipment can display, edit, enhance, analyze, print, and animate images. The video analysis system supports many standard image processing functions, including histogram equalization, contrast enhancement, density profiling, smoothing, sharpening, edge detection, median filtering, and spatial convolution with user defined kernels up to 63x63.

Typical test and data analysis frames are shown in Figures 3-9, 3-10 and 3-11. The video recording obtained before the start of the test is shown in Figure 3-9. Only the portions of the video showing a surface of the model are shown. This frame provides a reference that includes shadows and reflections from the two layers of Lucite. A frame of the video during the test is shown in Figure 3-10. Although there are differences between Figures 3-9 and 3-10, the liquid crystal contours cannot be readily discerned from the viewing of one video frame. However, the contours are easier to discern when viewing the video during playback and the viewer's eye and mind can discern the small changes in video frames.

A processed video data frame is shown in Figure 3-11. The processing included subtracting the Figure 3-9 frame from the Figure 3-10 frame, adjusting the location of the pixels to account for small shifts in the model location, and contrast enhancement. This video frame process enhancement eliminates extraneous light reflections by "zeroing" portions of the image not associated with the model coolant passage and enhances the intensity of the liquid crystal isotherms. The processed frame shows a small liquid crystal contour in Region 1, (see Figure 3-2 for definitions of Regions) two contours in Region 2 with flow radially inward, and contours in Regions 3 and 4 at the entrances to the Inner and Middle portions of Region 4. Each contour on the frame was identified as to temperature and the time after the start of the test. See Figure 6-2 for the identifications of video frames used on this video test for the trailing surface.

Corrections were made to the coolant path wall surface temperature to account for the transient energy storage in the liquid-crystal paint and temperature gradients through the paint. The transient energy storage corrections were obtained by estimating the temperature at the paint/air interface based on the calculated heat flux and the measured temperature at the paint/acrylic interface. The average internal paint temperature was then calculated for each time step. Differences in the temporal response of the average paint temperature and the paint/acrylic interface temperature (measured with the liquid-crystal

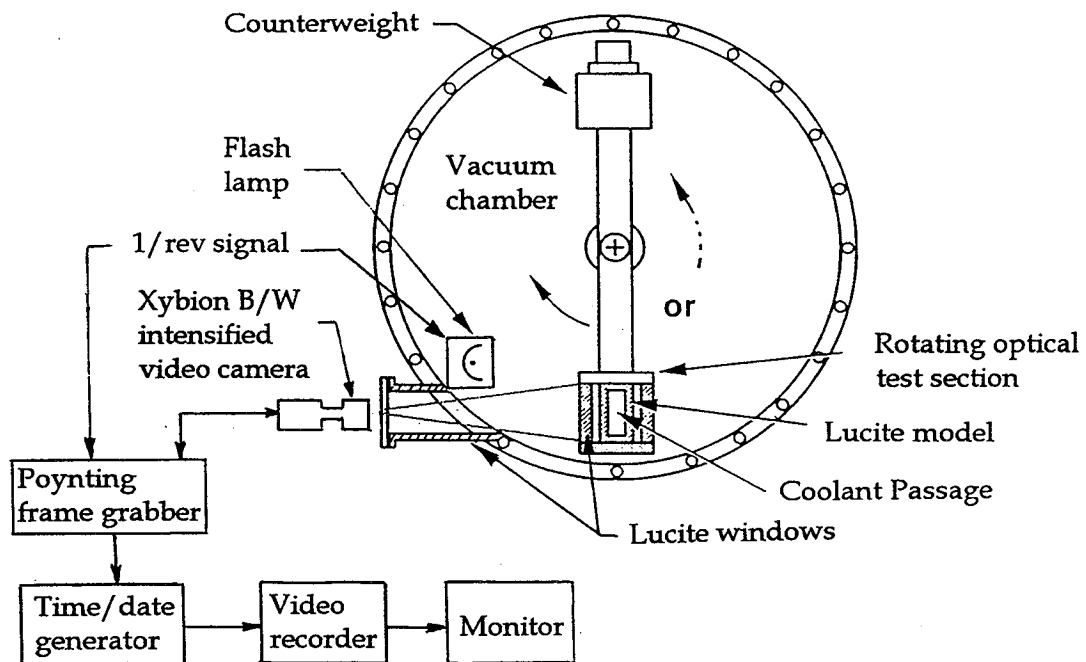


Figure 3-7. Optics Arrangement for Rotating Heat Transfer Measurements With Liquid Crystals.

UTRC Drawing 1896-20

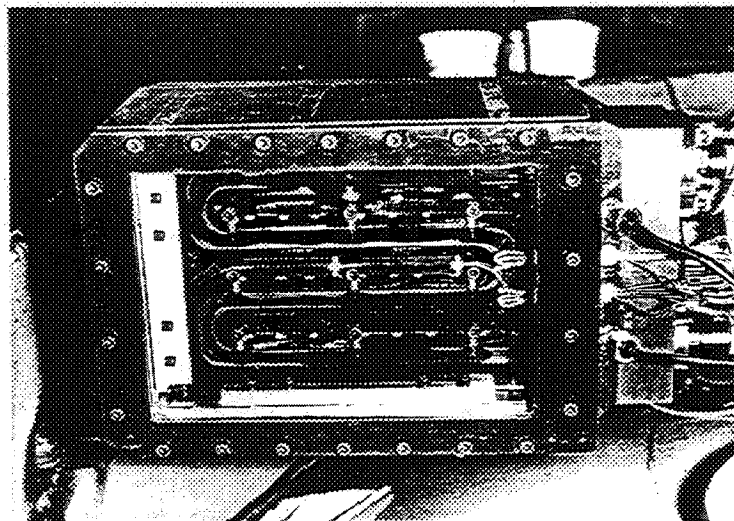


Figure 3-8. Rotating Optical Test Section With Previous Four Pass Model Installed.

Superimposed on NASA LeRC cooled turbine rotor outline

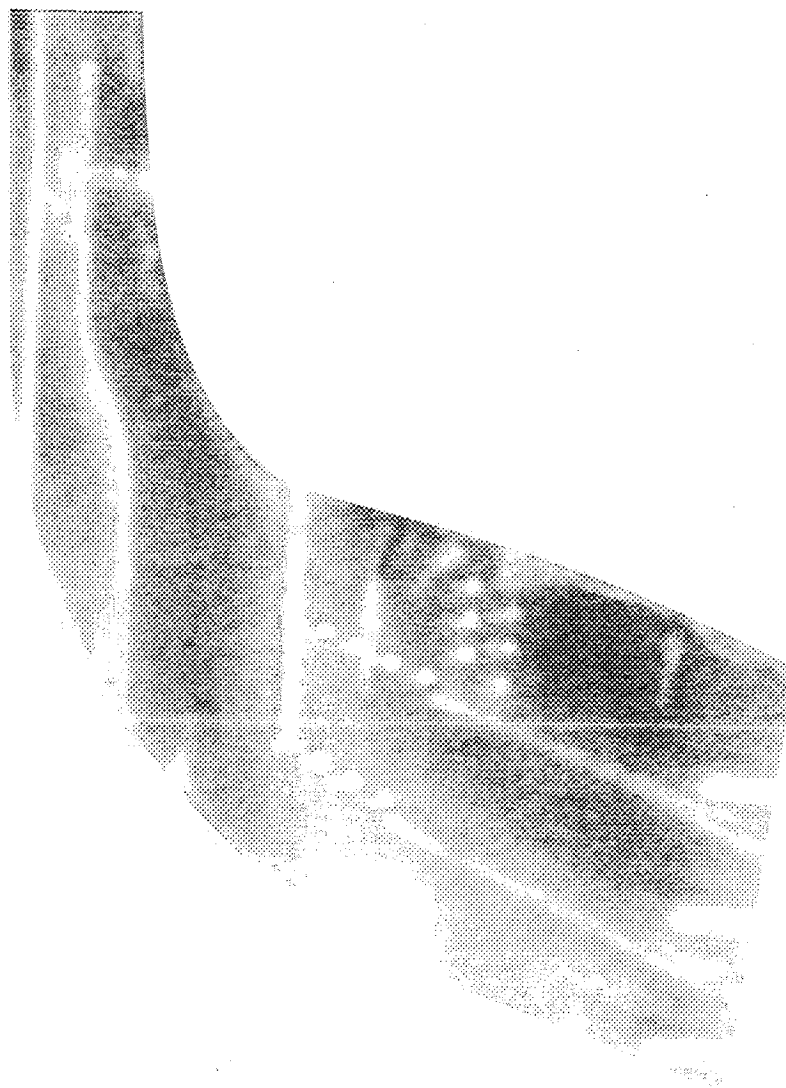


Figure 3-9. Frame of Video Recording Before Start of Transient Heat Transfer Test.

Superimposed on NASA LeRC cooled turbine rotor outline

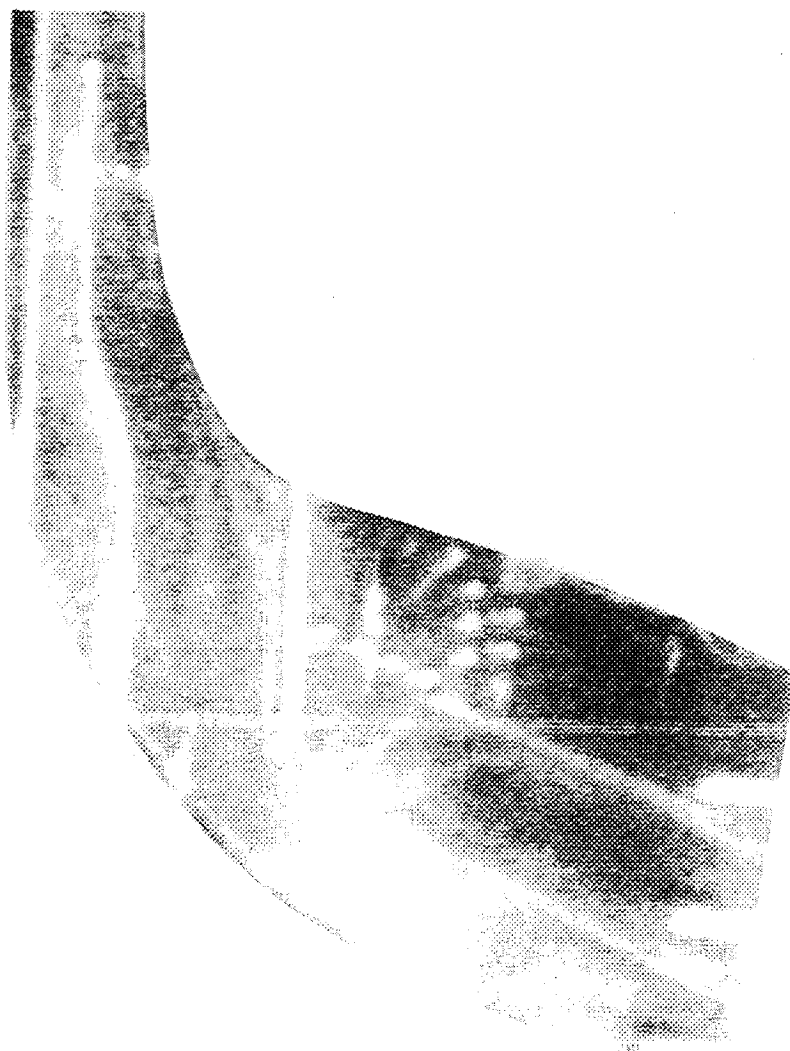


Figure 3-10. Frame of Video Recording During Transient Heat Transfer Test.

Superimposed on NASA LeRC cooled turbine rotor outline

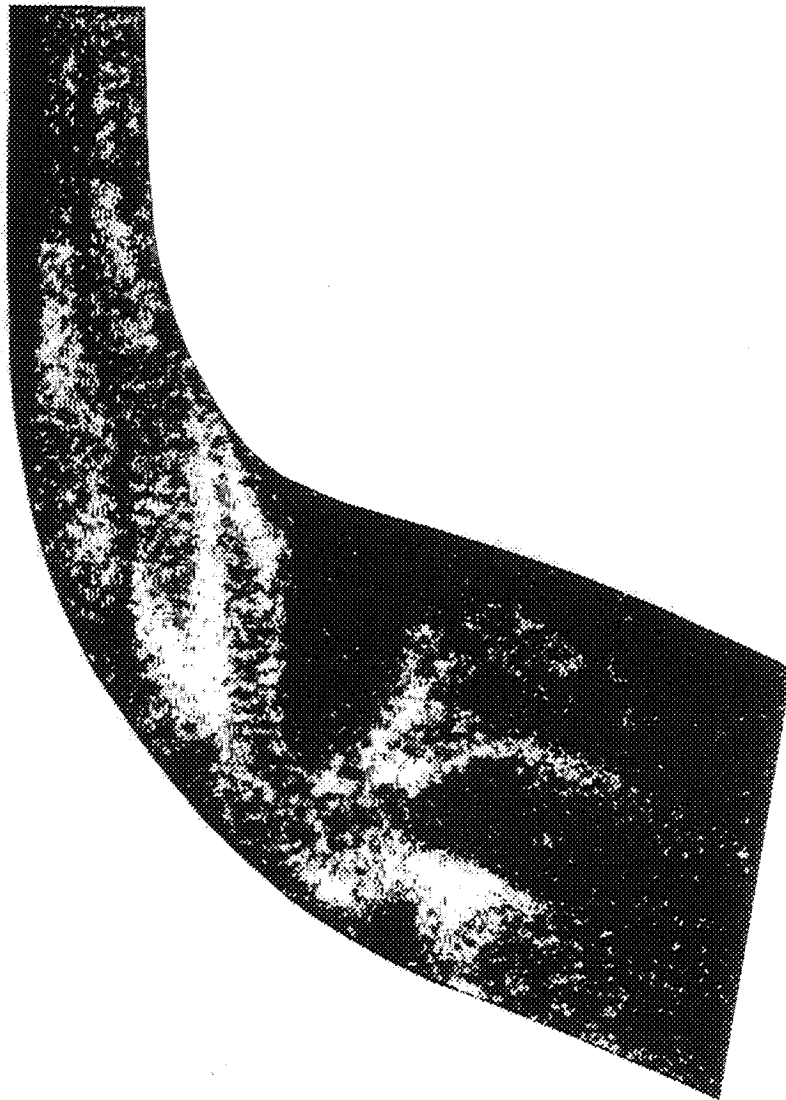


Figure 3-11. Processed Frame of Video Data From Transient Heat Transfer Test.



paint) were associated with the transient energy storage in the paint. The corrections associated with the energy storage and temperature gradient in the paint were typically on the order of 3 to 5 percent after 10 seconds.

A rotation induced calibration shift was also observed in this series of experiments. Comparison of the surface temperatures obtained with the liquid crystal paints with the thin film thermocouples showed that a calibration correction was necessary when the model was rotating. The temperatures measured with the liquid crystals on the stationary model were in good agreement, i.e.  $\pm 0.5^{\circ}\text{C}$  ( $1^{\circ}\text{F}$ ), with the thermocouple measurement for stationary test conditions. The temperature calibration of the liquid crystals changed considerably during rotation. The liquid crystals are known to be sensitive to shear stresses which will occur due to the centrifugal force on the liquid crystals due to its own weight and that of the black overcoat on the liquid crystal paint. The experimental results showed a  $2$  to  $7^{\circ}\text{C}$  ( $4$  to  $14^{\circ}\text{F}$ ) difference between the liquid-crystal surface and thin film thermocouples mounted on the test surface at the 450 and 750 RPM test conditions. This calibration shift is attributed to stresses in the paint under conditions of rotation which are not present when stationary. The surface thermocouples provide an on board calibration required to resolve these variations.

Heat transfer coefficients at specific locations were calculated by dividing the instantaneous heat flux with the wall-to-coolant inlet temperature difference for a given test time.

**Accuracy of Results** - A number of factors can affect the accuracy of the reduced heat transfer coefficient data. Typically, uncertainties in absolute and relative temperature differences are the largest contributors to uncertainties in calculated heat transfer coefficients. In this section the effect of temperature measurement error, noise in the temperature data, time resolution error, initial wall temperature gradient, paint thickness, and material property errors are presented.

A baseline test condition (Run 6.2) at a midpassage location (TC02) was used for the uncertainty analysis. The baseline wall temperature data was perturbed as noted and reduced to evaluate the effects listed. The temperature measurement error was simulated by adding  $1^{\circ}\text{C}$  ( $2^{\circ}\text{F}$ ) to the raw data. Noise in the data was simulated by applying a random function ranging  $\pm 1^{\circ}\text{C}$  ( $2^{\circ}\text{F}$ ) to the smoothed data. The effect of time resolution was simulated by adding 1 second to the raw data. The effect of an initial wall temperature gradient was determined by assuming the outside of the model was approximately  $6^{\circ}\text{C}$  ( $10^{\circ}\text{F}$ ) lower than the coolant passage surface at the start of the test. The effect of uncertainty of the Lucite model material properties was determined by adjusting the thermal conductivity 10 percent. The perturbations were applied to the measured data set and reduced to obtain heat flux and heat transfer coefficient results.

The inlet coolant temperature, wall temperature, heat flux, and heat transfer coefficient records are shown in Figure 3-12. The results show that random noise on the wall temperature data causes significant fluctuations in the resulting heat flux and heat transfer coefficient histories (Figure 3-12c and d) and that fluctuations in the heat transfer results are more likely related to less-than-ideal smoothing rather than flow-induced oscillations. Aside from the application of random offsets to the wall temperature data, the perturbation analysis indicates that the results are fairly insensitive to the effects studied. The percent change in heat transfer coefficient at Time = 50 seconds is listed below. As previously noted, the uncertainty in measuring temperature results in the largest contribution to the uncertainty in the heat transfer coefficient results although the temperature offset had a minimal effect on the heat flux distribution.

#### Percent Change in Heat Transfer Coefficient

	<u>Percent Change</u>
$T_{\text{wall}} + 1^{\circ}\text{C}(2^{\circ}\text{F})$	-8
$T_{\text{wall}} \pm \text{(random)} 1^{\circ}\text{C}(2^{\circ}\text{F})$	NA
Time + 1 second	+1
With initial gradient	-3
Without paint corrections	-3
10 percent increase in model conductivity	+5

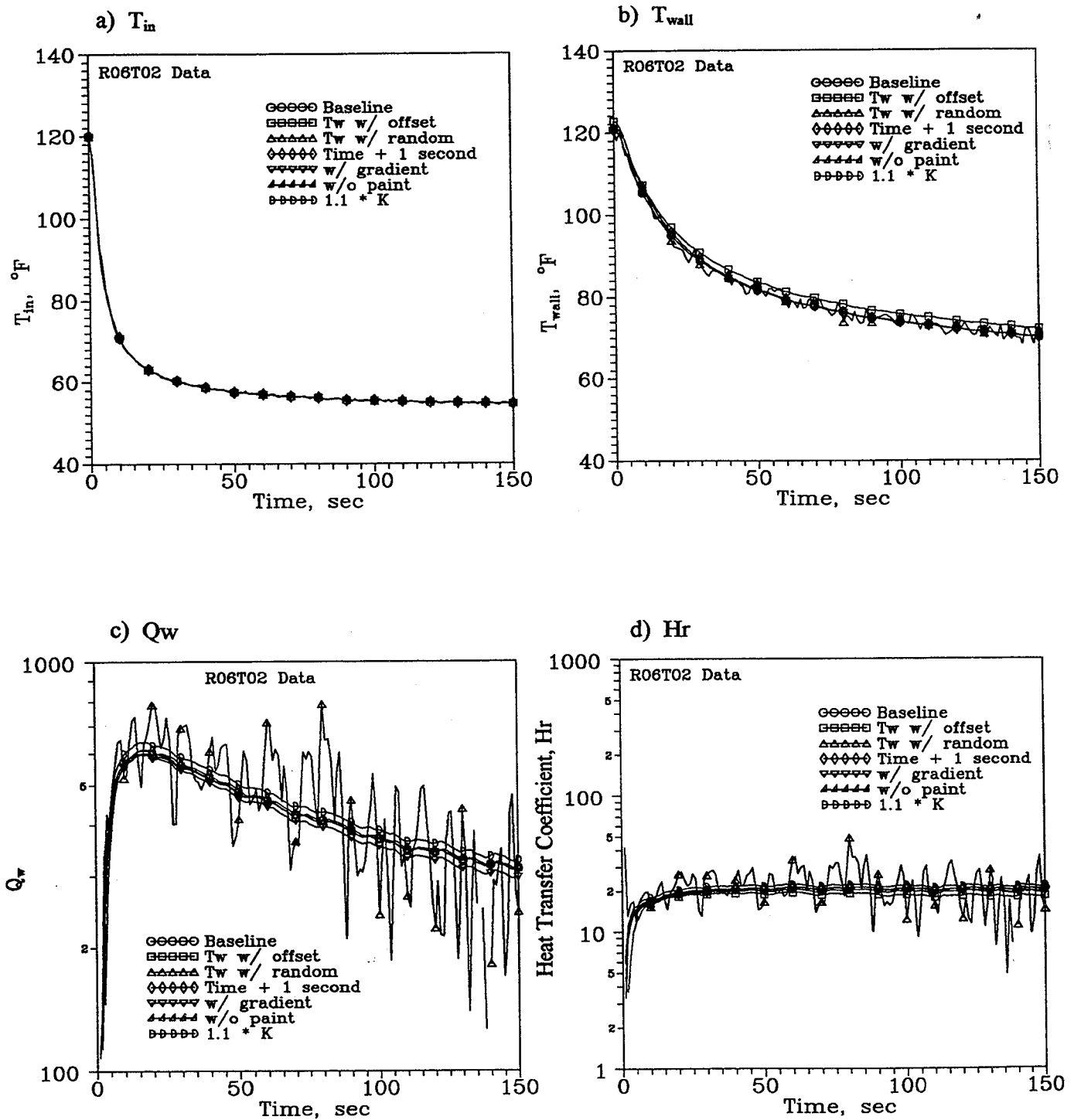


Figure 3-12. Uncertainty Analysis Results (Run 6.2, TC02)

## 4.0 EXPERIMENTAL PARAMETERS AND TEST MATRIX

The present study of heat transfer from a 1.15 times scale model was conducted at several dimensionless flow parameters in or near the range of the NASA LeRC rotor. Following is discussion of the flow and geometric parameter test conditions, and an outline of the presentation of results.

### 4.1 Flow Parameters

A dimensional analysis study performed at UTRC (Section 10 of Hajek et al., 1991, similar to that of Guidez, 1989), showed that the flow patterns and convective heat transfer in rotating radial passages would be influenced by four dimensionless flow parameters and several geometric parameters. The dimensionless flow parameters are as follows:

Reynolds number	(Re)	$\rho V d / \mu$
Rotation Number	(Ro)	$\omega d / V$ or $\omega H / V$
Density Ratio	$(\Delta \rho / \rho)$	$(\rho_b - \rho_w) / \rho_b = (T_w - T_b) / T_w$
Buoyancy Parameter (BUOY)		$[(\rho_b - \rho_w) / \rho_b](\omega R / V)(\omega d / V)$

For flow in rotating radial coolant passages, Coriolis forces, represented by the dimensionless parameter,  $\omega d / V$ , and the dimensionless streamwise velocity gradients, produce secondary flows in the plane perpendicular to the radial direction. These secondary flows are produced by the viscous force/Coriolis force interaction. Buoyancy also produces secondary flows in the radial direction. For flow in rotating radial coolant passages with walls hotter than the bulk fluid, the buoyancy effects drive the heated flow inward. Thus, the buoyancy flow direction is opposite the mean velocity direction for flow radially outward and is in the same direction for flow radially inward. From previous studies, both the Coriolis and buoyancy forces can be expected to produce significant changes to the coolant passage flowfield and heat transfer. Rotating constant-temperature flow studies by Johnston, et al., 1972, have shown that the Coriolis forces can dampen turbulent fluctuations and laminarize flow in portions of a channel. Combined free and forced convection studies in stationary systems have shown that the turbulent shear structure and heat transfer is significantly altered with co-flowing or counter-flowing buoyancy effects ( e.g., Eckert et al., 1953).

## 4.2 Geometric Parameters

The flow and heat transfer in stationary coolant passages are also strong functions of the geometric parameters (e.g., Johnson et al., 1993). All parameters except the radial location of the model are identical to the NASA LeRC rotor.

## 4.3 Test Conditions

The test conditions for the heat transfer experiments are listed in Table 4-1. The variations of Reynolds number and rotation numbers are shown in Figure 4-1. Tests were conducted for three flowrates (Reynolds numbers indicated in the figure) and three nominal rotation rates (0, 450, and 750 RPM). Tests were conducted at the Reynolds number range and approximately one-half and one-fourth the Reynolds number of the Full Scale Rotor. Due to the Reynolds number variation in the coolant passage for a given flowrate, subsequent references to flowrate will be as low, medium, and high flowrate test conditions. A tabulation of the test conditions for which thermocouple and liquid crystal data were obtained and the Full Scale NASA LeRC Radial (Full Scale) Turbine operating conditions are presented in Section 9.2. The characteristic dimensions used for the representation of the Reynolds and rotation numbers are shown in Figure 3-2. The channel width dimensions,  $W$ , were determined from the model drawings. The channel depth dimensions,  $H$ , at each location indicated on Figure 3-2 were obtained from the tabulated coolant passage coordinates supplied by the LeRC. Because of the flow distribution uncertainty, the average results anticipated for Regions 3 and 4 are represented by the single Location C.

Results are presented for all of the available locations. The Nusselt and Reynolds numbers (nominal values noted in the figures where appropriate) were calculated based on the geometry of Location B (see Appendix 9.2 and Figure 3-2). The viscosity and thermal conductivity of the coolant were based on the film properties where the coolant temperature was assumed to be the lowest temperature obtained for a given test condition ( $T_c$ , Appendix 9.2) and the wall temperature was assumed to be the initial temperature of the coolant (i.e. the ideal initial wall temperature,  $T_w$  in Appendix 9.2). Flow properties, velocity and Reynolds number, were based on the coolant temperature described above. Whereas the Nusselt and Reynolds numbers used the hydraulic diameter of the passage for a characteristic dimension, the separation distance,  $H$ , was used for the calculation of Rotation number. Local Rotation, Reynolds, and Nusselt numbers at a given location can be obtained using the local geometry and applying adjustments to the parameters presented based on ratios of the local and Location B dimensions. Normalizing the data in this manner (i.e. using a common representative model location) resulted in plots with similar scales so that results could be compared more easily. Note that the location designations in the figures refer to thermocouple (TC) locations shown in Figure 3-4.

**Table 4-1**  
**Flow Conditions for Transient Heat Transfer Tests**

Test No.	Date	Flow Rate	RPM	Video Surface	Comments	Data TC	Reduced Video
5.1	4/13/92	H	0	Trailing	(11)	Y	N
5.2	4/13/92	H	0	Trailing	(11)	Y	Y
6.1	4/13/92	M	0	Trailing	(11)	Y	N
6.2	4/13/92	M	0	Trailing		Y	Y
7.1	4/14/93	H	0	Leading	(11)	Y	Y
8.1	4/14/93	M	0	Leading	(11)	Y	Y
9.1	6/1/93	H	453	Trailing	Low Quality Video	Y	N
9.2	6/1/93	M	453	Trailing	Low Quality Video	Y	N
10.1	6/2/93	H	450	Trailing		Y	Y
10.2	6/2/93	M	450	Trailing		Y	Y
11.1	6/3/93	H	756	Trailing		N	N
12.1	6/24/93	H	749	Trailing		Y	Y
12.2	6/24/93	M	751	Trailing		Y	Y
12.3	6/24/93	L	749	Trailing		Y	Y
14.1	6/26/93	H	750	Trailing	No Video	Y	N
14.2	6/26/93	H	750	Trailing	Low Quality Video	Y	N
14.3	6/26/93	M	750	Trailing	Low Quality Video	Y	N
14.4	6/26/93	L	750	Trailing	Low Quality Video	N	N
15.1	8/12/93	H	753	Leading	(1,8,11)	Y	N
16.1	8/13/93	H	450	Leading	(1,11)	Y	Y
16.2	8/13/93	H	753	Leading	(1,8)	Y	Y
16.3	8/13/93	M	750	Leading	(1,8)	Y	Y
16.4	8/13/93	M	450	Leading	(1)	Y	Y
16.5	8/13/93	L	452	Leading	(1,11)	Y	Y
16.6	8/13/93	L	751	Leading	(1)	Y	Y

Note: Numbers in ( ) indicate thermocouple locations where data is not available.

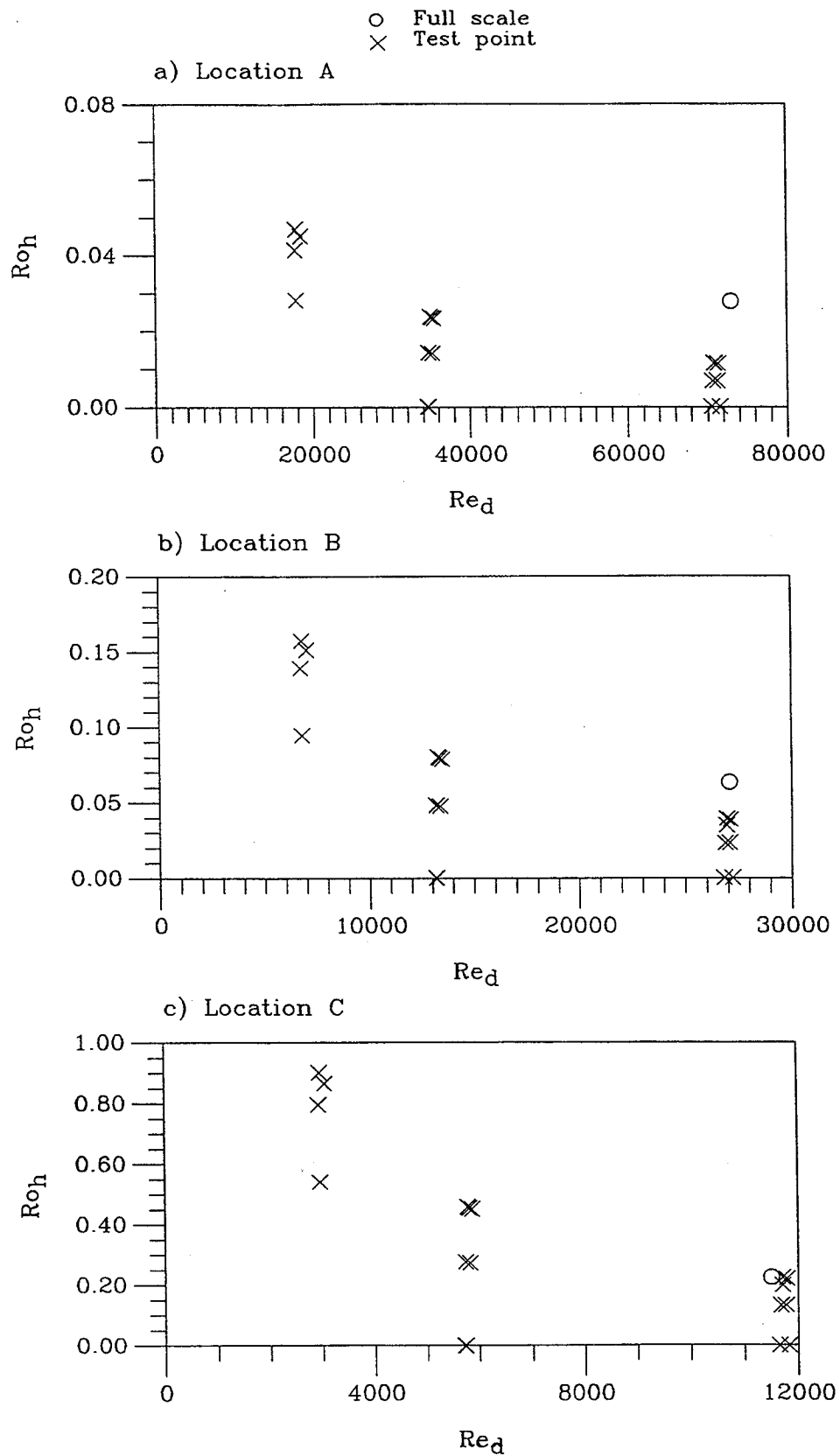


Figure 4-1. Comparison of Test Matrix With NASA LeRC Full Scale Operating Conditions.

The combinations of Re and Ro for the tests and for the Full Scale turbine are shown in Figure 4-1 for Locations A, B, and C. The figure shows the maximum rotation numbers obtained during this series of tests with the scaled UTRC model for Locations A and B (see Figure 3-2) near the entrance of the airfoil coolant passage were approximately half that of the Full Scale model at the design Reynolds number. The low test rotation numbers for these locations were due to facility limitations. However, the design rotation numbers for these locations were obtained at Reynolds numbers half the Full Scale operating conditions.

Design rotation numbers were obtained for Location C as a result of the large pressure drop through the Full Scale model coolant passage (1.66 to 0.82 atmospheres) and the relatively small pressure drop through the UTRC model (11.0 to 10.9 atmospheres). The large pressure drop in the Full Scale model results in a significant increase in coolant velocity and a commensurate decrease in Full Scale rotation numbers compared to little pressure drop in the UTRC model. Therefore, due to the relatively low pressure drop in the coolant passage of the scaled UTRC model the same relative decrease in the rotation number which occurs in the Full Scale model with streamwise distance does not occur in the UTRC model.

#### **4.4 Outline for Presentation of Results**

A total of twenty-five tests were conducted with models as shown in Table 4-1 (repeat runs were obtained under different test numbers). These tests consisted of eight different combinations of coolant flowrate and rotation rate as noted. Repeat runs and runs where one portion of the data system was unsatisfactory are also noted. In order to make the presentation of the principle results for this program tractable and discernible to the reader, the heat transfer data is presented in several stages.

The local heat transfer results obtained from the thermocouple data are presented in Section 5.0. These results show the range of heat flux and heat transfer coefficients based on the inlet air temperature, the local wall temperature, and the local wall heat flux for three sets of rotating conditions and the medium flowrate. The results for each thermocouple location at this flowrate are compared to show the effects of rotation. To summarize the effects of flow and rotation, the heat transfer ratio,  $Nu/Re^{0.8}$ , versus rotation number, Ro, is used to compare all of the data acquired.

Liquid crystal data and regions of constant heat flux will be presented in Section 6.0.



## 5.0 HEAT TRANSFER RESULTS FROM THERMOCOUPLES

Six sets of thermocouple data are presented in detail to identify the range of wall temperature responses, heat fluxes, and heat transfer coefficients based on measured inlet coolant temperatures. All six cases were at the same approximate coolant flowrate, 3.4 gm/sec (0.0075 lbm/sec) and the same model pressure, approximately eleven atmospheres. These data were obtained during transient heat transfer tests at 0, 450, and 750 RPM with concurrent video recording of the leading or trailing coolant passage surfaces (one side per test). These thermocouple data facilitate the interpretation of the results from the video records of the liquid crystal color changes. Data and results are available on computer disk. A sample table is provided in Appendix 9.3.

### 5.1 Data and Results for Medium Coolant Flowrate

Measured temperature, heat flux, and heat transfer coefficient results are presented. The temperature records shown in the figures are not smoothed. Note that not all of the temperature records were available for analysis. During the testing it was speculated that the thin film thermocouples were intermittently failing. However, the test-to-test variations in the quality and availability of the thermocouple data suggest that lead and switch contact irregularities may have been contributing factors. The temperature data was smoothed with a "running" second order fit of the nearest seven data points. The smoothed data was used to obtain heat flux and heat transfer coefficient results. Using more points resulted in smoother heat flux and heat transfer coefficient plots but was not deemed necessary. The major purpose of the smoothing was to reduce the large variations which tended to obscure the general trends (see discussion of uncertainty in Section 3). It is the authors' recommendation that using the relative smoothness of the heat flux and heat transfer coefficient data to contemplate the unsteadiness of the coolant flow should be done with much care.

**Stationary Tests** - The data and results for the two medium flow, stationary tests are presented in Figures 5-1 through 5-4. The leading and trailing wall temperature histories (Figure 5-1c and d) are used to determine their respective wall heat flux histories (e.g., Figure 5-2a and b) as described in Section 3.4. The inlet air temperature histories (e.g., Figure 5-1a), the wall temperature histories, and the heat flux histories are used to determine a heat transfer coefficient,  $h_r$ , (e.g., Figure 5-2c and d) based on the difference between the local wall temperature and the inlet temperature. Note that the calculated heat transfer coefficients are essentially independent of time after 10 seconds of test time for these stationary tests.

Re = 13,000

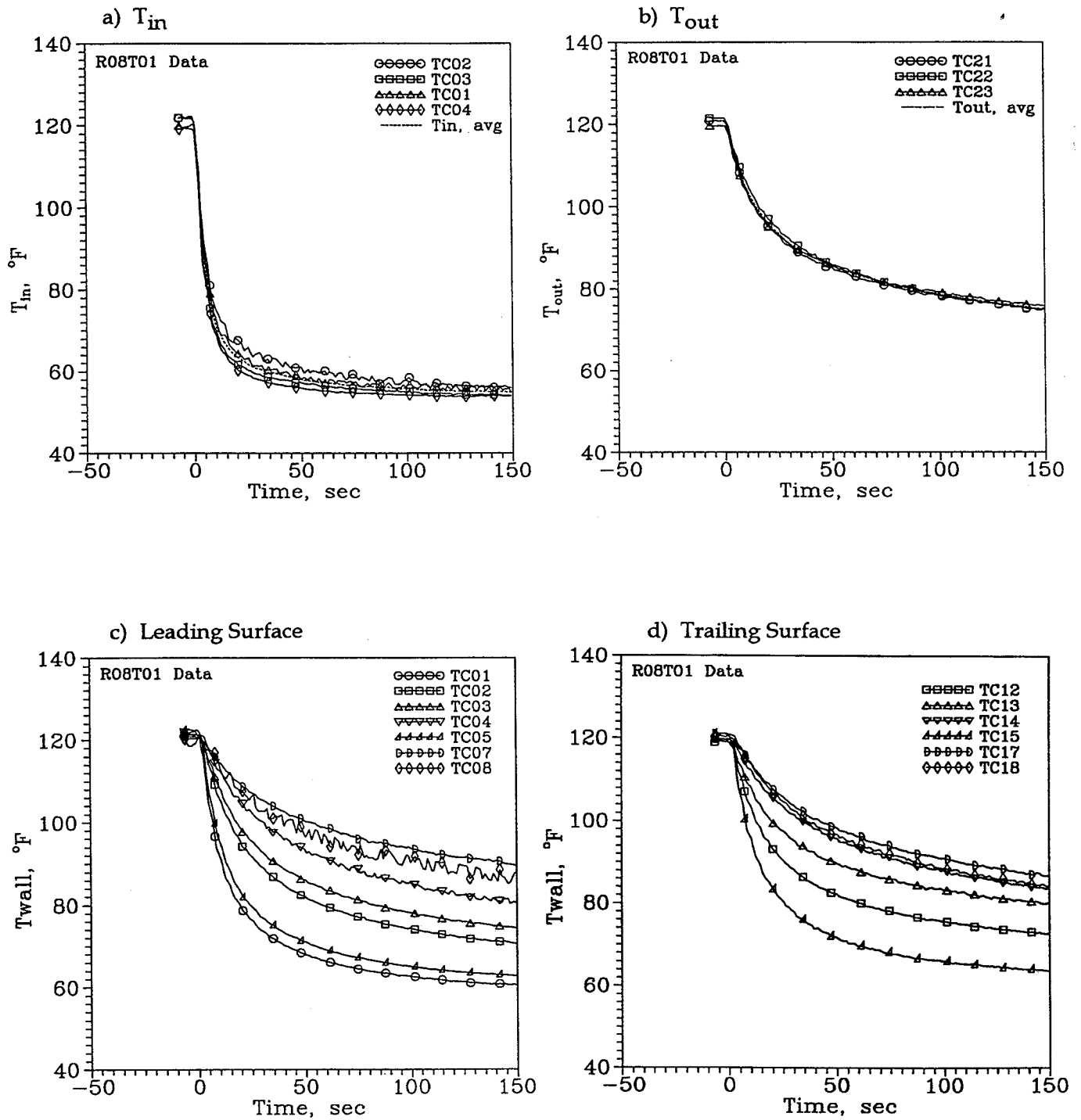


Figure 5-1. Thermocouple Data for Liquid Crystal Test on Leading Surface  
With  $\Omega = 0$  rpm.

Re = 13,000

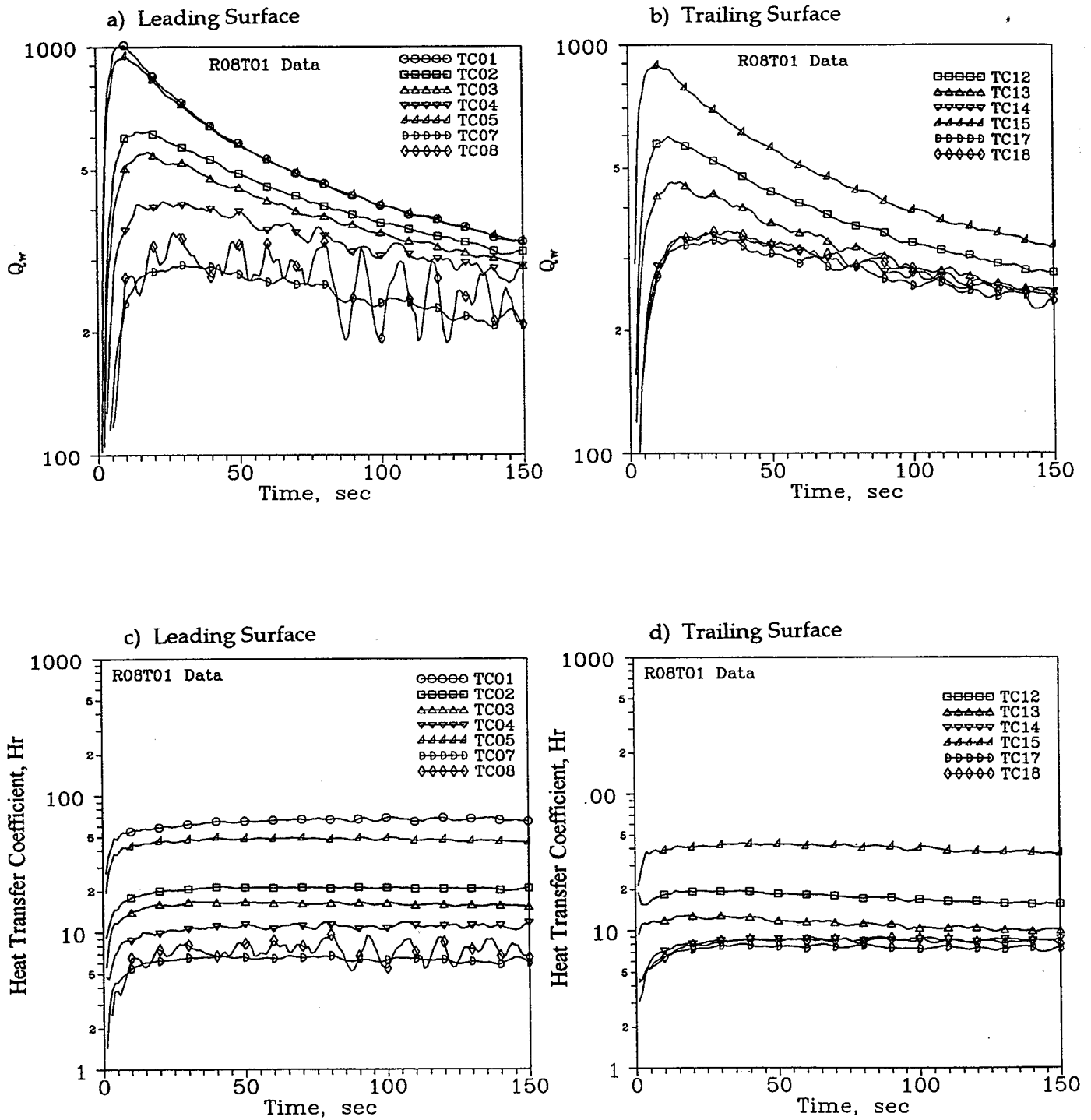


Figure 5-2. Results From Thermocouple Data for Liquid Crystal Test on Leading Surface With  $\Omega = 0$  rpm

Re = 13,000

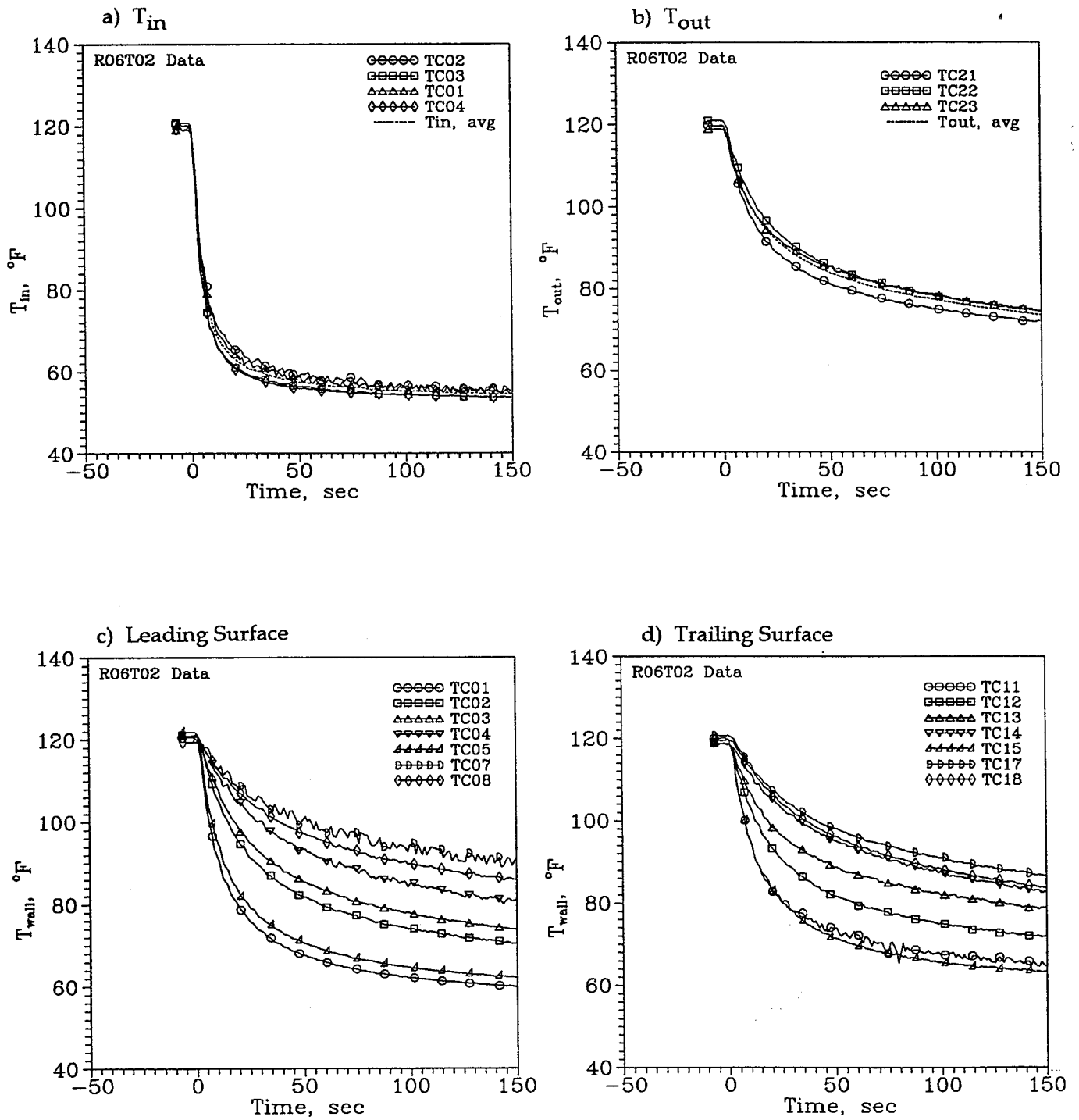


Figure 5-3. Thermocouple Data for Liquid Crystal Test on Trailing Surface  
With  $\Omega = 0$  rpm.

Re = 13,000

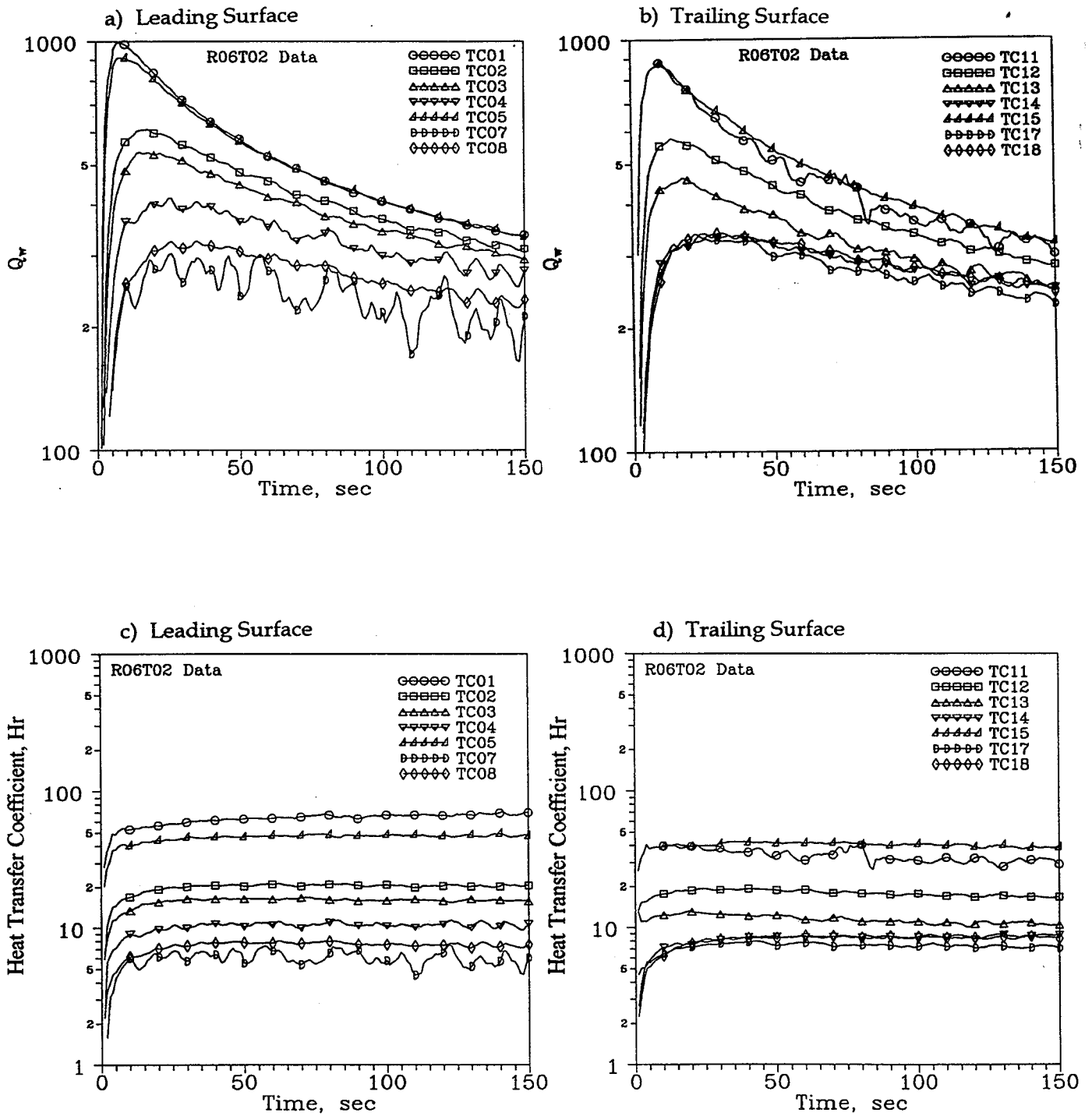


Figure 5-4. Results From Thermocouple Data for Liquid Crystal Test on Trailing Surface With  $\Omega = 0$  rpm.

The data indicate a quick decrease in inlet flow temperature when power to the inlet heater is switched off at Time=0 (Figures 5-1a and 5-3a). For this medium flowrate the time constant of the inlet heater system is approximately 5 seconds. The outlet temperature response (Figure 5-1b) is much slower due to the heat transfer to the coolant from the model walls. The dashed lines in the figures are the smoothed average of the measured inlet and exit flow temperature data. The average coolant temperature records were used for determination of the heat transfer coefficients. The wall temperature records by definition are slower responding than the inlet flow temperature due to the heat capacity of the model walls and the finite heat transfer coefficient. Note that the wall temperature records are not bound by the limits of the outlet coolant temperature. In general, as the shape of a wall temperature trace approaches that of the inlet coolant temperature trace the heat transfer coefficients become large (i.e. towards infinity in the limiting case). Conversely, as the model wall temperature records approach a flat distribution (i.e. constant wall temperature) the heat transfer decreases to zero,

The wall temperature records represent a wide range of time temperature responses indicating various levels of heat flux and, therefore, heat transfer coefficient. The heat flux records (Figure 5-2a and b and Figure 5-4a and b) are characterized by a large increase in heat flux near the start of the test (Time=0) and a general decline as the model wall temperatures approach the coolant temperature.

The heat flux histories are somewhat sensitive to the smoothness of the temperature records. For example, the temperature record for TC08 in figure 5-1c results in heat flux and heat transfer coefficient records which are not as smooth as the other records associated with this test. The unsteadiness of this thermocouple trace is attributed to lead, slip ring, and switch contact irregularities. The unsteadiness was intermittent and was not restricted to specific channels (note TC08 in Figure 5-1c and TC07 in Figure 5-3c). Smoothing of the raw data reduced the effects of the unsteadiness as discussed in Section 3.

The results for the stationary tests show a 10 fold variation in heat transfer in the model depending on the relative location from the inlet. Heat transfer is highest near the two inlet locations (TC01, TC05, TC11, and TC15) and lowest near the exit in the outer passage of Region 4. The large variations noted are due to large differences in local Reynolds numbers and redistribution of flow near the exit of the model passage.

**Rotating Tests** - The data and results for two rotation rates (450 and 750 RPM) are presented in Figures 5-5 through 5-12 in the same format as the results from the stationary tests. Several differences between the operating condition of the stationary and rotating tests should be noted.

It is clear from the thermocouple data for times less than zero (i.e. the initial conditions before the start of the transient portion of the test) that the model did not attain the same level of temperature uniformity for the rotating tests as for the stationary tests. Whereas the initial inlet temperature uniformity was good for all tests, the range of exit temperatures increased from  $\pm 1^{\circ}\text{C}(2^{\circ}\text{F})$  for the stationary tests to approximately  $\pm 3^{\circ}\text{C}(6^{\circ}\text{F})$  for rotating test conditions. The variations noted for the exit flow temperatures are representative of the level at which isothermal conditions were attained in the model prior to the start of the test. This was also indicated in the plots showing the wall temperature data.

Rotation decreased the range of the inlet flow temperature variation after the inlet heater was switched off. The inlet temperature varied from 52 to  $27^{\circ}\text{C}(125^{\circ}\text{F})$  in the rotating tests and from 52 to  $13^{\circ}\text{C}(125^{\circ}\text{F})$  in the stationary tests. The decrease in range is due to increased heat pick up in the rotating air supply system to the model. The combination of rotation and a fixed attainable minimum coolant supply temperature resulted in reduced temperature differences and, consequently, lower values of buoyancy parameter.

The temperature records for the tests with rotation were used to calculate the heat flux histories at each thermocouple location as outlined above. The results shown in Figures 5-5 through 5-12 show that heat transfer was significantly affected by rotation. The most notable effect is the reduction in heat flux from locations in Regions 3 and 4 on the leading surface, (e.g. TC07, see Figures 3-2 and 3-4). The outer portion of Region 3 was especially slow in thermal response which resulted in very low heat flux and heat transfer coefficient.

Some heat transfer coefficient results from tests with rotation show some uncharacteristic behavior, principally, a sharp increase in heat transfer coefficient as time increases from the start of the test (TC01 and TC11) even though the heat flux traces for these locations are consistent compared to the other traces associated with a given test. This characteristic is typically associated with the outer locations of Regions 1 and 2 (i.e. near the inlet of the passage). The sharp increases in the heat transfer coefficient traces are attributed to nonisothermal initial test conditions combined with high heat transfer rates. The wall temperatures for locations in the model with high heat transfer decrease rapidly from the onset of the transient portion of the test. This results in small temperature differences between the wall and the inlet coolant which increases heat transfer coefficients. Additionally, the measured wall temperatures were corrected for conduction and heat storage effects associated with the liquid crystal paint which also contributed to smaller temperature differences. Therefore, results where the temperature difference is greater are expected to be more useful for analyzing the effects of rotation.

Re = 13,000

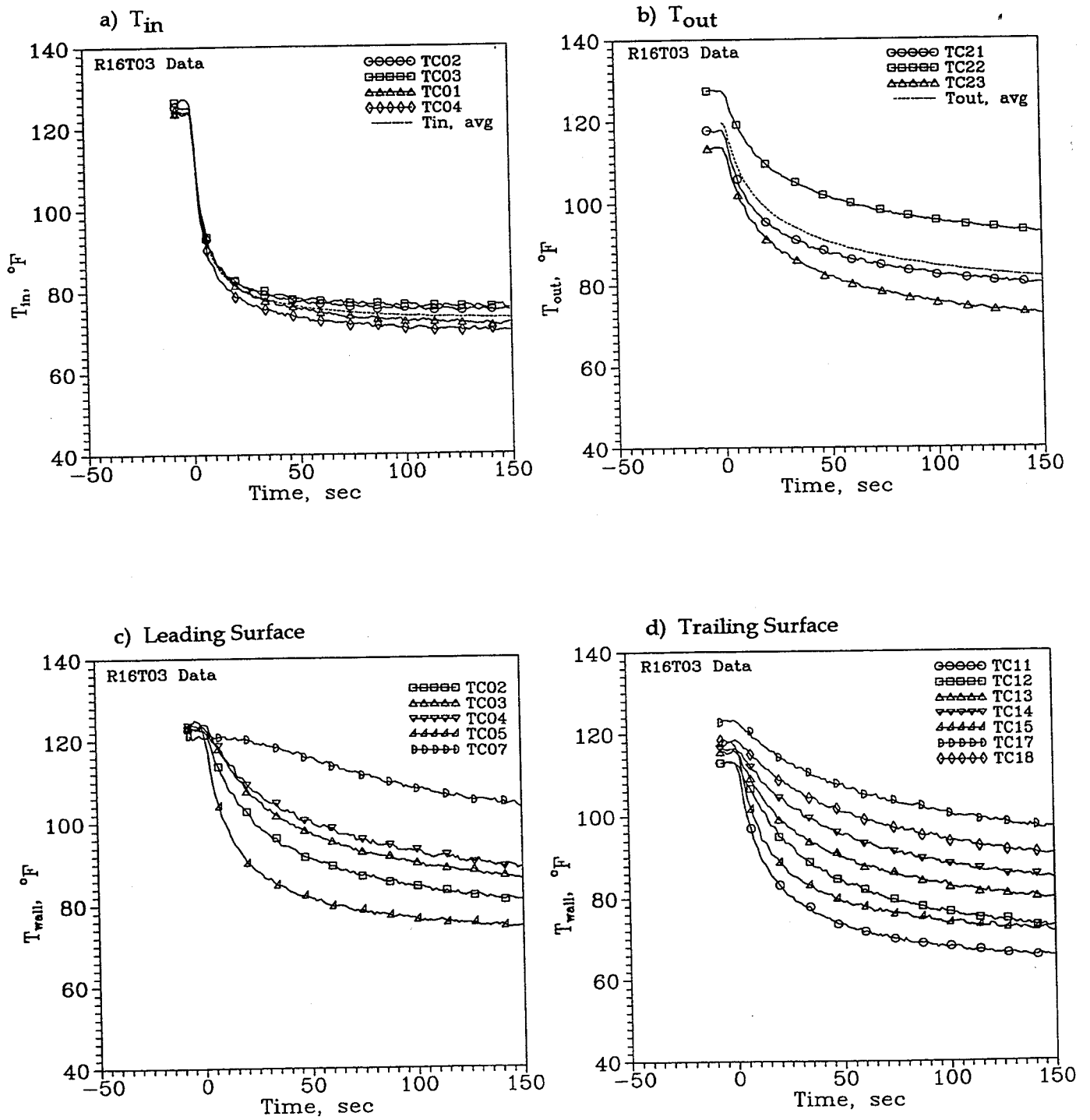


Figure 5-5. Thermocouple Data for Liquid Crystal Test on Leading Surface  
With  $\Omega = 450$  rpm.



$Re = 13,000$

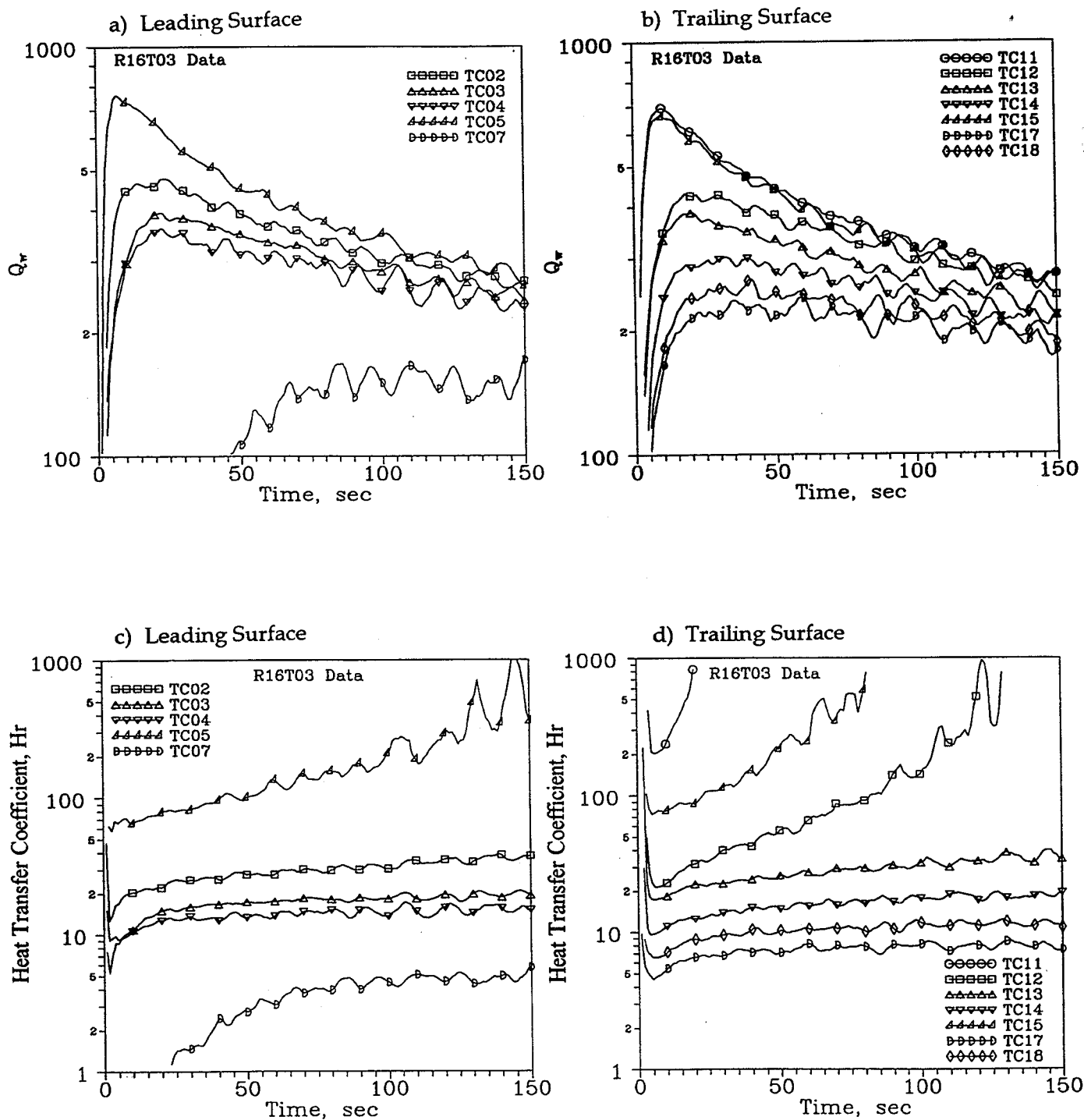


Figure 5-6. Results From Thermocouple Data for Liquid Crystal Test on Leading Surface With  $\Omega = 450$  rpm.

Re = 13,000

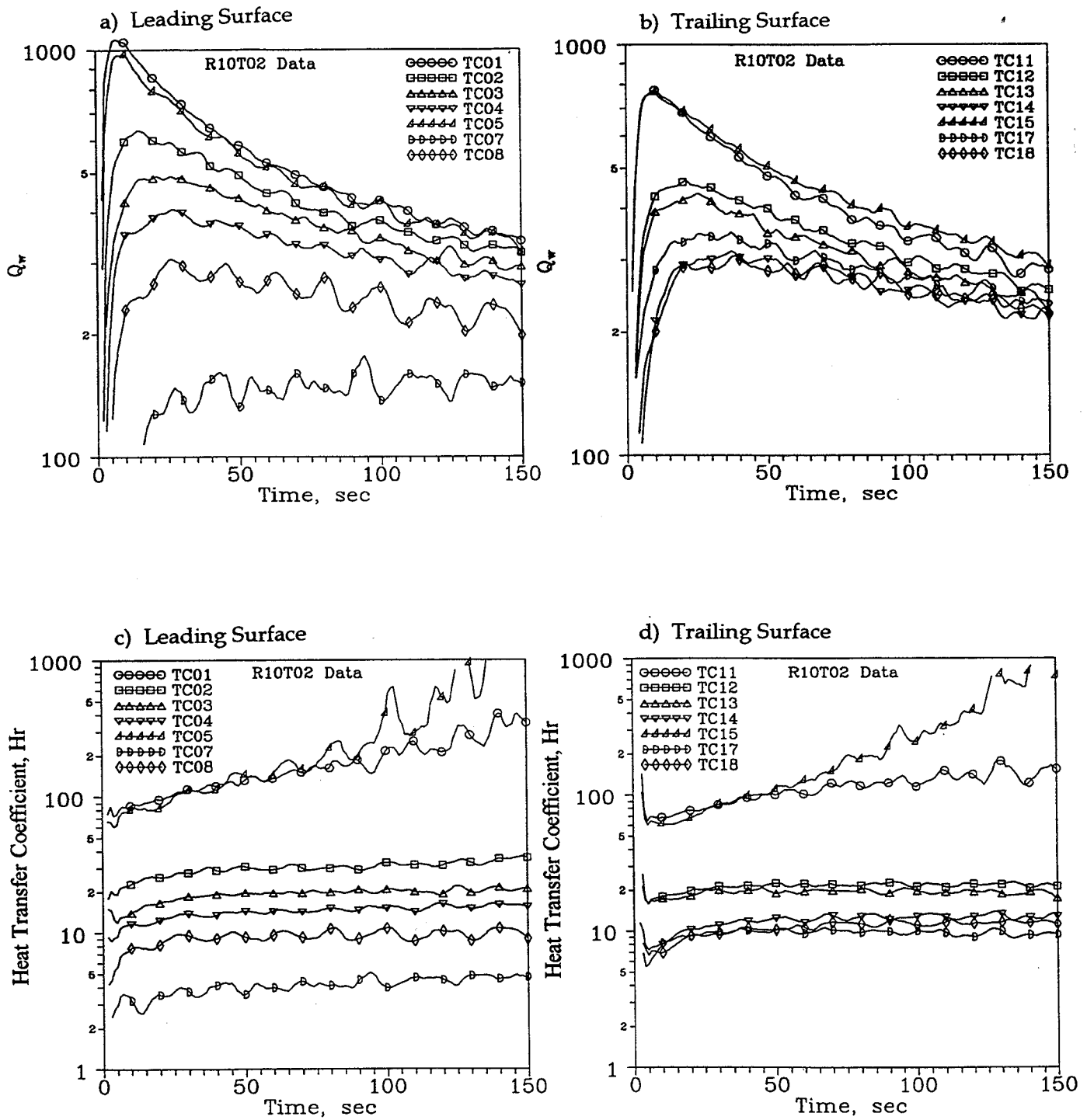


Figure 5-8. Results From Thermocouple Data for Liquid Crystal Test on Trailing Surface With  $\Omega = 450$  rpm.

Re = 13,000

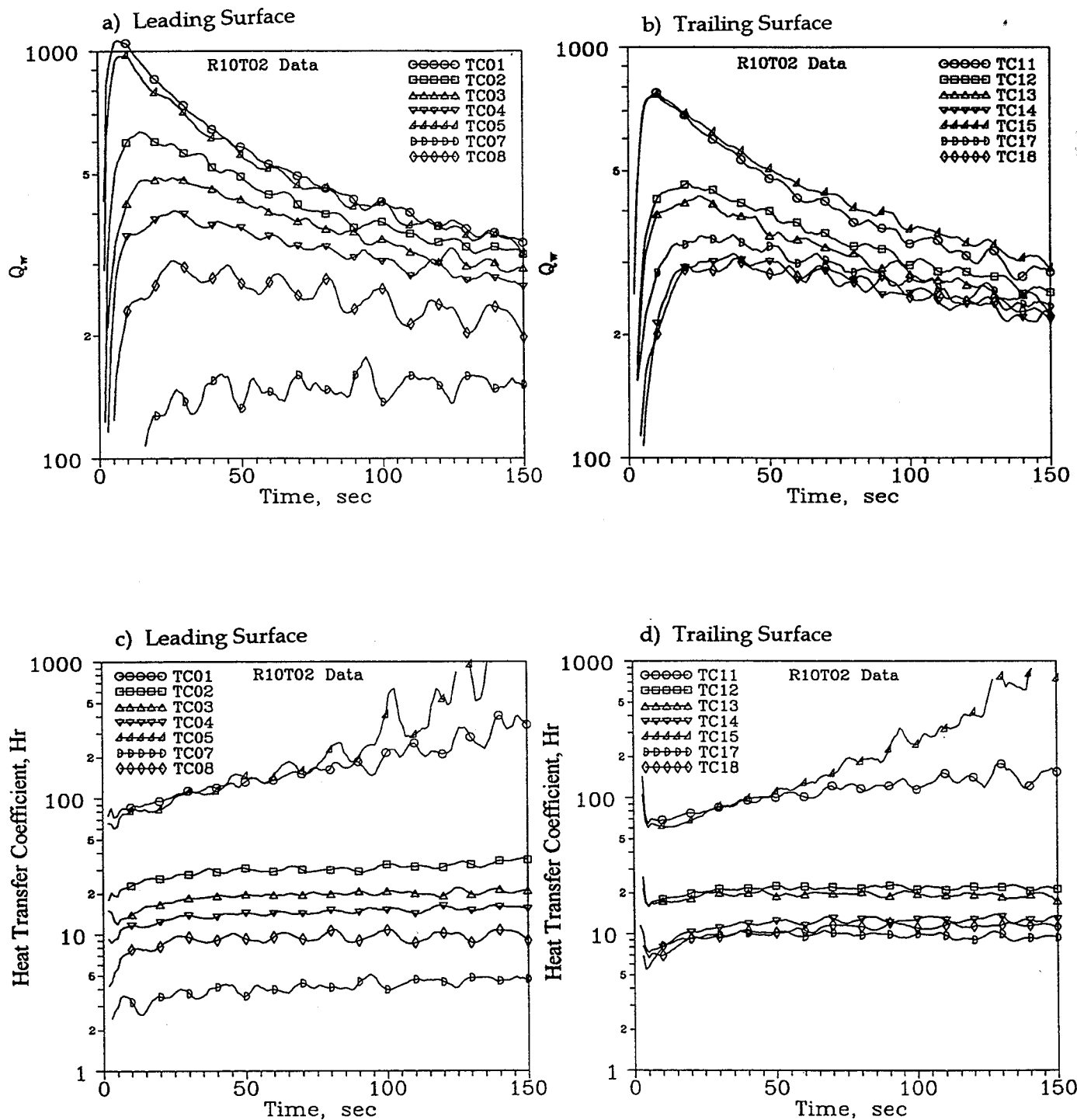


Figure 5-8. Results From Thermocouple Data for Liquid Crystal Test on Trailing Surface With  $\Omega = 450$  rpm.

Re = 13,000

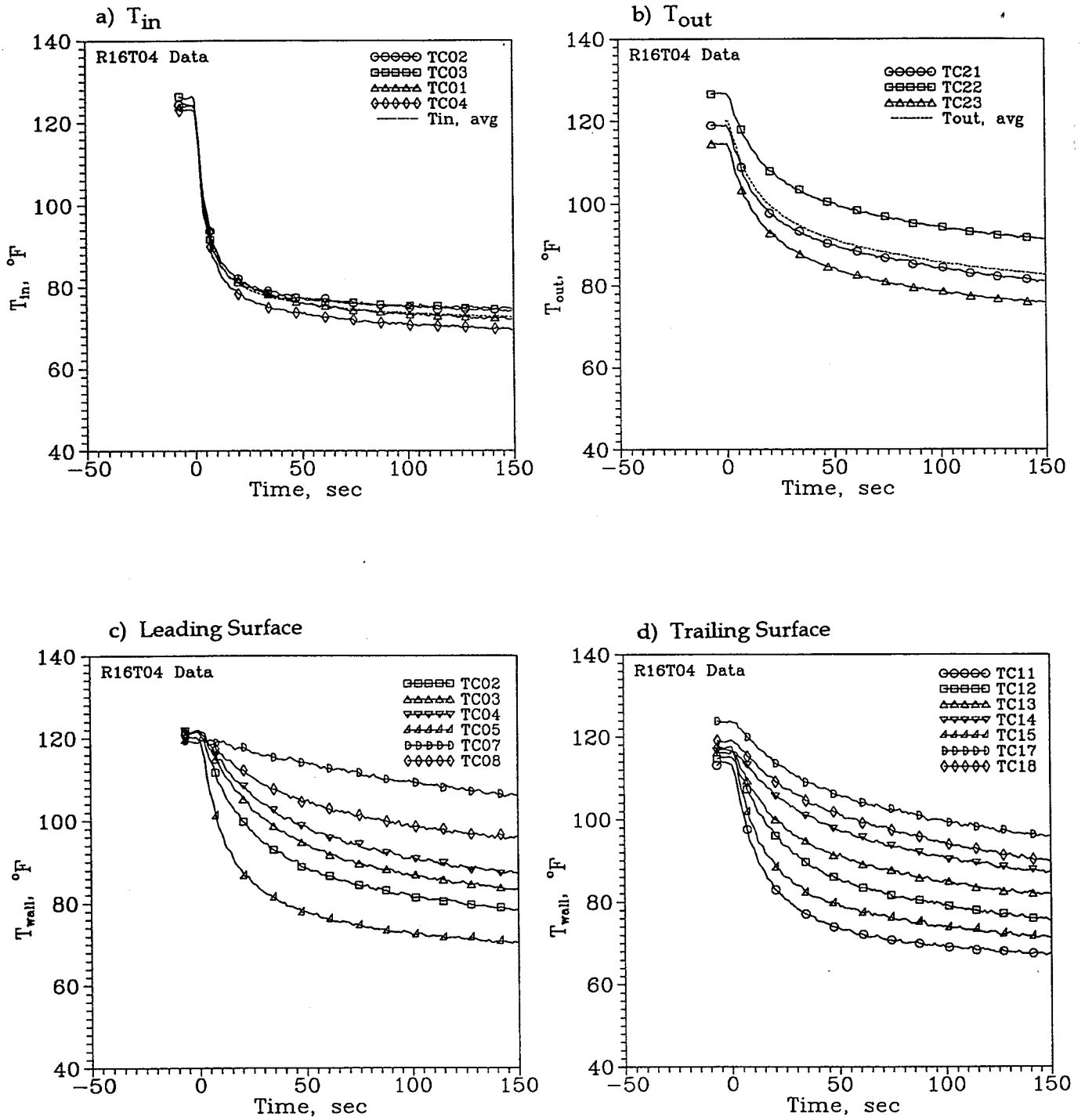


Figure 5-9. Thermocouple Data for Liquid Crystal Test on Leading Surface  
With  $\Omega = 750$  rpm.

Re = 13,000

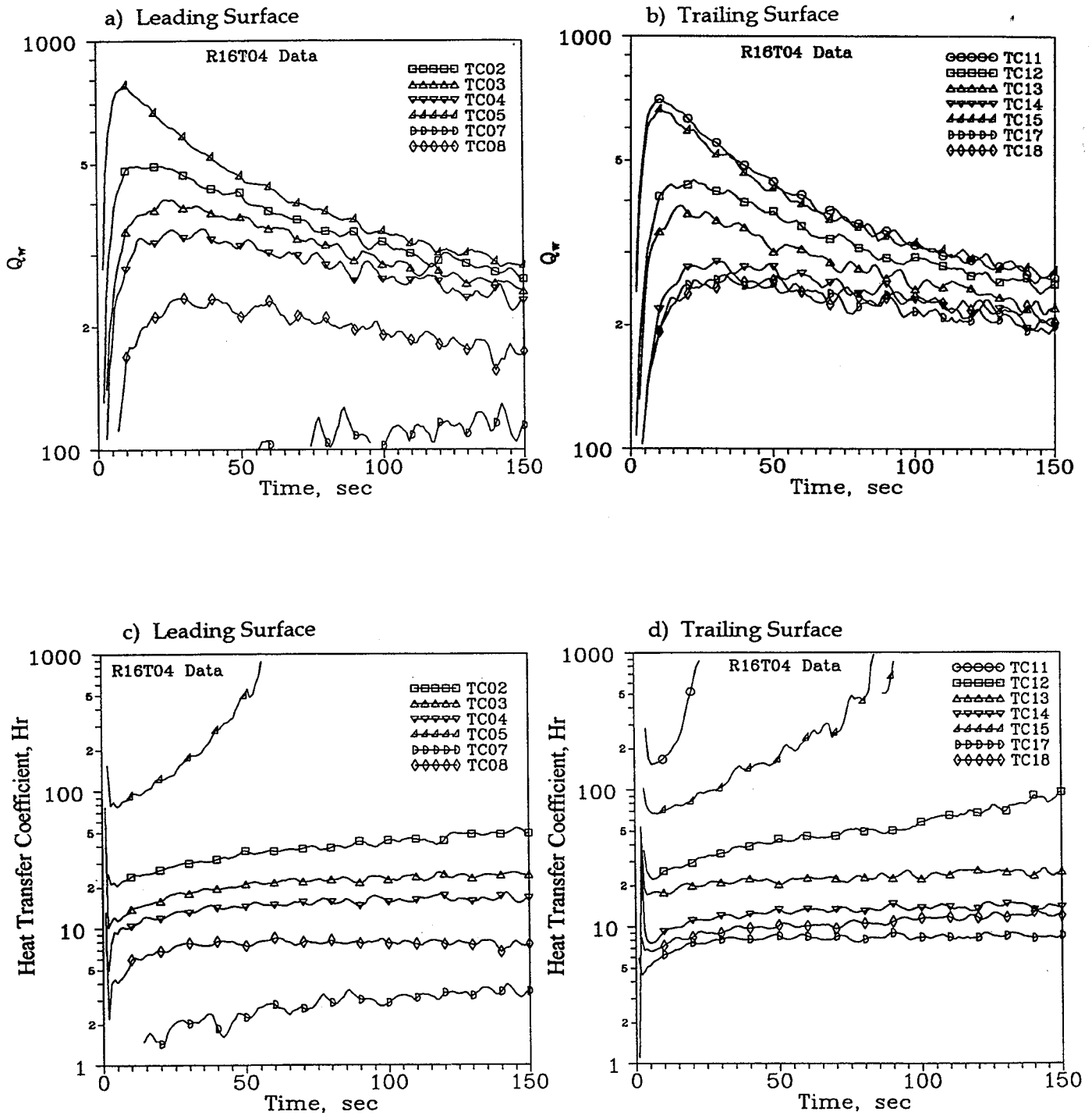


Figure 5-10. Results From Thermocouple Data for Liquid Crystal Test on Leading Surface With  $\Omega = 750$  rpm.

Re = 13,000

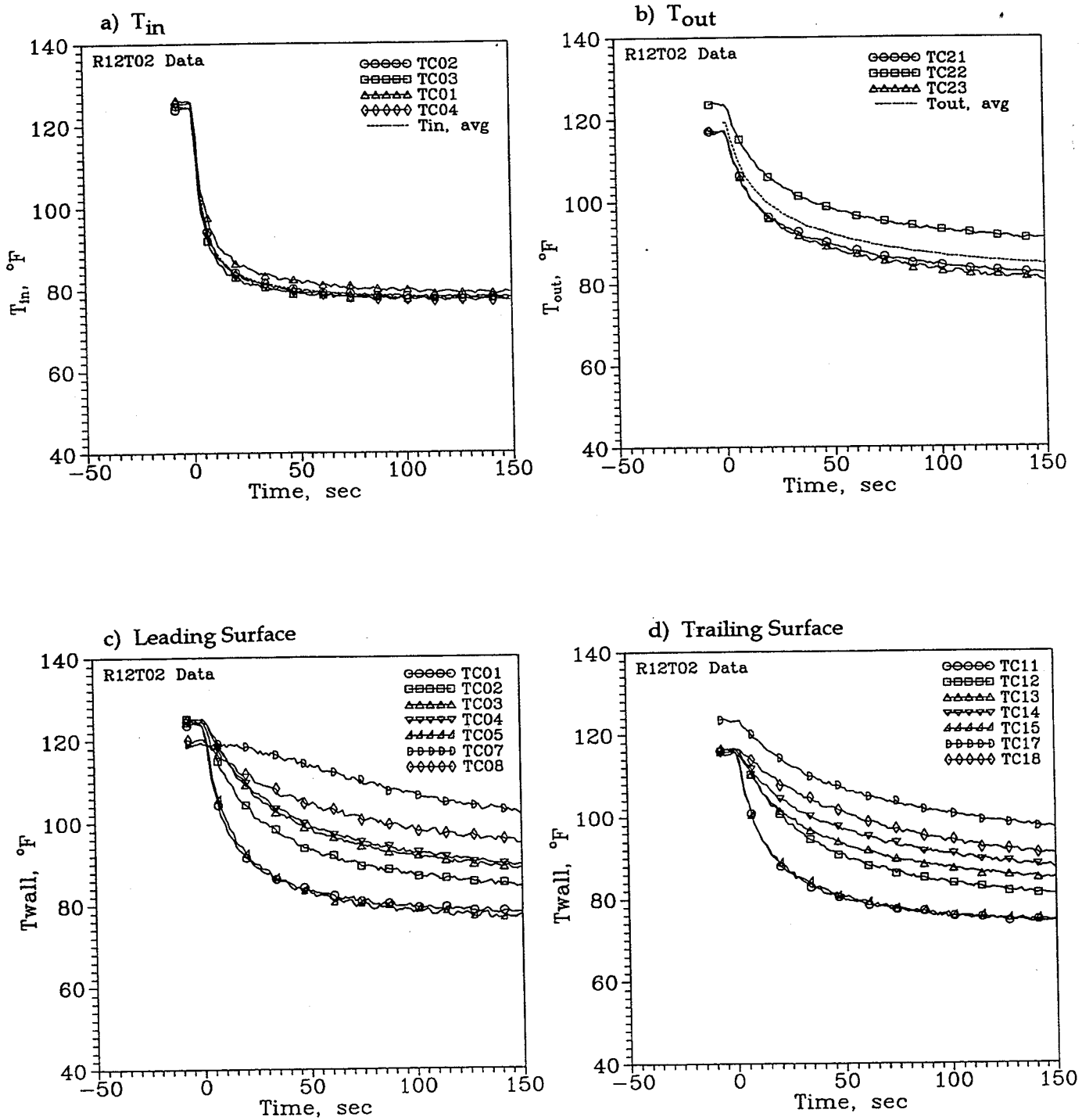


Figure 5-11. Thermocouple Data for Liquid Crystal Test on Trailing Surface  
With  $\Omega = 750$  rpm.

Re = 13,000

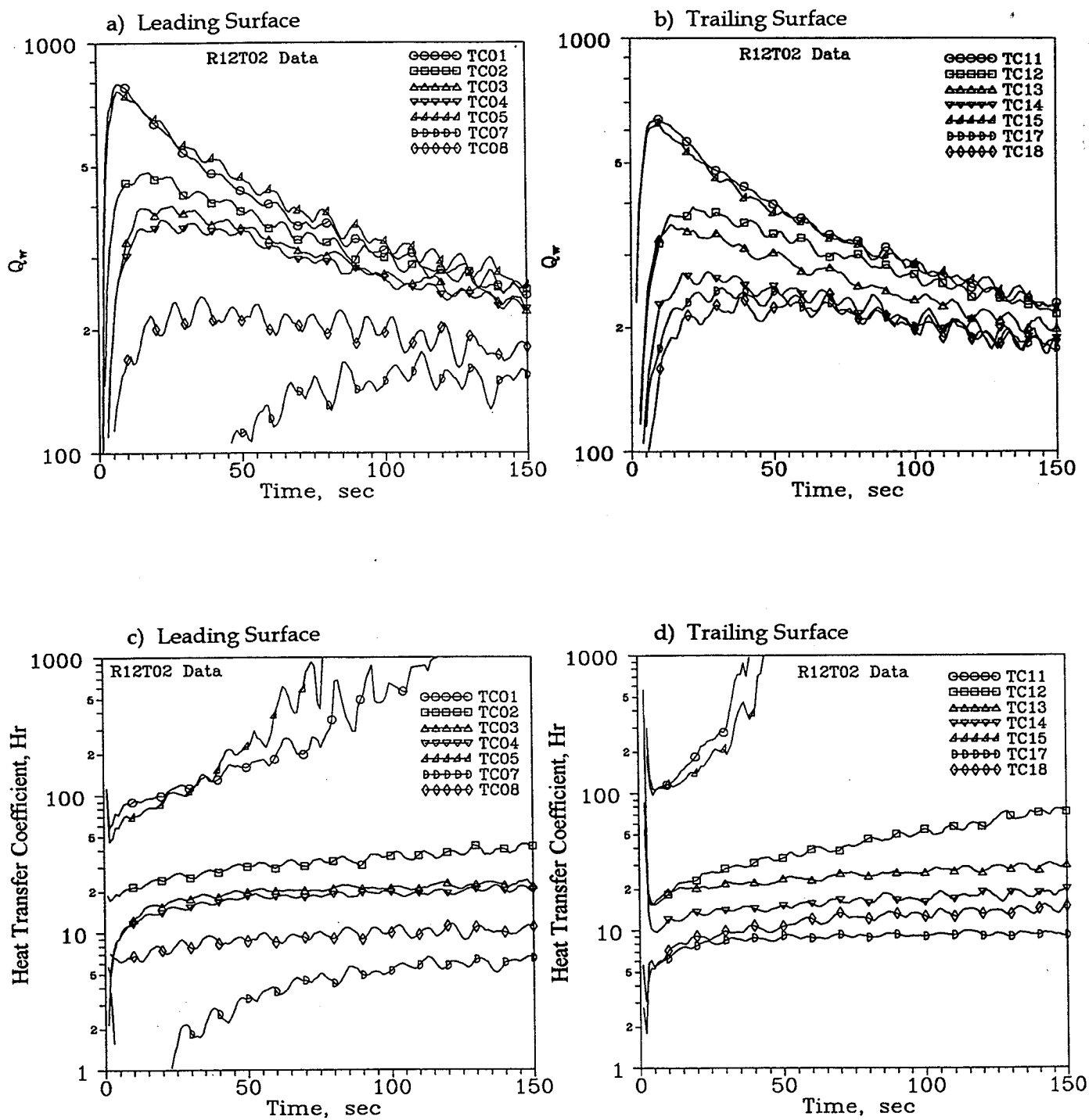


Figure 5-12. Results From Thermocouple Data for Liquid Crystal Test on Trailing Surface With  $\Omega = 750$  rpm.

An adjustment was applied to the measured temperature data. Offsets were applied to normalize the thermocouple results with rotation to the same initial temperature variation as shown for the stationary tests. Temperature offsets from mean model surface and flow temperatures for each thermocouple were calculated from the tests with stationary conditions. These offsets were subsequently applied to the mean model surface and flow temperatures determined for tests with rotation. The corrected results are presented in Appendix 9.4. Note that the heat flux records were essentially unaffected by the temperature offset adjustments.

The adjusted heat transfer coefficient results shown in the appendix are less affected by the small temperature differences associated with the high heat transfer areas as evidenced by the flatter heat transfer coefficient records for TC01, TC05, TC11, and TC15. The effects of rotation on heat transfer are shown in the figures. In general, lesser increases in heat transfer coefficient as a result of rotation are shown in the adjusted results compared to the nonadjusted results. However, the large decrease in heat transfer in certain model areas with rotation are still predicted for the low heat transfer areas (i.e. TC07). The effects of rotation on heat transfer are more clearly shown in the following section for two elapsed times after the beginning of the transient portion of the test.

## **5.2 Effects of Rotation on Local Heat Transfer**

The adjusted heat transfer coefficient records for the medium (0.0075 lbm/sec) coolant flowrates for all rotation rates are presented in Figures 5-13 through 5-18. Additionally, the heat transfer ratio,  $Nu/Re^{0.8}$ , at 10 and 30 seconds from the start of the test are compared as a function of rotation number for the three coolant flowrates and the three rotational rates, i.e. stationary, 450 RPM, and 750 RPM. Adjusted results, as described above, are presented in this section and subsequent sections.

**Region 1 - Tip Section** - The adjusted heat transfer coefficients for Location 1 (Figure 5-13a, leading surface) with medium flow and RPM = 0 are essentially identical, indicating repeatability for this flow condition. The heat transfer coefficients for the two tests with medium flow and rotation are approximately 60 to 100 percent greater than those for RPM = 0. The effect of rotation on heat transfer ratio is shown in Figure 5-13c. These results show an increase in heat transfer (consistent with the medium flow heat transfer coefficient results, Figure 5-13a) at moderate values of rotation number (i.e.  $Ro$  less than 0.1) and then a subsequent decrease for larger Rotation numbers. The increase in heat transfer coefficient is not consistent with the previous results from Guidez, 1989, or Wagner et al., 1991, where the heat transfer on the leading surface of coolant passages with flow outward decreased with rotation. It is likely that the increase in heat transfer at the moderate to high flowrates results from secondary flows in the inlet duct and the continuation of these secondary flows in the coolant passage.



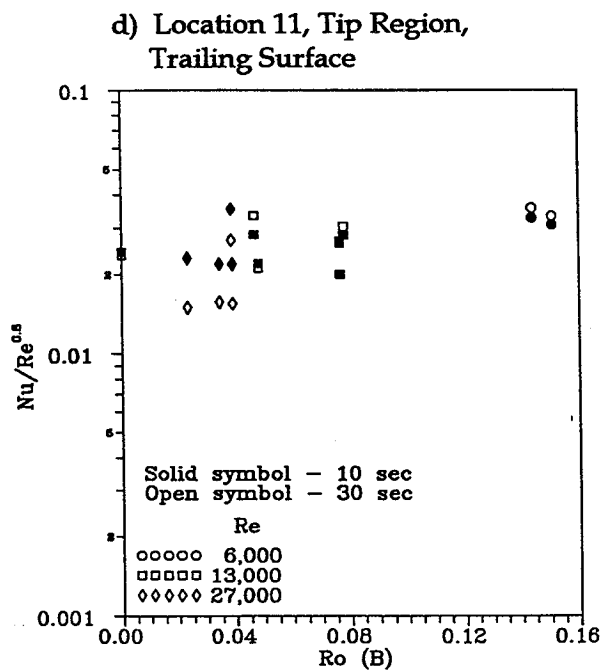
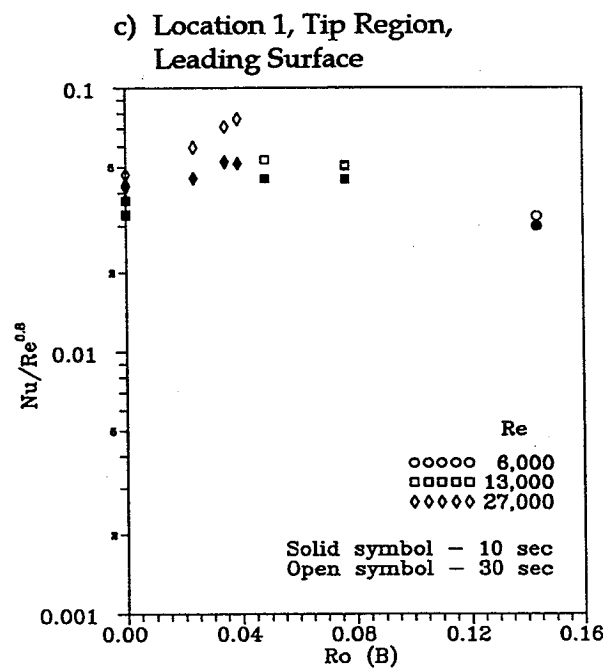
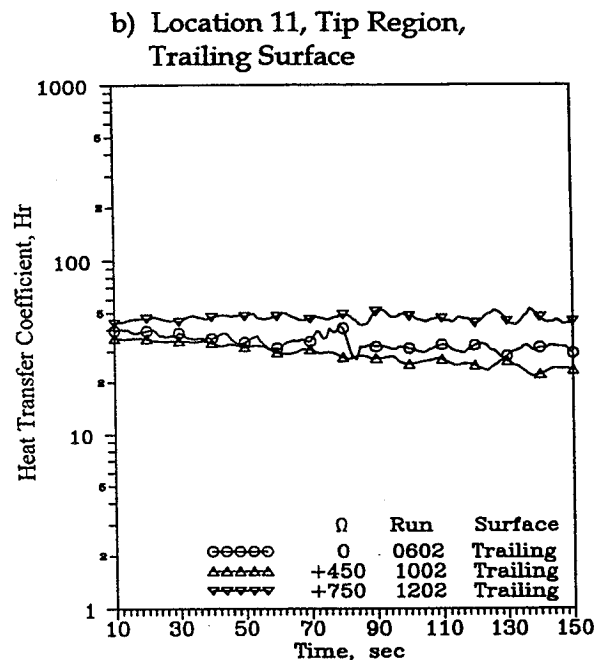
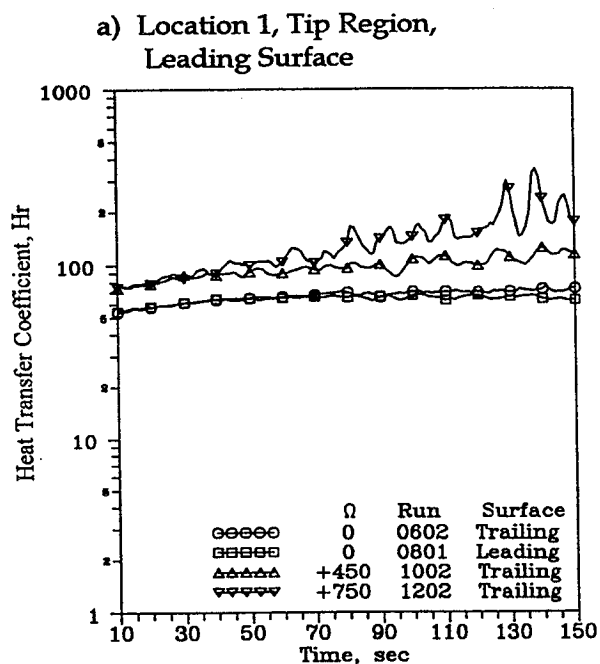


Figure 5-13. Dimensional and Dimensionless Heat Transfer Results From Thermocouple Data for Region 1.

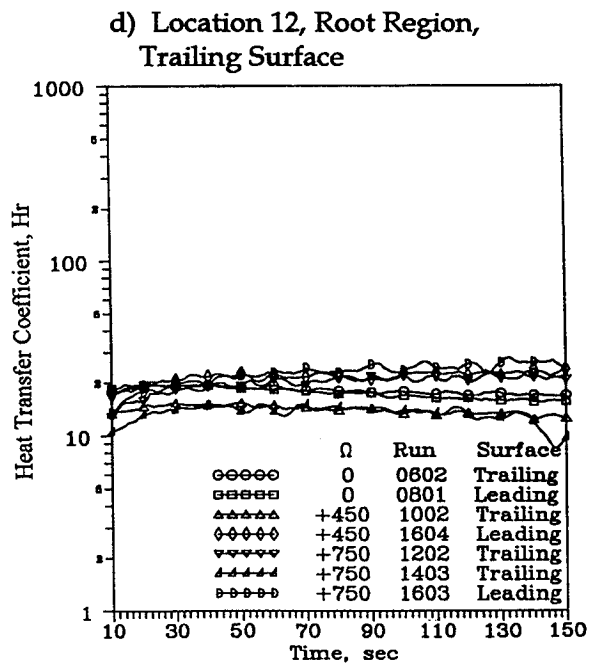
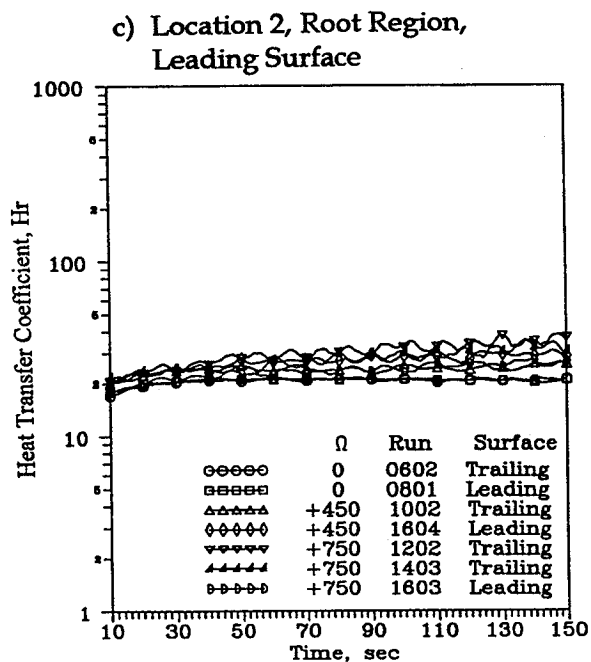
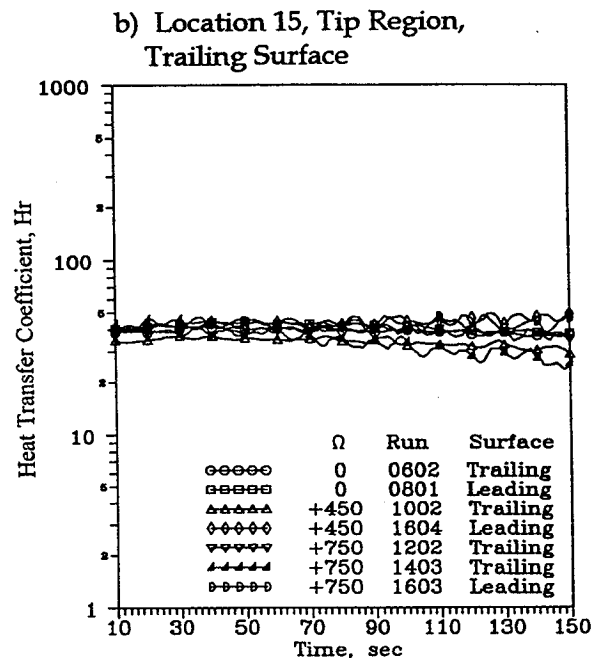
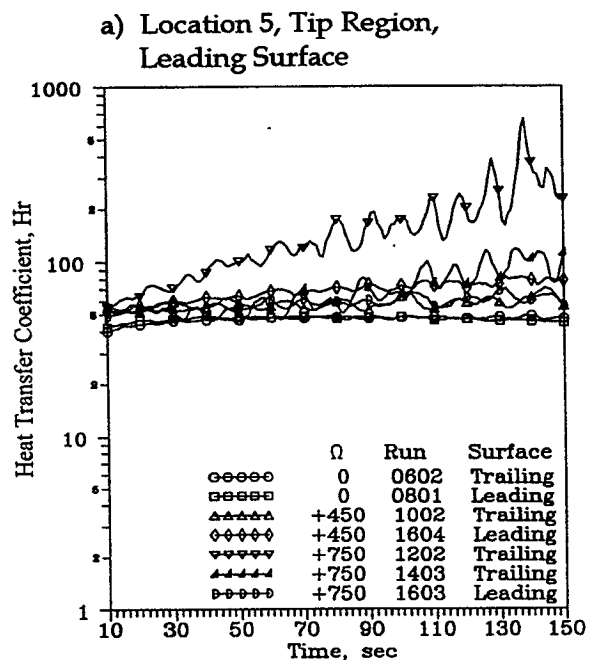


Figure 5-14. Dimensional Heat Transfer Results From Thermocouple Data for Region 2 and  $Re = 13,000$ .

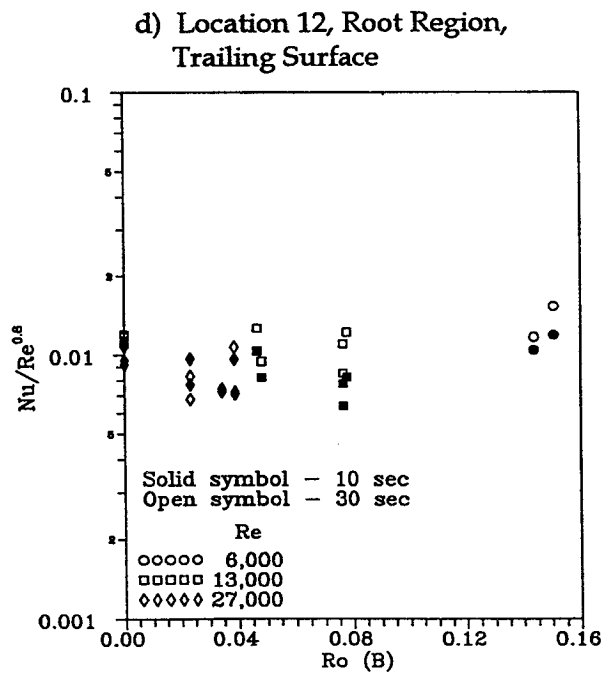
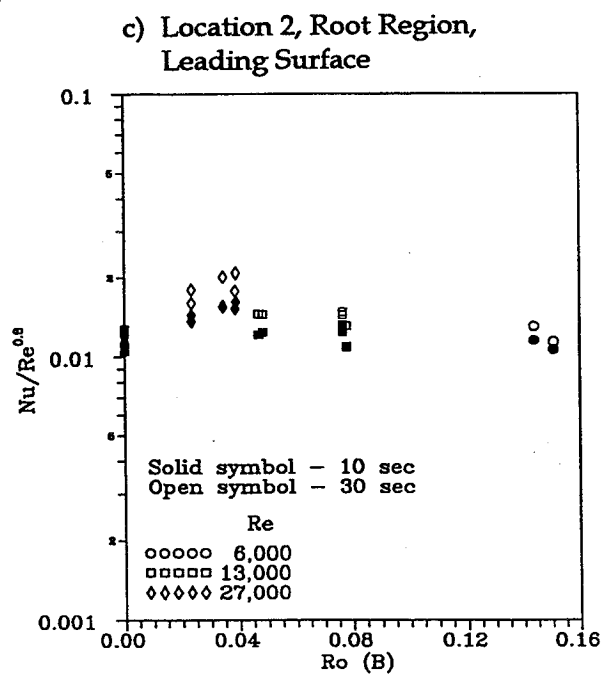
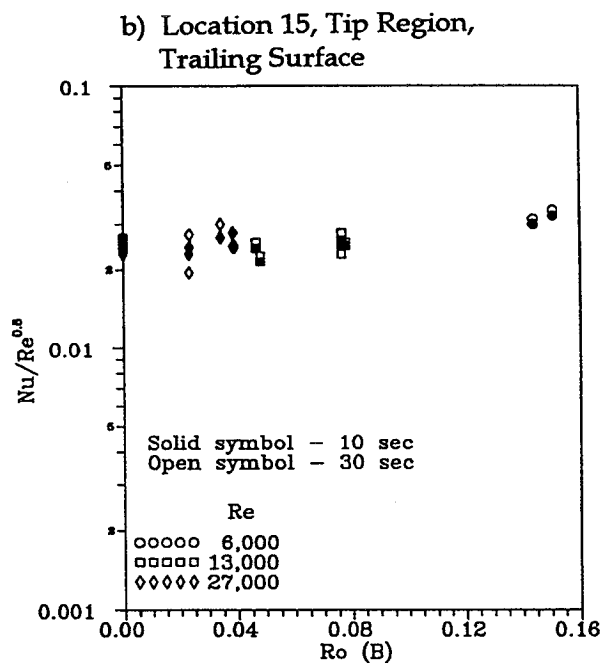
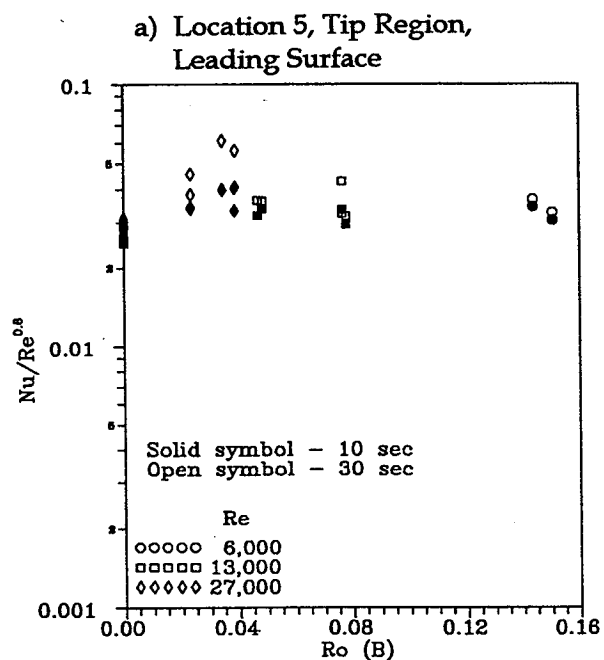


Figure 5-15. Dimensionless Heat Transfer Results From Thermocouple Data for Region 2.

The results for Location 11 (Figure 5-13b and d, trailing surface, tip region) are generally similar to previous studies (e.g., Hajek et al., 1991). Heat transfer coefficient and heat transfer ratio are shown to increase, on the order of 50 percent, with increases in rotation number, especially for the low to moderate flowrates.

The general conclusion from the analysis of the heat transfer results from Region 1 are that the effect of rotation is consistent with earlier results where heat transfer decreases on the low pressure side of the passage and increases on the high pressure side. However, this only appears to be consistently true for the low flowrate. Note that the previous experience is generally limited to Reynolds numbers of 50,000 and below. The high flowrate case of the present program results in a local Reynolds number significantly greater than previous experience (over 70,000). Considering that inlet flow effects may be convecting into the coolant passage for the high flowrate cases, it is inappropriate to generalize the effect of rotation on the heat transfer results for Region 1.

Region 2 - Tip Section - The calculated heat transfer coefficient,  $h_r$ , for the medium flowrate (Figure 5-14a) increased significantly with rotation for TC Location 5 (tip leading surface). The calculated coefficients at 10 seconds were approximately 25 percent greater than the stationary values and generally increased with time. Heat transfer on the trailing surface (TC Location 15, Figure 5-14b) for the medium flowrate is much less affected by rotation. Heat transfer is shown to increase and decrease with rotation compared to the stationary results. Additionally, the results are uncorrelated with rotation rate. The effect of rotation number on heat transfer is shown in Figure 5-15a and b. Heat transfer ratio is shown to increase with increases in rotation number on the leading and trailing surfaces. Whereas the increase in heat transfer on the leading surface is pronounced at the low and moderate rotation numbers, the effect of rotation on heat transfer on the trailing surface is minimal. In general, heat transfer ratio for all flowrates increased or stayed the same with rotation. These results had high heat transfer coefficients as expected from previous results. The local streamwise velocities are high and a great deal of turbulence and vorticity downstream of the turn is expected. The conclusion from these comparisons is that the vorticity in the channel is increased significantly due to rotation.

Region 2 - Root Section - The results from TC Location 2 at the root on the leading surface with the medium flowrate and radially inward flow (Figure 5-14c) are compatible with Hajek et al., 1991. Heat transfer coefficients increase on the leading surface approximately 50 percent with rotation. The results for TC Location 12 at the root on the trailing surface appear anomalous (as discussed above for

the tip section) compared with the values for stationary conditions. Heat transfer coefficient is shown to increase and decrease with rotation but is uncorrelated with the rotation rate. The effect of rotation number on the heat transfer ratio is shown in Figure 5-15c and d for the root section of Region 2. The results on the leading surface generally increase with rotation number for low to moderate values of rotation number and then subsequently decrease to the same level of heat transfer ratio measured for the stationary tests. The trend of the trailing surface results is opposite to that of the leading surface such that heat transfer ratio generally decreases with rotation number for low to moderate values of rotation and then subsequently increases to the same level of heat transfer ratio measured for the stationary tests.

The conclusion from the analysis of the heat transfer coefficient and heat transfer ratio results from Region 2 is that heat transfer increased and decreased significantly with rotation on the leading and trailing surfaces especially for the medium to high flowrate test conditions.

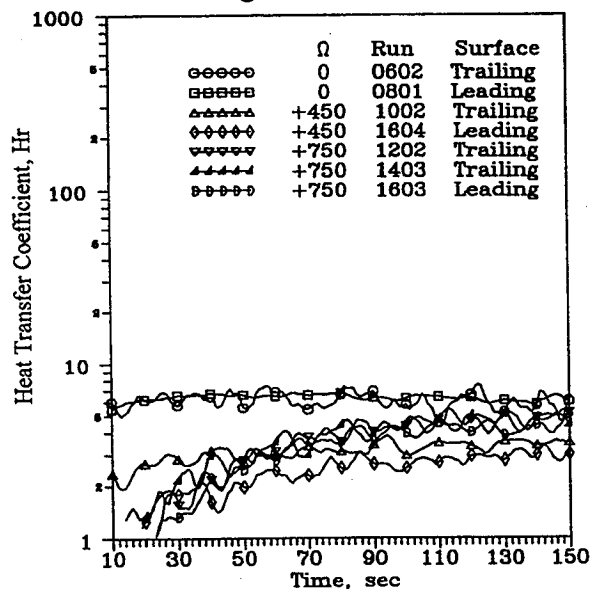
Region 3 - Tip Section - The tip, leading surface of Region 3 (TC Location 7, Figures 5-16a and 5-17a) was the only region that had consistently lower heat transfer with rotation. The heat transfer in this region with rotation was as low as 10 to 30 percent of that with no rotation. Heat transfer on the trailing surface (TC Location 17, Figures 5-16b and 5-17b) is less affected by rotation compared to the leading surface. However, heat transfer is shown to increase slightly and then decrease with an increase in the rotation number.

Region 3 - Root Section - The heat transfer in the root region of Region 3 (Figures 5-16c and d and 5-17c and d) is shown to increase slightly and then decrease with rotation number on the leading and trailing surfaces. These results are inconsistent with Coriolis driven secondary flows and are likely affected by more complex rotation induced flow structures.

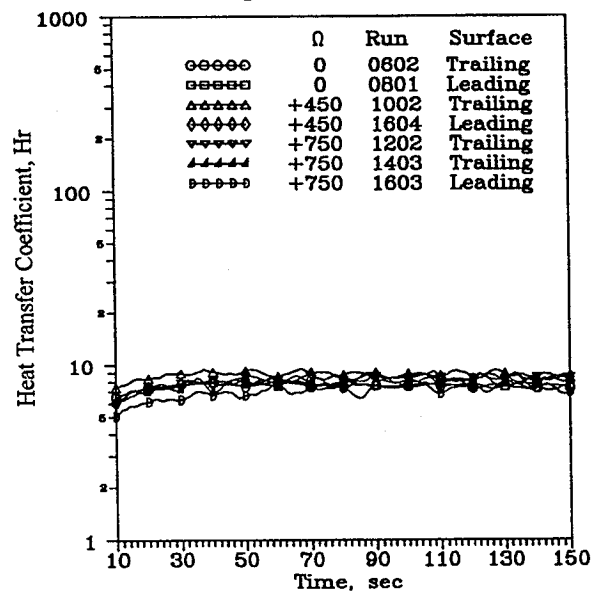
The general conclusion from the analysis of the heat transfer results obtained in Region 3 is that the heat transfer is strongly affected by rotation especially in the tip section where heat transfer was substantially reduced.

Region 4 - Tip section - The heat transfer on the leading and trailing surfaces in the tip region of Region 4 (TC Location 8 and 18, Figures 5-18a and b and 5-19a and b) was relatively unaffected by rotation. This relative insensitivity to rotation would be expected when the flow is axial and the stream tubes do not change radius.

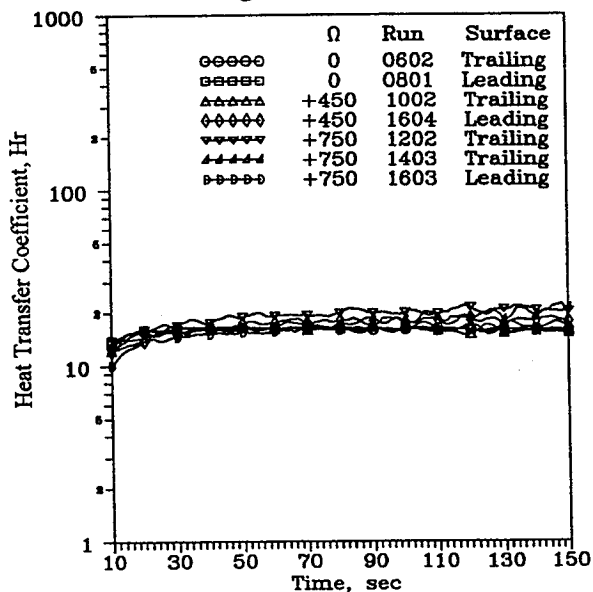
a) Location 7, Tip Region,  
Leading Surface



b) Location 17, Tip Region,  
Trailing Surface



c) Location 3, Root Region,  
Leading Surface



d) Location 13, Root Region,  
Trailing Surface

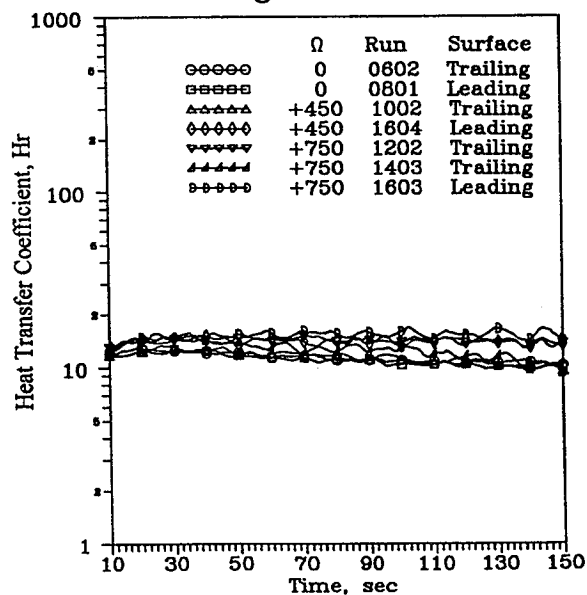


Figure 5-16. Dimensional Heat Transfer Data From Thermocouple Data for  
Region 3 and  $Re = 13,000$ .

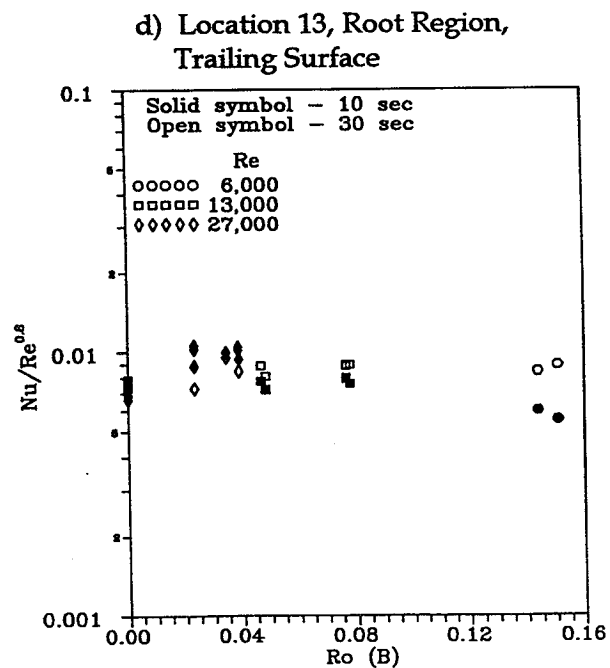
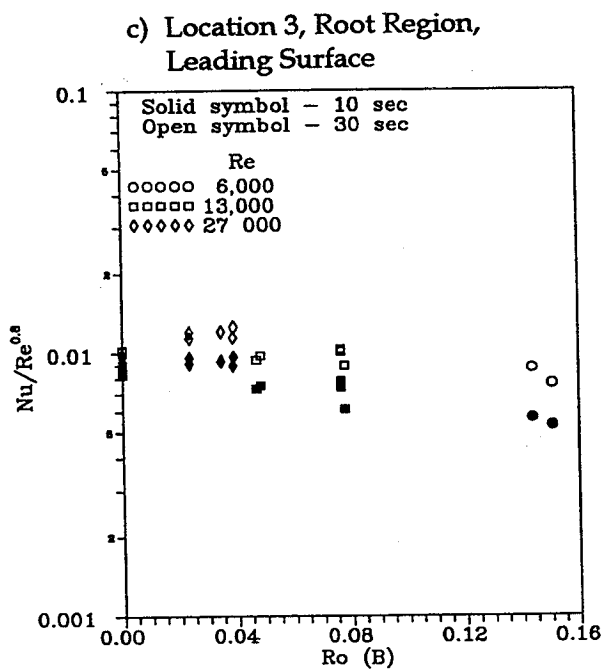
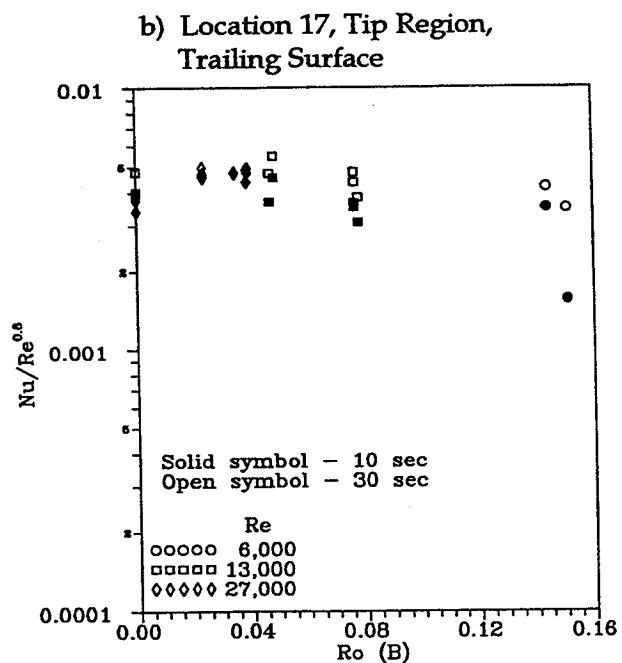
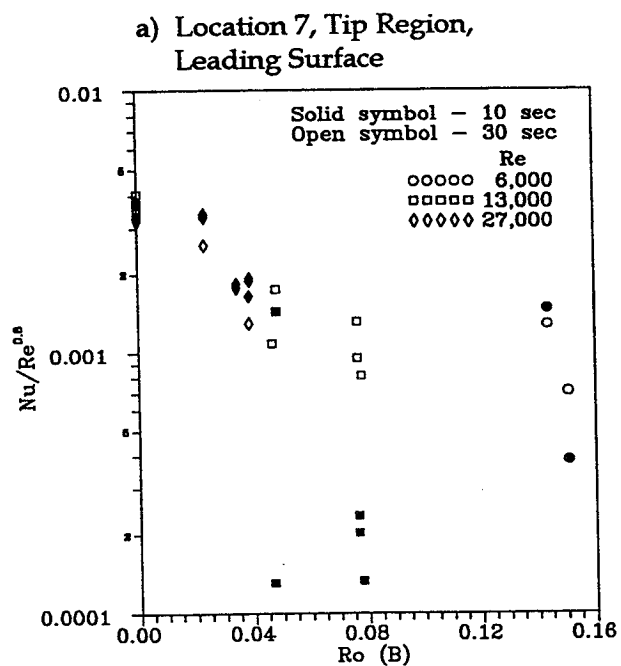
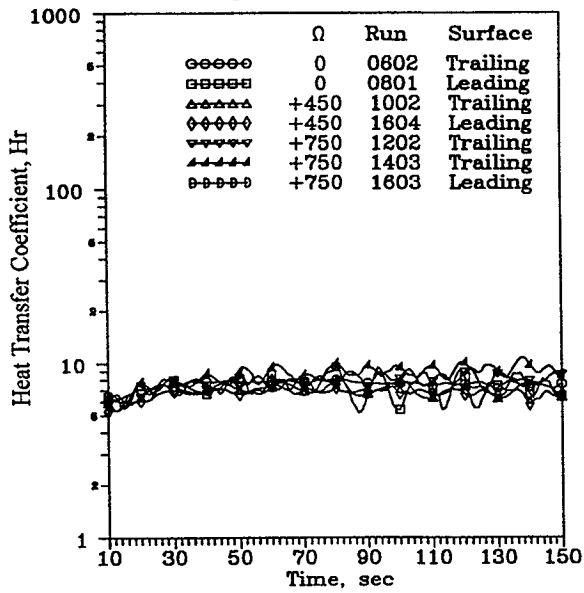
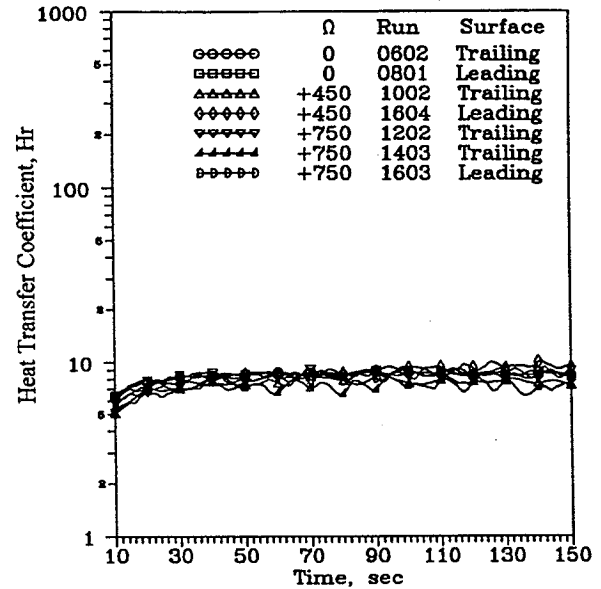


Figure 5-17. Dimensionless Heat Transfer Data From Thermocouple Data for Region 3.

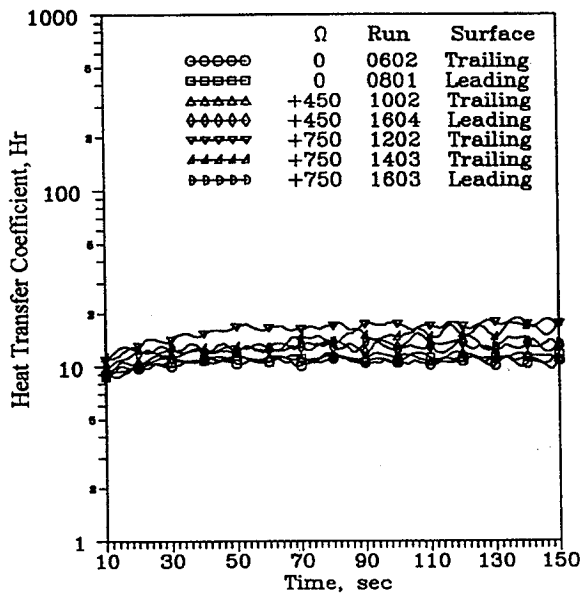
a) Location 8, Tip Region,  
Leading Surface



b) Location 18, Tip Region,  
Trailing Surface



c) Location 4, Root Region,  
Leading Surface



d) Location 14, Root Region,  
Trailing Surface

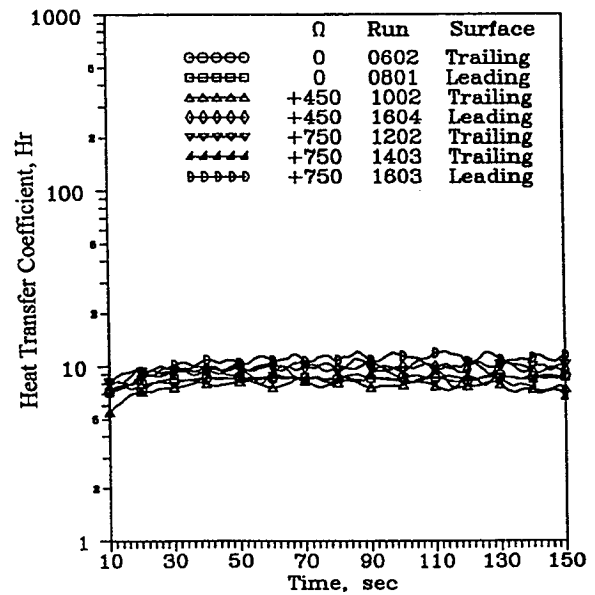


Figure 5-18. Dimensional Heat Transfer Data From Thermocouple Data for Region 4 and  $Re = 13,000$ .



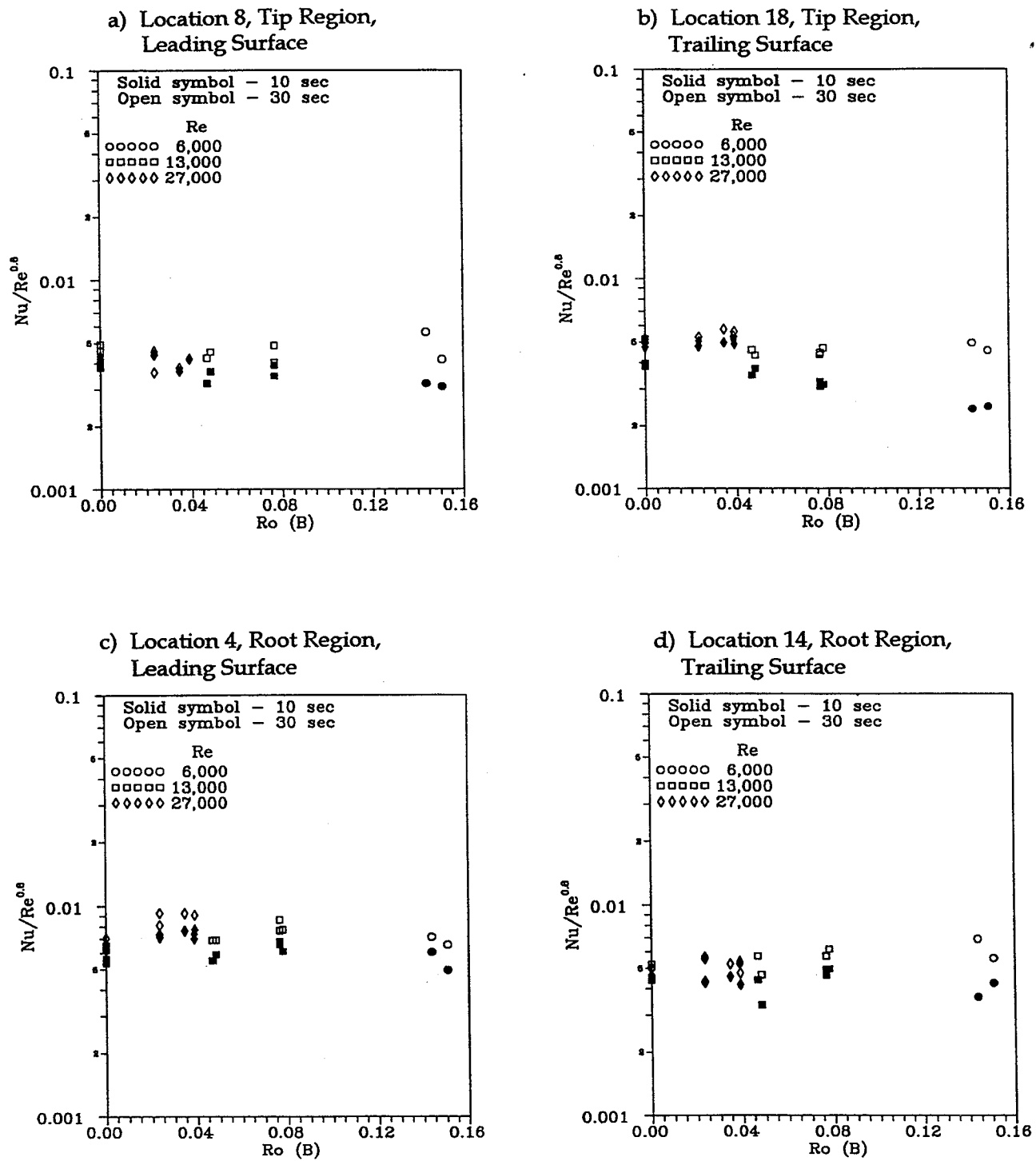


Figure 5-19. Dimensionless Heat Transfer Data From Thermocouple Data for Region 4.

Region 4 - Root Section - The heat transfer for TC Locations 4 and 14 (Figures 5-18c and d and 5-19c and d) are also relatively unaffected by rotation. One could conjecture that an increase in heat transfer ratio occurred with an increase in rotation number at low rotation numbers on the leading surface. However, the increased heat transfer ratio results are for the high flowrate case only which might suggest a flow redistribution effect rather than a rotation induced flow phenomena.

The conclusion from the analysis of the heat transfer results from Region 4 is that rotation effects are minimal when the flow is predominately axial. Any heat transfer differences with rotation are more likely to be the result of a flow redistribution between the three exiting flow streams rather than by a rotation induced secondary flow.

### **5.3 Summary of Results from Thermocouple Measurements**

- ☐ The heat transfer coefficients in the tip section of Regions 1 and 2 are at least twice as much as those in other regions of the coolant passage.
- ☐ Heat transfer in Regions 1 and 2 are significantly affected by rotation. The results are generally consistent with previous studies where heat transfer increases on the high pressure side of a passage and decreases on the low pressure side.
- ☐ The affects of rotation are most pronounced on the leading surface of the tip section of Region 3. Heat transfer decreased to a level of 10 to 30 percent of stationary levels when the model was rotating. The consequence of this result is that this region of the airfoil is essentially uncooled. The low heat transfer in this region is attributed to a redistribution of the coolant flow which results in a large recirculating stall cell.
- ☐ The heat transfer in Region 4 with axial flow was less affected by rotation than Regions 1, 2, or 3.

## 6.0 HEAT TRANSFER RESULTS FROM LIQUID CRYSTALS

The video records for fifteen combinations of model orientation and flow conditions of transient heat transfer tests are available from the NASA LeRC. Used in conjunction with the thermocouple data for the same tests, such as that presented in Section 5, these video data might be used to evaluate codes for predicting conjugate heat transfer in complex coolant passages. The results also show the shapes of the constant heat flux contours and provide insight, through inference of the flow structure in the coolant passages.

Because the transient heat flux and temperature distributions do not lend themselves to easy interpretation, those data were used, along with the thermocouple data, to develop heat transfer coefficient contours. Corresponding flow parameters for the selected tests for several locations in the model coolant passage (Figure 3-2) are presented in Appendix 9.2.

The temperatures measured with the liquid crystals on the stationary model were in good agreement, i.e.  $\pm 0.5^\circ\text{C}$  ( $1^\circ\text{F}$ ), with the thermocouple measurement for stationary test conditions. The temperature calibration of the liquid crystals changed considerably during rotation. The liquid crystals are known to be sensitive to shear stresses which will occur due to the centrifugal force on the liquid crystals due to its own weight and that of the black overcoat on the liquid crystal paint.

### 6.1 Results for Stationary Tests

The video records of liquid crystal isotherms for the leading and trailing surfaces of the model for the middle flowrate are presented in Figures 6-1 and 6-2, respectively. The contours noted were drawn from processed frames of video data like that shown in Figure 3-11. The identification system uses the isotherms, 1 through 6, and the video times, 1 through 4, for test 8.1 (Figure 6-1).

Nomographs were constructed from surface thermocouple data, obtained concurrently, to aid in the interpolation of each set of liquid crystal data (Figure 6-3). The heat transfer coefficients, determined for each thermocouple, are plotted as a function of local wall temperature for selected times into the test. The heat transfer coefficients at selected times after the start of the test (Times 1, 2, 3, and 4) for wall temperatures (Isotherms 1 through 6) are determined by intersecting a vertical wall temperature isotherm line with a selected test time shown as dashed lines in the nomograph figures. Heat transfer coefficients greater and less than the range of data are obtained by extrapolation.

Isotherms

- 1 - 46.7 °C (116 °F)
- 2 - 43.3 °C (110 °F)
- 3 - 37.8 °C (100 °F)
- 4 - 32.2 °C ( 90 °F)
- 5 - 26.7 °C ( 80 °F)
- 6 - 21.1 °C ( 70 °F)

Video Times

- 1 - 5.8 sec
- 2 - 9.2 sec
- 3 - 17.4 sec
- 4 - 33.3 sec

ID System

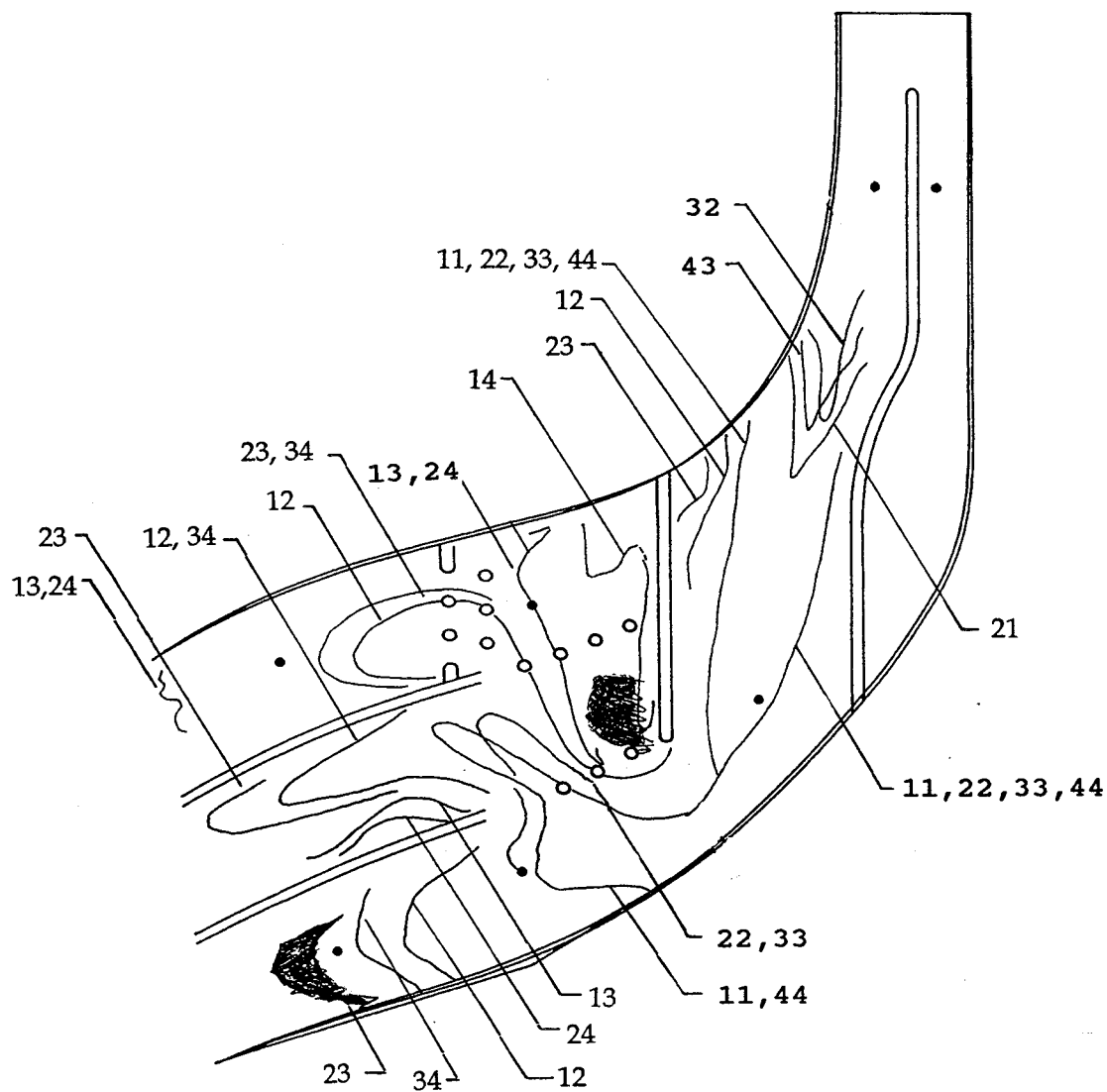
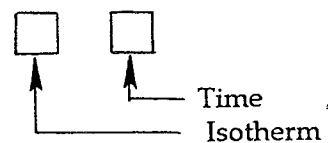


Figure 6-1. Video Records of Liquid Crystal Isotherms for Test 8.1.

Isotherms

- 1 - 46.7 °C (116 °F)
- 2 - 43.3 °C (110 °F)
- 3 - 37.8 °C (100 °F)
- 4 - 32.2 °C ( 90 °F)
- 5 - 26.7 °C ( 80 °F)
- 6 - 21.1 °C ( 70 °F)

Video Times

- 1 - 4.7 sec
- 2 - 7.8 sec
- 3 - 15.4 sec
- 4 - 29.4 sec

ID System

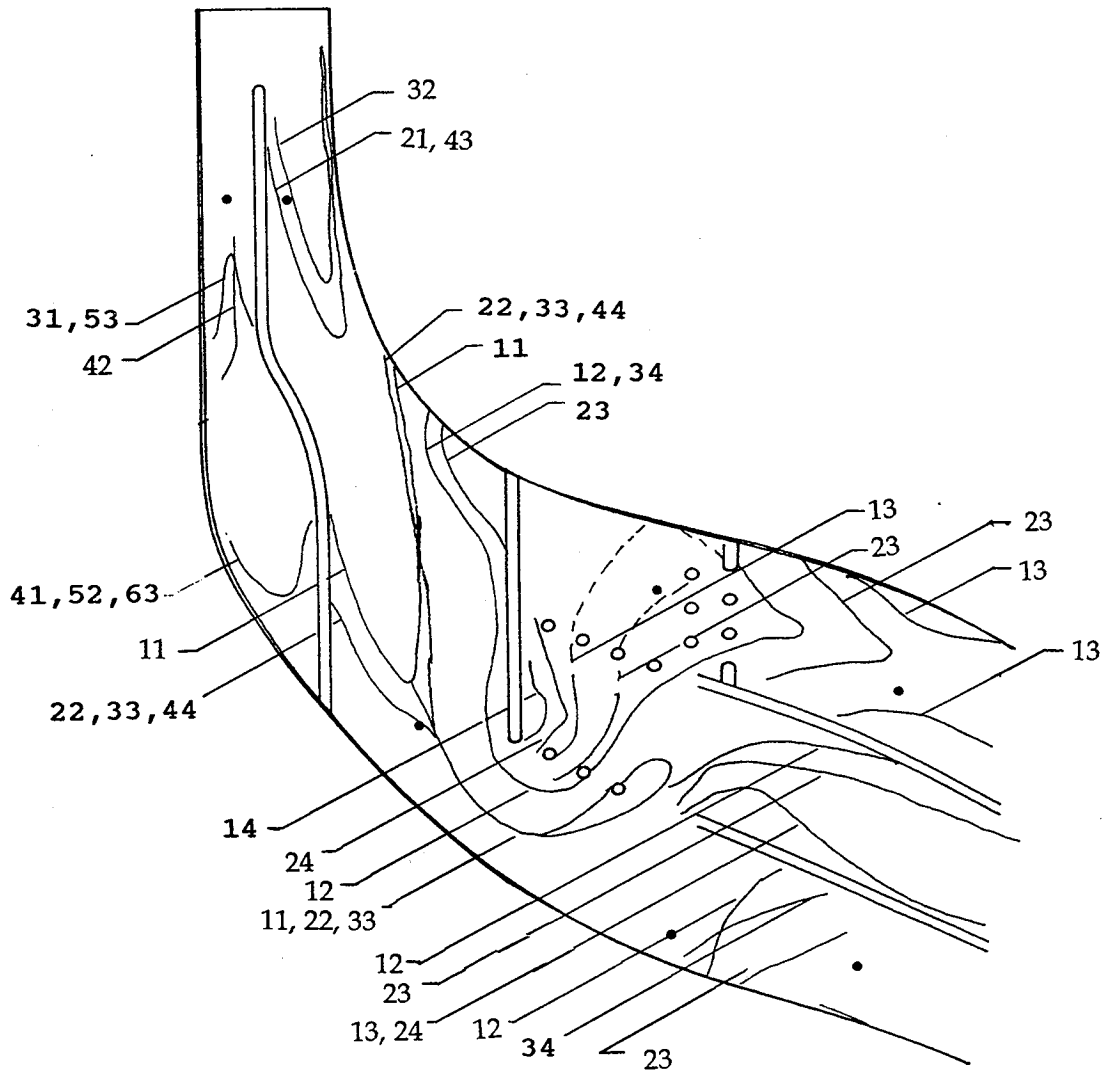
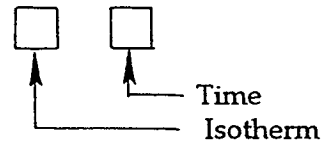
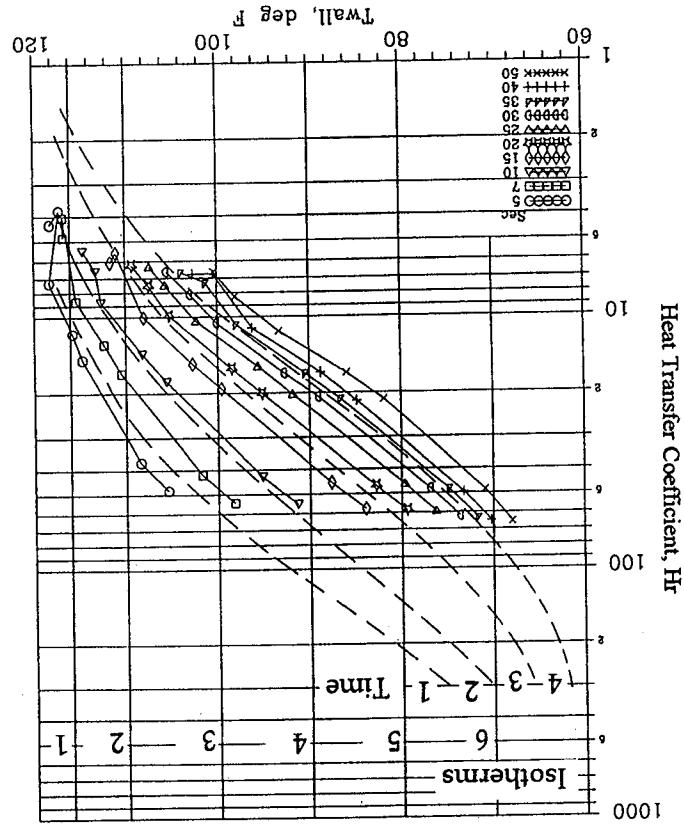
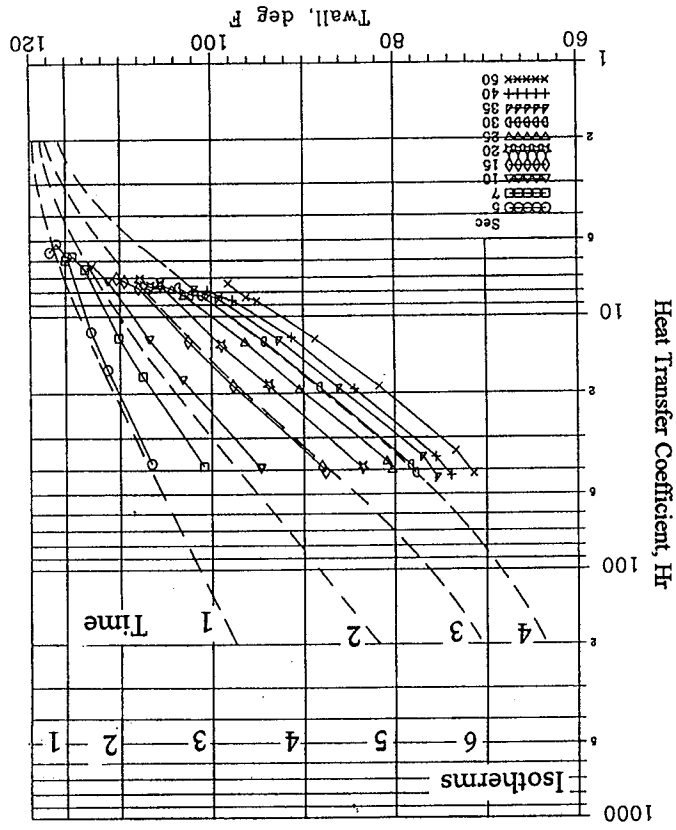


Figure 6-2. Video Records of Liquid Crystal Isotherms for Test 6.2.



a) Leading Surface  
Test 8.1  
 $T_{in}(\text{start}) = 48.8^\circ\text{C} (120^\circ\text{F})$   
 $T_{in}(\text{end}) = 13.3^\circ\text{C} (56^\circ\text{F})$   
Data from Figs. 5-1 & 5-2

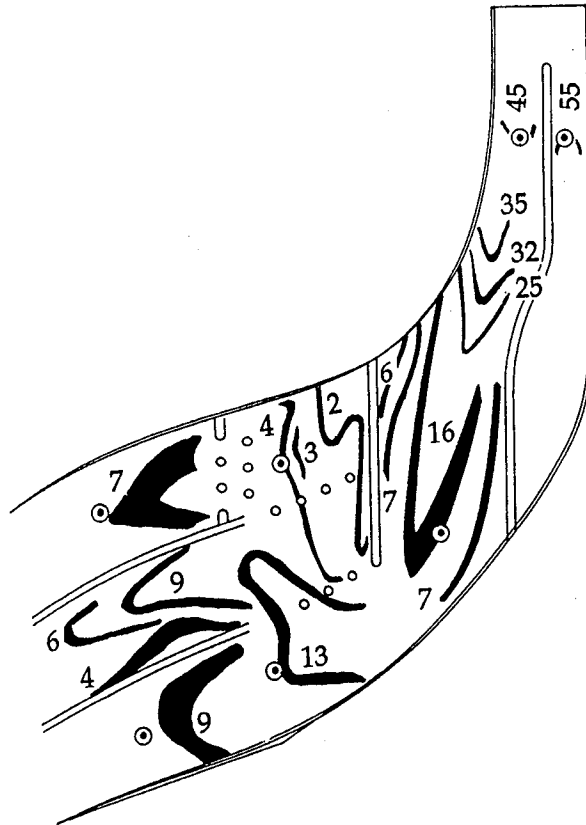


b) Trailing Surface  
Test 6.2  
 $T_{in}(\text{start}) = 48.8^\circ\text{C} (120^\circ\text{F})$   
 $T_{in}(\text{end}) = 13.3^\circ\text{C} (56^\circ\text{F})$   
Data from Figs. 5-3 & 5-4

Figure 6-3. Nomograph for Evaluating Liquid Crystal Data for  $Re = 13,000$  and  $\Omega = 0$  rpm.

Note: Dotted iso-coefficients  
from TC data

a) Leading Surface  
Test 8.1



b) Trailing Surface  
Test 6.2

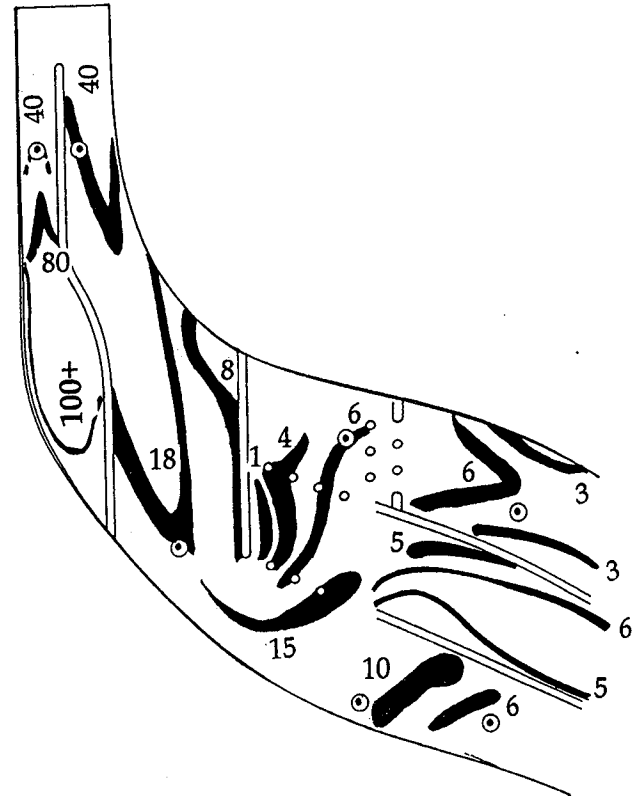


Figure 6-4. Heat Transfer Coefficients From Liquid Crystal Isotherms for  $Re = 13,000$  and  $\Omega = 0$  rpm.



The iso-heat-transfer coefficients at the intersections of the times and wall temperatures are plotted on Figure 6-4. In Regions 1 and 2, the heat transfer coefficient contour shapes and levels on the leading and trailing surfaces are similar. Variations in the results between the leading and trailing surfaces ( $\pm 15$  percent at the same location in the coolant passage) are indicative of the precision with which the heat flux and heat transfer coefficients can be determined using the liquid crystal and transient heat transfer measurement system. The heat transfer on the leading and trailing surface in Region 4 are also approximately the same on both sides of the channel, although the shapes of the contours in the middle and root passages have significantly different shapes. The leading surface heat transfer contour shapes indicate centerflowing coolant in the middle and root passages while the trailing surface contours suggest the coolant flow is biased to the side of the passage. These differences are attributed to the curvature in the coolant passage as the gas paths changes from radial (Region 1) to axial (Region 4).

## 6.2 Results from Rotating Tests

The apparent calibration of the liquid crystal paint changed appreciably due to rotation. Consequently, an effort was made to evaluate isotherms which were adjacent to or passed over the surface thermocouples. The isotherms selected are shown in Figures 6-5 and 6-6 for tests at 450 RPM and in Figures 6-9 and 6-10 for tests at 750 RPM. Nomographs were constructed for the four data sets required for the leading and trailing surfaces at 450 and 750 RPM (Figures 6-7 and 6-11). However, comparison of the liquid crystal contours with thermocouple data indicated that the liquid crystal paint calibration had shifted as much as  $7.8^{\circ}\text{C}$  ( $14^{\circ}\text{F}$ ) (e.g., in one instance the  $46.6^{\circ}\text{C}$  ( $116^{\circ}\text{F}$ ) liquid crystal paint calibration had shifted to  $38.9^{\circ}\text{C}$  ( $102^{\circ}\text{F}$ )). Consequently, the contours passing through the surface thermocouple locations were used to characterize the heat transfer. Analysis of the liquid crystal and thermocouple results suggested a constant shift in the paint calibrations was appropriate to compensate for the effects of rotation. Therefore, a shift of  $6^{\circ}\text{C}$  ( $10^{\circ}\text{F}$ ) was applied to the liquid crystal paint calibrations for tests with rotation (Figures 6-7 and 6-11) to help in the interpretation of the nomographs.

Iso-heat-transfer coefficient results for the medium flowrate at 450 and 750 RPM are presented in Figures 6-8 and 6-12, respectively. As noted in the discussions of the thermocouple results, the largest effects of rotation occurred on the leading surface in the tip section of Region 3 where the heat transfer decreased by a factor of approximately 5 at the thermocouple location. The large decrease in heat transfer is the result of a rotation induced flow redistribution in the exiting, Region 4, passages. Comparing the contours of heat transfer coefficient with rotation (Figures 6-8 and 6-12) with those from the stationary test (Figure 6-4) the flow structure is significantly different on the leading surface. The flow structure in the outward passage of Region 4 is centerflowing when stationary and skewed when rotating as a result of the blockage in the Region 3 tip section.

Isotherms

- 1 - 46.7 °C (116 °F)
- 2 - 43.3 °C (110 °F)
- 3 - 37.8 °C (100 °F)
- 4 - 32.2 °C ( 90 °F)
- 5 - 26.7 °C ( 80 °F)
- 6 - 21.1 °C ( 70 °F)

Video Times

- 1 - 18.9 sec
- 2 - 30.9 sec

ID System

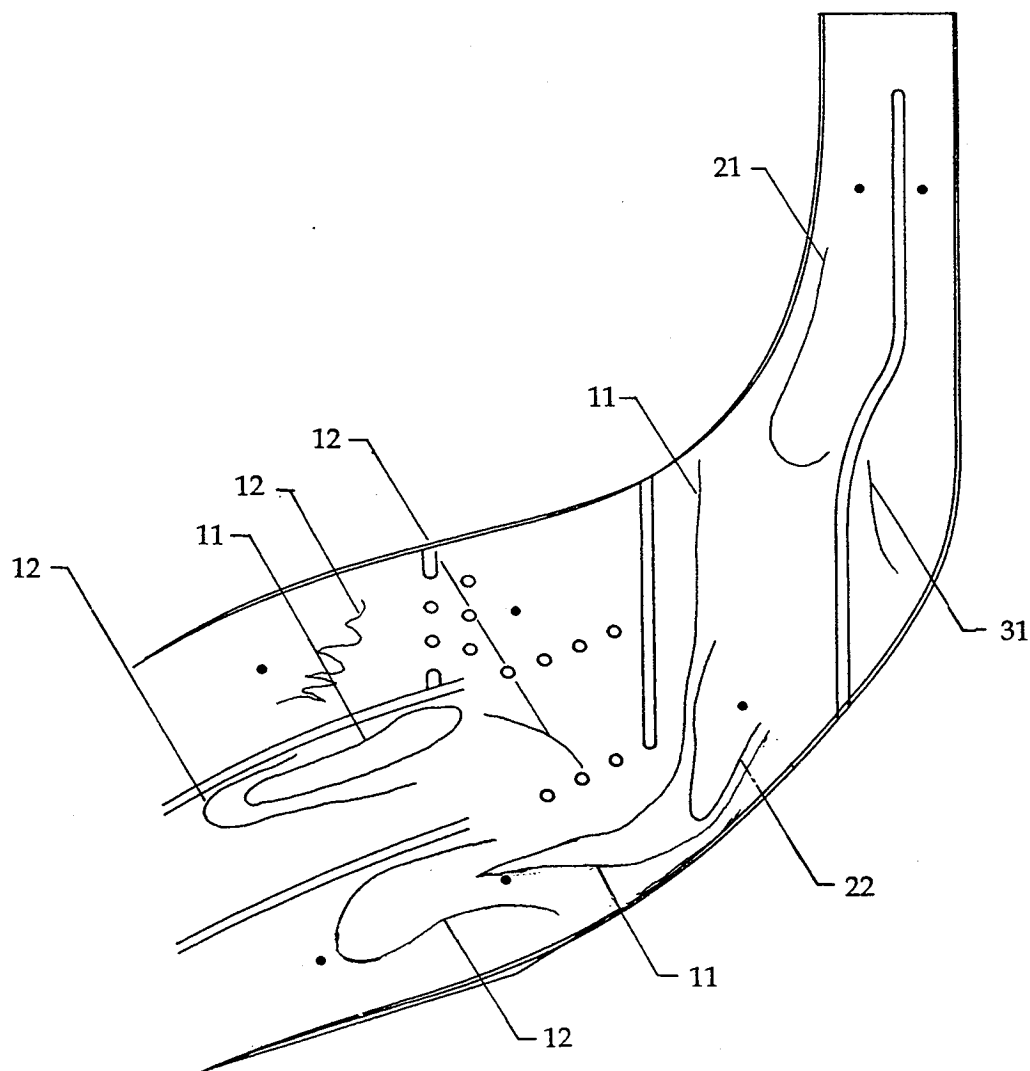
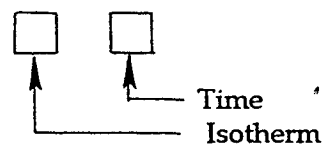


Figure 6-5. Video Records of Liquid Crystal Isotherms for Test 16.3.

Isotherms

- 1 - 46.7 °C (116 °F)
- 2 - 43.3 °C (110 °F)
- 3 - 37.8 °C (100 °F)
- 4 - 32.2 °C ( 90 °F)
- 5 - 26.7 °C ( 80 °F)
- 6 - 21.1 °C ( 70 °F)

Video Times

- 1 - 17.0 sec
- 2 - 26.0 sec
- 3 - 49.7 sec

ID System

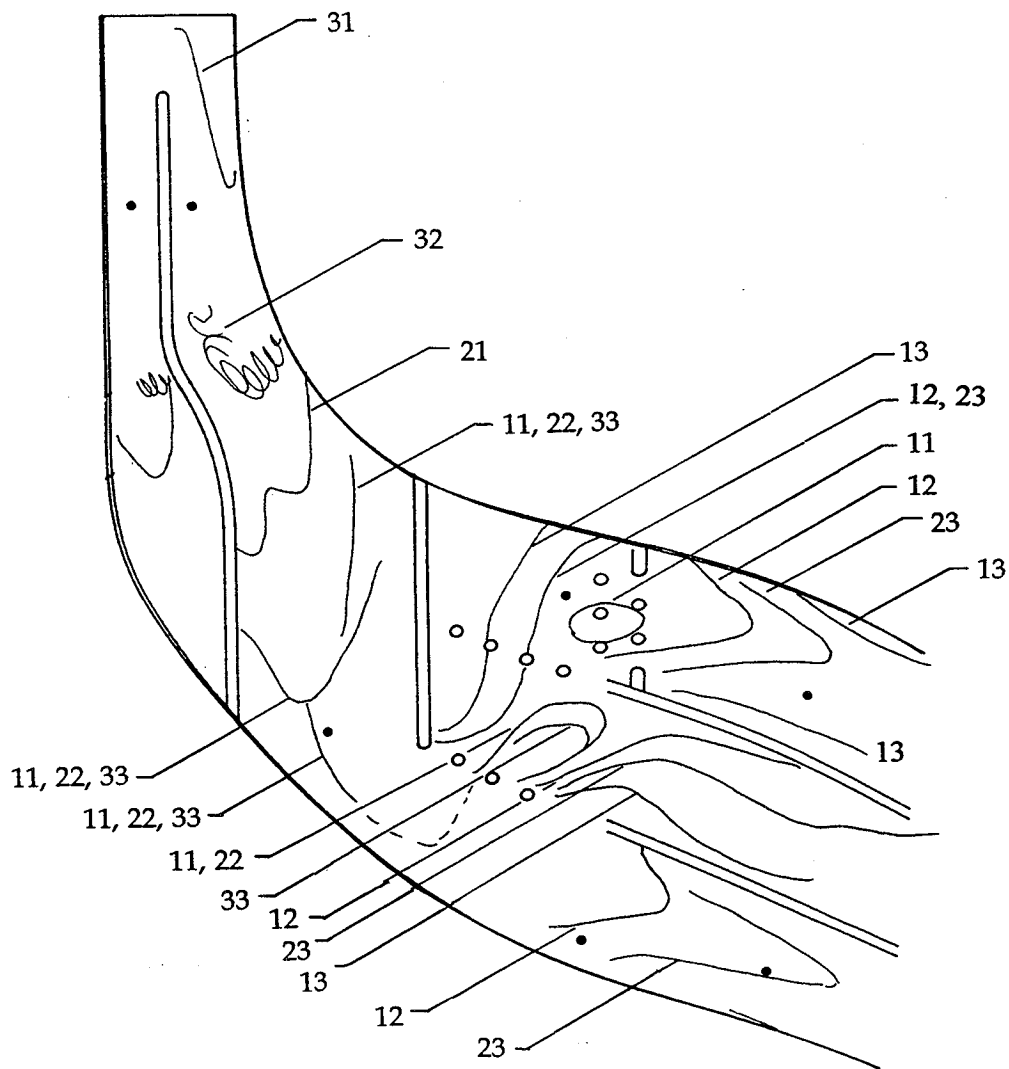
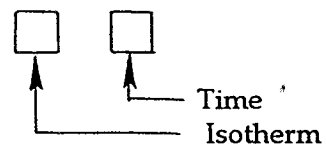


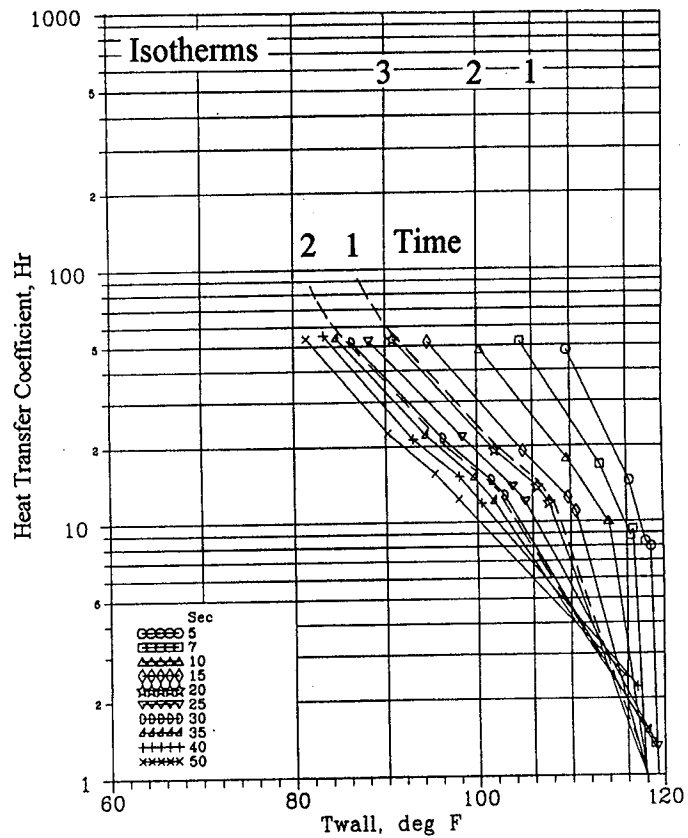
Figure 6-6. Video Records of Liquid Crystal Isotherms for Test 10.2.

## a) Leading Surface

Test 16.3

 $T_{in} \text{ (start)} = 51.7^\circ\text{C} \text{ (} 125^\circ\text{F)}$  $T_{in} \text{ (end)} = 23.9^\circ\text{C} \text{ (} 75^\circ\text{F)}$ 

Data from Figs. 5-5 &amp; 5-6

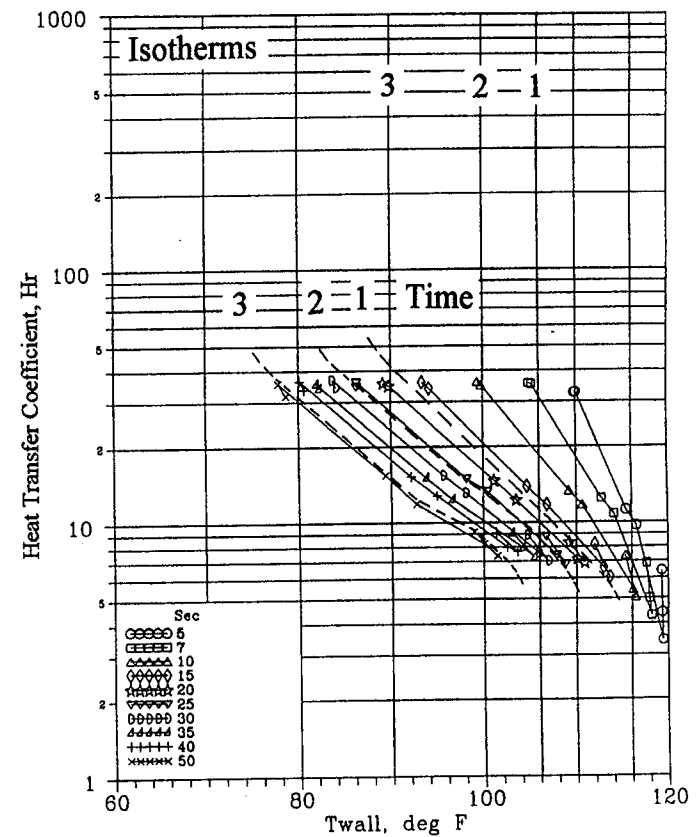


## b) Trailing Surface

Test 10.2

 $T_{in} \text{ (start)} = 52.8^\circ\text{C} \text{ (} 127^\circ\text{F)}$  $T_{in} \text{ (end)} = 18.3^\circ\text{C} \text{ (} 65^\circ\text{F)}$ 

Data from Figs. 5-7 &amp; 5-8

Figure 6-7. Nomograph for Evaluating Liquid Crystal Data for  $Re = 13,000$  and  $\Omega = 450$  rpm.

Notes: Dotted iso-coefficients from TC data.  
 Iso-coefficients interpolated between values at TC locations  
 due to liquid crystal calibration shift with rotation.

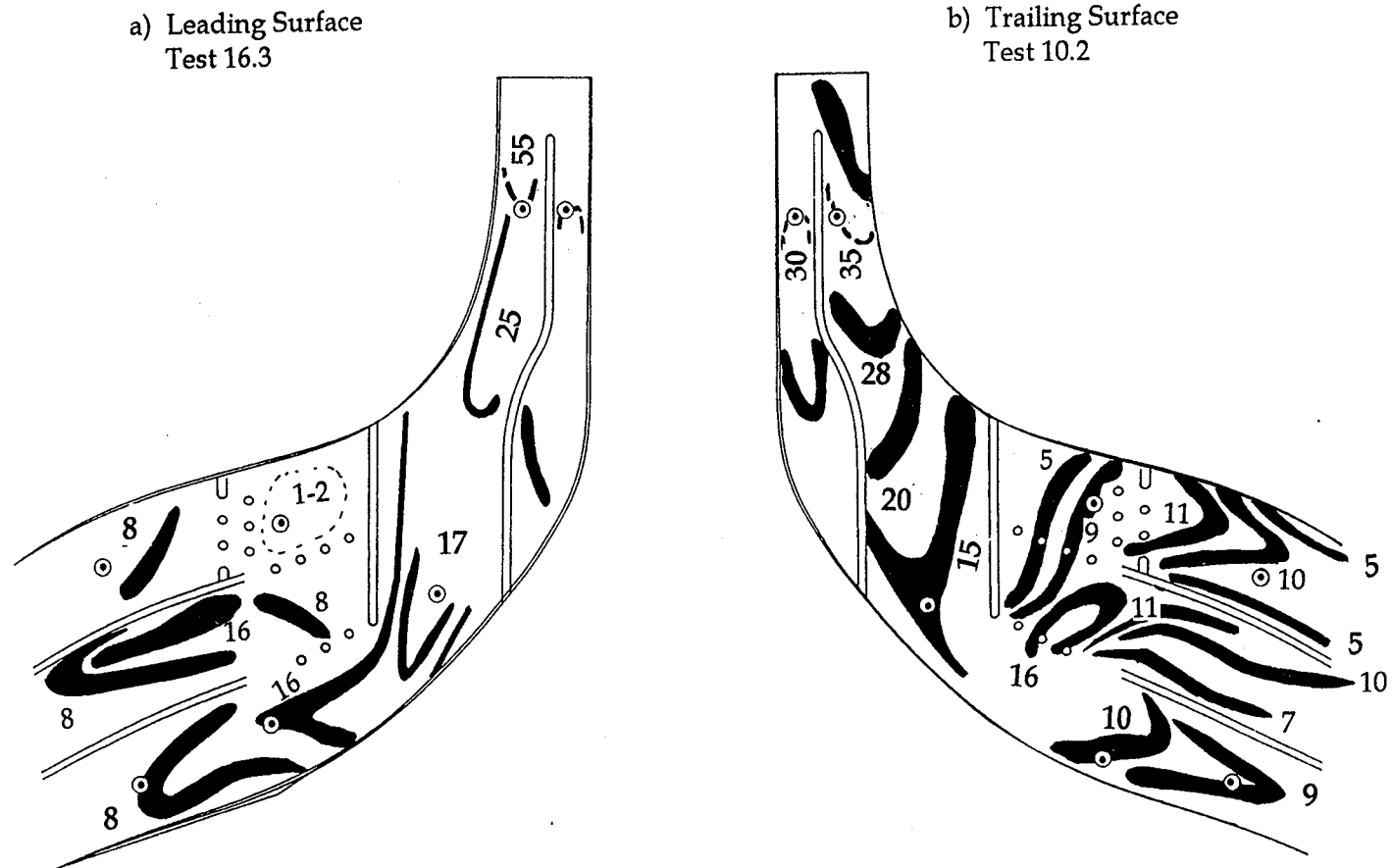


Figure 6-8. Heat Transfer Coefficients From Liquid Crystal Isotherms for  $Re = 13,000$  and  $\Omega = 450$  rpm.

Isotherms

- 1 - 46.7 °C (116 °F)
- 2 - 43.3 °C (110 °F)
- 3 - 37.8 °C (100 °F)
- 4 - 32.2 °C ( 90 °F)
- 5 - 26.7 °C ( 80 °F)
- 6 - 21.1 °C ( 70 °F)

Video Times

- 1 - 15.6 sec
- 2 - 23.8 sec
- 3 - 43.9 sec
- 4 - 58.0 sec

ID System

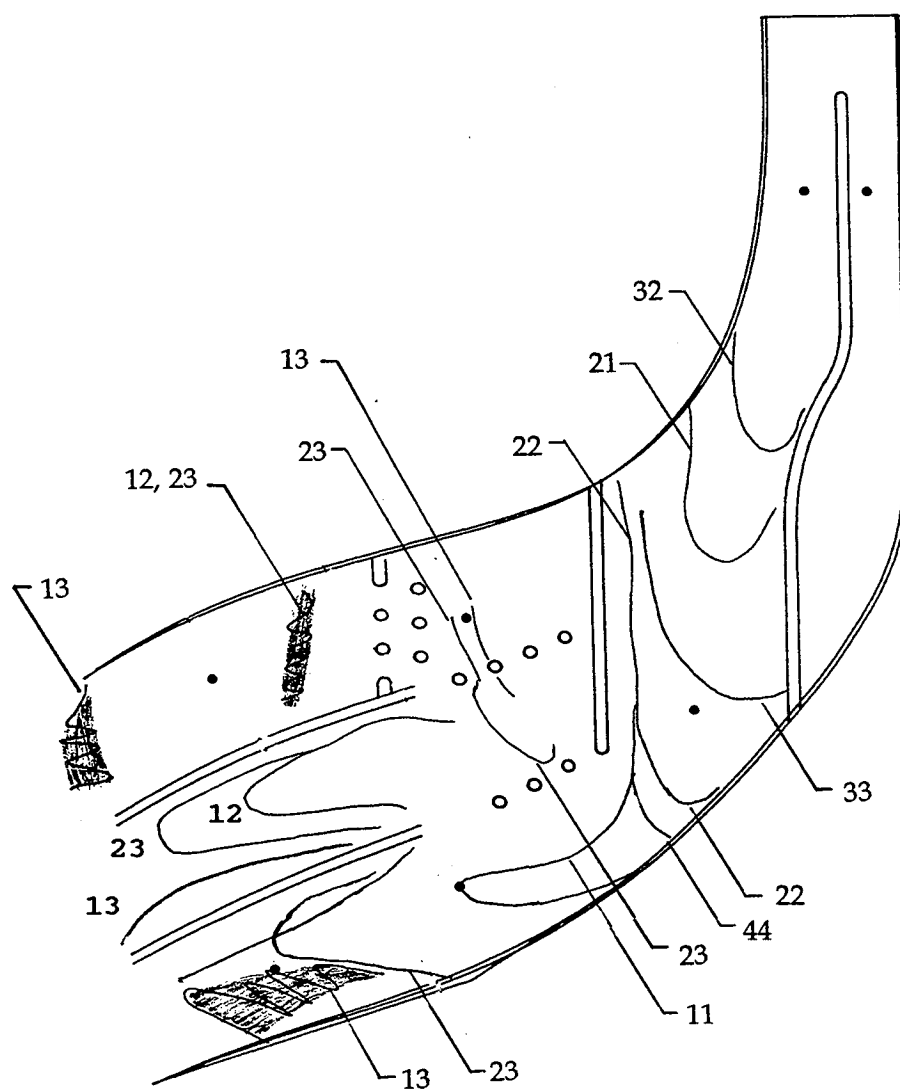
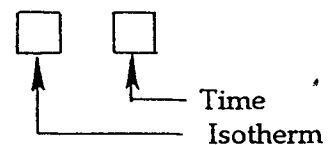


Figure 6-9. Video Records of Liquid Crystal Isotherms for Test 16.4.

### Isotherms

- 1 - 46.7 °C (116 °F)
- 2 - 43.3 °C (110 °F)
- 3 - 37.8 °C (100 °F)
- 4 - 32.2 °C ( 90 °F)
- 5 - 26.7 °C ( 80 °F)
- 6 - 21.1 °C ( 70 °F)

### Video Times

- 1 - 19.4 sec
- 2 - 32.9 sec
- 3 - 99.0 sec

### ID System

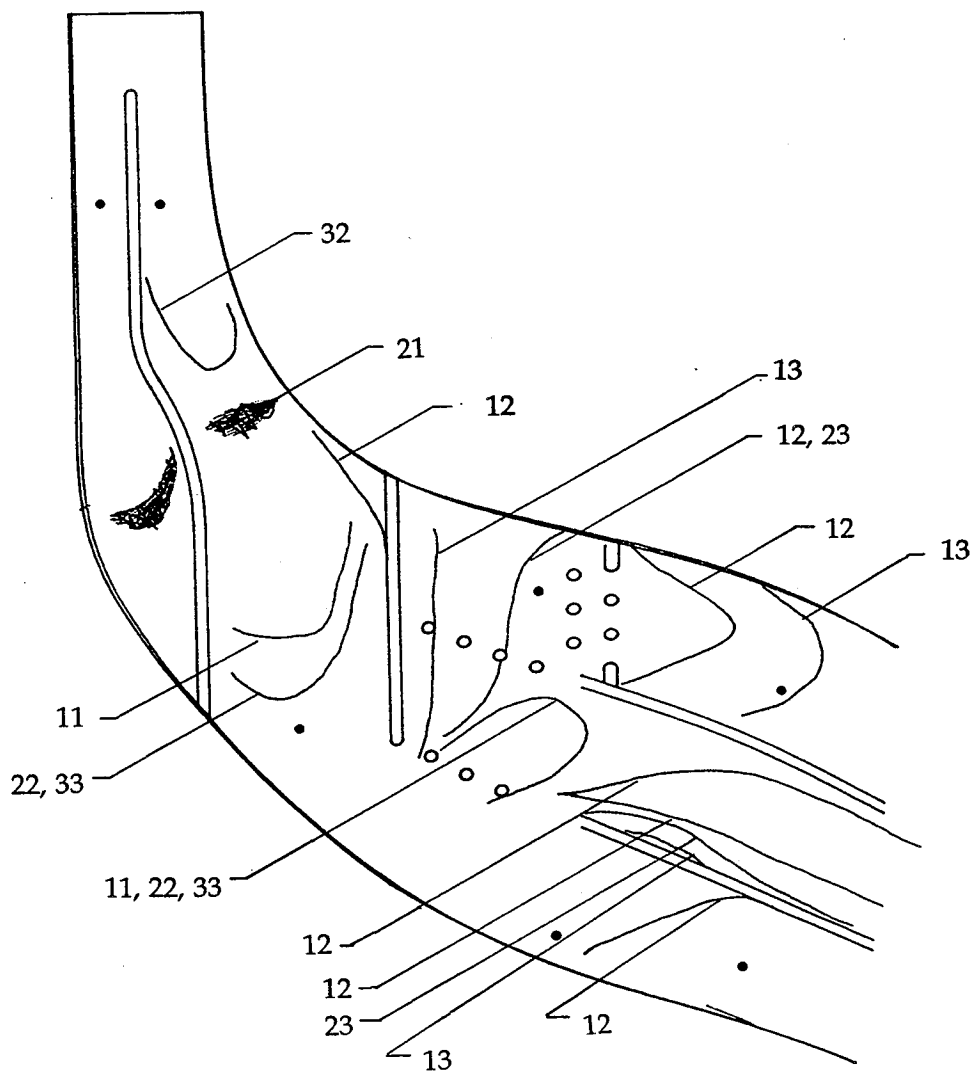
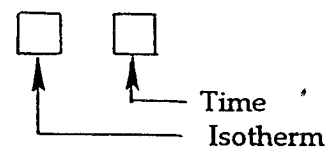


Figure 6-10. Video Records of Liquid Crystal Isotherms for Test 12.2.

a) Leading Surface

Test 16.4

$T_{in} \text{ (start)} = 51.1^\circ\text{C} (124^\circ\text{F})$

$T_{in} \text{ (end)} = 22.8^\circ\text{C} (73^\circ\text{F})$

Data from Figs. 5-9 & 5-10

b) Trailing Surface

Test 12.2

$T_{in} \text{ (start)} = 51.1^\circ\text{C} (124^\circ\text{F})$

$T_{in} \text{ (end)} = 25.0^\circ\text{C} (77^\circ\text{F})$

Data from Figs. 5-11 & 5-12

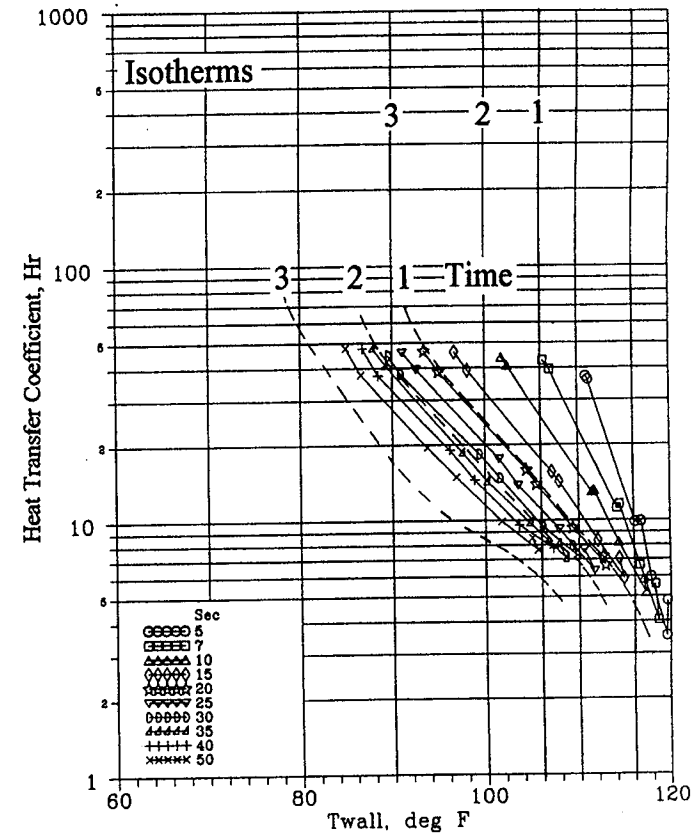
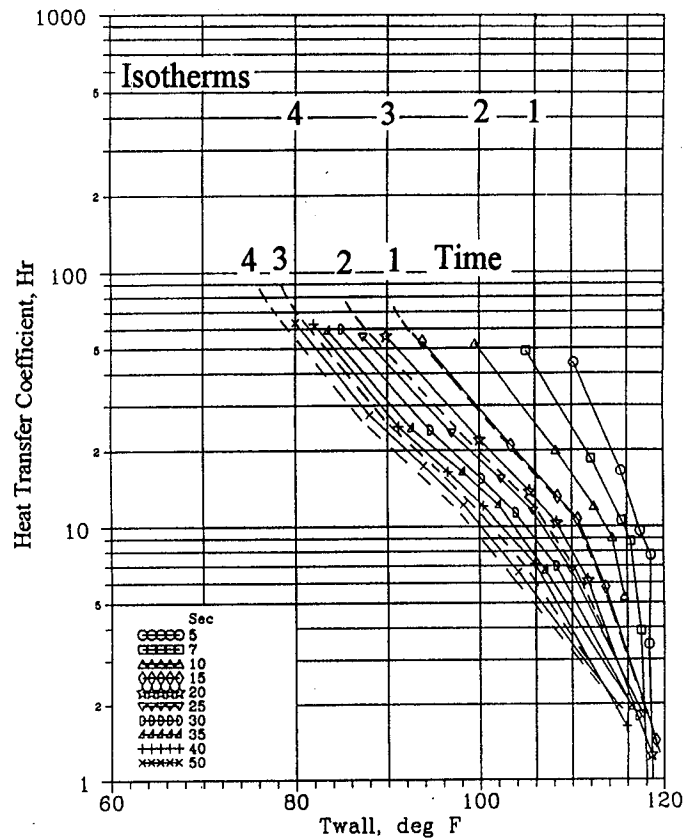


Figure 6-11. Nomograph for Evaluating Liquid Crystal Data for  $Re = 13,000$  and  $\Omega = 750$  rpm.



Notes: Dotted iso-coefficients from TC data.  
 Iso-coefficients interpolated between values at TC locations  
 due to liquid crystal calibration shift with rotation.

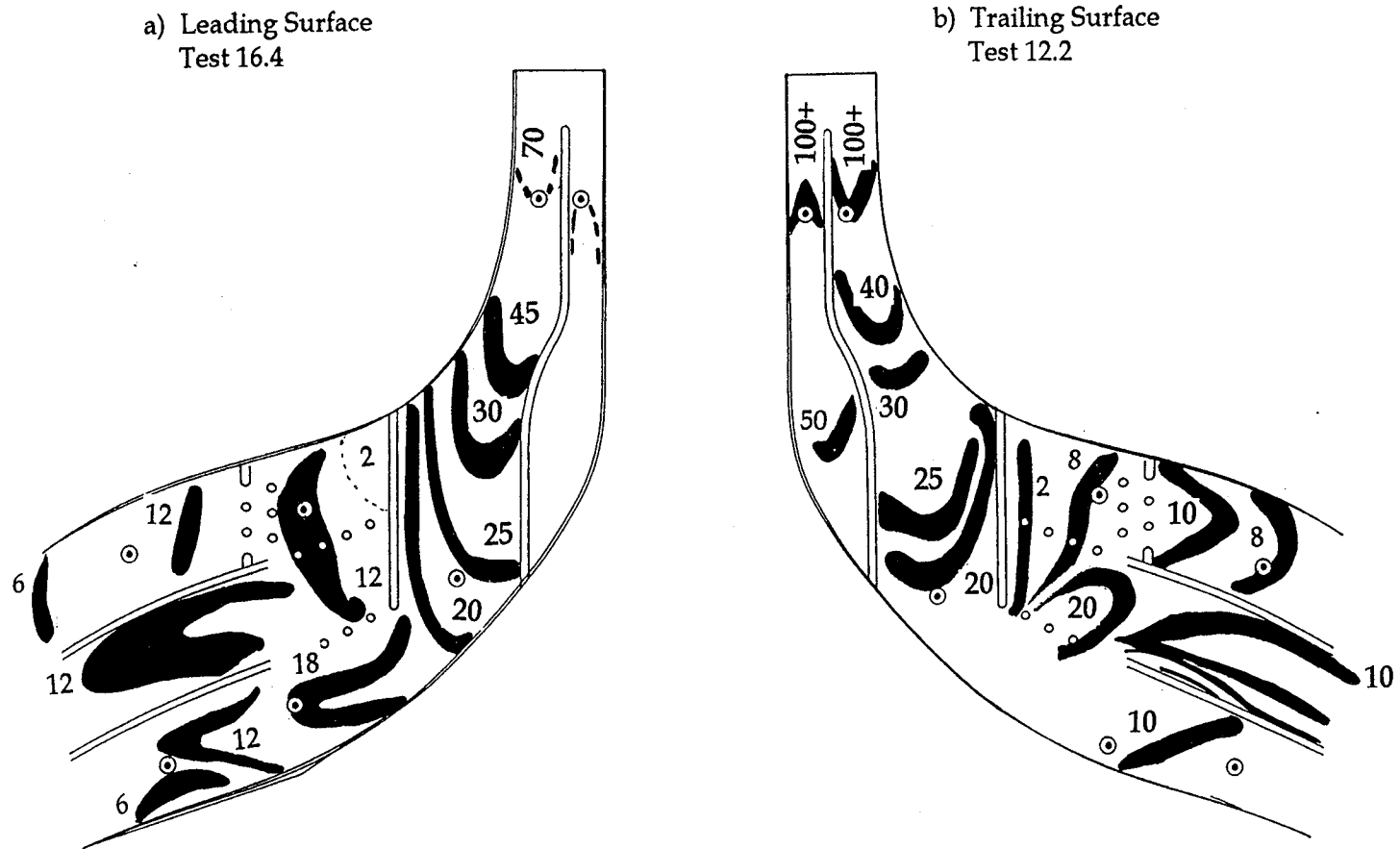


Figure 6-12. Heat Transfer Coefficients From Liquid Crystal Isotherms for  $Re = 13,000$  and  $\Omega = 750$  rpm.

## 7.0 COMPARISON WITH PREVIOUS ANALYSIS

Only general heat transfer characteristics can be compared due to the differences in operating conditions and the lack of velocity and pressure data within the model. The largest noticeable difference in the flow fields and heat transfer between the four sets of calculations, Ippolito, 1991, Dawes, 1992, Steinhilber et al., 1991, and Stephens et al., 1993, occurs in Region 2 where the flow is radially inward. The results of Ippolito, 1991, and Steinhilber 1991, show higher velocities along the outer or tip section of Region 2 and along the divider between Region 2 and Region 3. The results of Dawes, 1992, and Stephens, et al., 1993, show higher velocities in the center of the Region 2 passage. High heat transfer accompanied the higher velocities in the preceding calculations. The results from both the rotating and stationary heat transfer experiments show the highest heat flux in the center of the channel with the characteristic predicted by Dawes, 1992, and Stephens et al., 1993. More recent work by Steinhilber, 1993, with a finer grid also produced (unpublished) results with the flow tending toward the center of the Region 2 passage.

A second region in which general characteristics can be compared is the tip section of Region 3. All the analyses showed low velocities and low heat transfers in this region. However, from the numerical results presented, it does not appear that a significant difference was predicted by any of the analyses in the heat transfer between the leading and trailing surface.

The heat transfer contours predicted by Ippolito, 1991, in the root section of Region 3 also resemble the contours measured and have larger heat transfer coefficients on the leading surface than the trailing surface. Recall that the experimental results from the leading and trailing surfaces of the root section, Region 3, indicated increased levels of heat transfer with rotation for certain rotation numbers.

The shapes of the Region 4 heat transfer contours predicted by Ippolito, 1991, in the root, middle, and tip passages resemble the contours measured.

Several of the heat transfer characteristics measured in the 1.15 scale model of the NASA LeRC High Temperature Radial Turbine appear to be predicted by one or more of the numerical studies. However, a more complete evaluation of the numerical procedures by direct comparison with the present experiments requires that calculations be made using the boundary conditions of the experiment, including possibly the conjugate heat transfer condition of the transient heat transfer experiment.

## 8.0 REFERENCES

Anon, 1989, "Rotor Assy-Air-Cooled Radial Turbine: Drawing Ex159092", Allison Gas Turbine Division, July 12, 1989.

Blair, M.F., Wagner, J.H., and Steuber, G.D., 1991, "New Applications of Liquid Crystal Thermography in Rotating Turbomachinery Heat Transfer Research", ASME Preprint 91-GT-354.

Calvert, G.S., Beck, S.C., and Okapuu, E., 1971, "Design and Experimental Evaluation of a High-Temperature Radial Turbine", USAAMRDL TR 71-20.

Clifford, R.J., Jones, T.V., and Dunne, S.T., 1983, "Techniques for Obtaining Detailed Heat Transfer Coefficient Measurements Within Gas Turbine Blade and Vane Cooling Passages," ASME Paper 83-GT-58.

Clifford, R.J., 1985, "Rotating Heat Transfer Investigations on a Multipass Cooling Geometry", AGARD Conference Proceedings, No. 390: Heat Transfer and Cooling in Gas Turbines.

Dawes, W.N., 1992, "The Solution-Adaptive Numerical Simulation of the 3D Viscous Flow in the Serpentine Coolant Passage of a Radial Inflow Turbine Blade", ASME Paper 92-GT-193.

Eckert, E.R.G., Diaguila, A.J. and Curren, A.N., 1953, "Experiments on Mixed - Free and Forced-Convective Heat Transfer Connected with Turbulent Flow Through a Short Tube", NACA Technical Note 2974.

El-Husayini, H.A., Taslim, M.E. and Kercher, D.M., 1992, "Experimental Heat Transfer Investigation of Stationary and Orthogonally Rotating Asymmetric and Symmetric Heated Smooth and Turbulated Channels", ASME Paper 92-HT-189.

Guidez, J., 1989, "Study of the Convective Heat Transfer in Rotating Coolant Channel", ASME Turbomachinery, Vol 111, pp. 43-50.

Hajek, T.J., Wagner, J.H., Johnson, B.V., Higgins, A.W., and Steuber, G.D., 1991, "Effects of Rotation on Coolant Passage Heat Transfer: Volume 1 - Coolant Passages with Smooth Walls", NASA Contractors Report 4396.

Hammer, A.N., Aigret, G.G., Psychogios, T.P., and Rodger, C., 1986, "Fabrication of Cooled Radial Turbine Rotor", (SR 86-R-4938, Solar Turbines, Inc.,) NASA CR-179503.

Han, J.C., Zhang, Y.M., and Lee, C.P., 1992, "Influence of Surface Heating Condition on Local Heat Transfer in a Rotating Square Channel with Smooth Walls and Radial Flow Outward," ASME Paper 92-GT-188.

Han, J.C., Park, J.S. and Ibrahim, M.Y., 1986, "Measurement of Heat Transfer and Pressure Drop in Rectangular Channels with Turbulence Promoters", NASA Contractors Report 4015.

Ippolito, J., 1991, "Three Dimensional Flow Analysis of the Internal Passage of a Cooled Radial Rotor", Analysis and Design Application Company, LTD., Report Number 30-02-004, April 26, 1991.

Johnson, B.V., Wagner, J.H., Steuber, G.D. and Yeh, F.C., 1992, "Heat Transfer in Rotating Serpentine Passages with Trips Skewed to the Flow", ASME Paper 92-GT-191.

Johnson, B.V., Wagner, J.H., and Steuber, G.D., 1993, "Effect of Rotation on Coolant Passage Heat Transfer: Volume II - Coolant Passages with Trips Normal and Skew to the Flow", NASA Contractors Report 4396.

Johnston, J.P., Halleen, R.M., and Lezius, D.K., 1972, "Effects of Spanwise Rotation of the Structure of Two-Dimensional Fully Developed Turbulent Channel Flow", J. Fluid Mech., Vol 56, Part 3, pp 533-557.

Kreith, F., 1973, "Principles of Heat Transfer" 3rd Edition, Intex Press, Inc., pp 177.

Kumar, G.N. and Deanna, R.G., 1998, "Development of a Thermal and Structural Analysis Procedure for Cooled Radial Turbines", ASME Paper 88-GT-18.

Kumar, G.N, and Deanna, R.G. , 1989, "A Generalized One Dimensional Computer Code for Turbomachinery Cooling Passage Flow Calculations", NASA Technical Memorandum 102079.

Metzger, D.E. and Larson D.E., 1986, "Use of Melting Point Surface Coatings for Local Convective Heat Transfer Measurements in Rectangular Channel Flows with 90-deg Turns", ASME J. Heat Transfer, Vol 108, pp 48.

Metzger, D.E., Bunker, R.S., and Bosch, G., 1989, "Transient Liquid Crystal Measurement of Local Heat Transfer on a Rotating Disk with Jet Impingement", ASME Paper 89-GT-287.

Mochizuki, S., Takamura, J., Yamawaki, S., and Yang, W.J., 1992, "Heat Transfer in Serpentine Flow Passages with Rotation", ASME Paper 92-GT-190

Morris, W.D., 1981, Heat Transfer and Fluid Flow in Rotating Coolant Channels, Research Studies Press.

Roelke, R.J., 1991, Coordinates for Coolant Passage Core of NASA LeRC High-Temperature Cooled Radial Turbine, Private Communication.

Saabas, J., Arora, S.C., and Abdel Messeh, W., 1987, "Application of the Transient Test Technique to Measure Local Heat Transfer Coefficients Associated with Augmented Airfoil Cooling Passages", ASME Paper 87-GT-212.

Schultz, D.L., Jones, T.V., Oldfield, M.L.G., and Daniels, L.C., 1973, "Heat Transfer Measurements in Short-Duration Hypersonic Facilities", Agardograph 165.

Snyder, P.H., 1992, "Cooled High-Temperature Radial Turbine Program", NASA CR 189122, USAACSCOM TR-92-C-010, Allison Report No. EDR 15982, May 1992.

Snyder, P.H. and Roelke, R.J., 1988, "The Design of an Air-Cooled Metallic High Temperature Radial Turbine," Conference Preprint AIAA-88-2872.

Steinhorsson, E., Shih TI-P and Roelke R.J., 1991, "Computation of the Three-Dimensional Flow and Heat Transfer Within a Coolant Passage of a Radial Flow Turbine", Conference Preprint AIAA-91-2238. 1991.

Steinhorsson, E., Liou, M.S., and Povinelli, L.A., 1993, "Development of an Explicit Multiblock/Multigrid Flow Solver for Viscous Flows in Complex Geometries", Conference Preprint AIAA-93-2380.

Steinhorsson, E., 1993, "Private Communication", July.

Stephens, M.A., Rimlinger, M.J., and Shih T.I-P, 1993, "Chimera Grids in the Simulation of Three-Dimensional Flowfields in Turbine-Blade-Coolant Passages", Conference Preprint AIAA-93-2559.

Vershure, R.W., Large, G.D., Meyer, L.J., and Lane, J.M., 1980, "A Cooler Laminated Radial Turbine Technology Demonstration", AIAA Paper 80-0300.

Wagner, J.H., Johnson, B.V., and Hajek, T.J., 1991, "Heat Transfer in Rotating Passages with Smooth Walls and Radial Outward Flow", ASME Turbomachinery, Vol. 113 pp 42-51, January (ASME Paper 89-GT-272).



## **9.0 APPENDIX**



## 9.1 Nomenclature

$d$	Hydraulic diameter, $2HW/(H+W)$
$H$	Leading to trailing surface separation difference
$Hr$	Heat transfer coefficient, $\text{Btu/Ft}^2/\text{hr}/^\circ\text{F}$
$k$	Thermal conductivity
$Q_w$	Heat flux, $\text{Btu/Ft}^2/\text{hr}$
$R$	Radial position
$Re$	Reynolds number
$Ro$	Rotation number
$t$	Time
$T$	Temperature
$V$	Coolant velocity
$W$	Width of coolant passage
$x$	Distance into model wall
$\alpha$	Thermal diffusivity
$\mu$	Dynamic viscosity
$\omega$	Rotation rate $\text{rad/sec}$
$\rho$	Density

### Subscripts:

$b, c$	Bulk fluid property
$w, \text{wall}$	Fluid property at the wall
$d$	Parameter based on hydraulic diameter
$h$	Parameter based on separation distance

## **9.2 Tables of Flow Conditions for Full Scale NASA Radial Turbine and 1.15 Scale Model Coolant Passage**

### **Note:**

Model pressures noted are derived from an average of the measured pressures at the flowmeter locations upstream and downstream of the rotating facility. Temperatures were measured in the model coolant passage. For parametric analysis the wall temperature,  $T_w$ , was assumed to be the initial coolant temperature prior to the transient portion of a test and the coolant temperature,  $T_c$ , was assumed to be the inlet coolant temperature at 150 seconds. These two temperatures provided the ideal heat transfer potential used for comparisons of the test results.

## NASA Radial Turbine

## Full Scale

Location	A	B	C	
Flowrate	0.0154	0.0154	0.0154	#/sec
Radius	6.8	6.8	6.8	in
H	0.110	0.110	0.170	in
W	0.246	0.826	1.983	in
Pc	24.5	18.0	12.0	psia
Tc	600	650	700	deg R
Tw	750	750	750	deg R
ROh	0.028	0.064	0.226	
REd	72949	27086	11506	
BUOY	0.0096	0.0333	0.1356	
Density	0.110	0.075	0.046	#/ft <sup>3</sup>
Velocity	742.6	326.2	142.1	ft/sec
RPM	21596	21596	21596	
Omega	2261.5	2261.5	2261.5	rad/sec
d	0.152	0.194	0.313	in
area	0.000188	0.000631	0.002341	in <sup>2</sup>
visc(mu)	1.42E-05	1.46E-05	1.49E-05	lb/sec-ft
k	0.0180	0.0186	0.0191	BTU/ft-hr-F

1.15 Full Scale Model  
Median Coolant Flow Rate  
Stationary Model

Test # :	6.2 Date:			
Location	A	B	C	
Flowrate	0.0073	0.0073	0.0073	#/sec
Radius	19.0	19.0	16.5	in
H	0.127	0.127	0.196	in
W	0.283	0.950	2.280	in
Pc	164.2	164.2	164.2	psia
Tc	514.5	514.5	514.5	deg R
Tw	579.9	579.9	579.9	deg R
ROh	0.000	0.000	0.000	
REd	34676	13191	5736	
BUOY	0.0000	0.0000	0.0000	
Density	0.862	0.862	0.862	#/ft^3
Velocity	34.2	10.2	2.7	ft/sec
RPM	0	0	0	
Omega	0.0	0.0	0.0	rad/sec
d	0.175	0.223	0.360	in
area	0.000249	0.000835	0.003095	in^2
visc(mu)	1.24E-05	1.24E-05	1.24E-05	lb/sec-ft
k	0.0152	0.0152	0.0152	BTU/ft-hr-F
Test # :	8.1 Date:			
Location	A	B	C	
Flowrate	0.0073	0.0073	0.0073	#/sec
Radius	19.0	19.0	16.5	in
H	0.127	0.127	0.196	in
W	0.283	0.950	2.280	in
Pc	164.0	164.0	164.0	psia
Tc	514.9	514.9	514.9	deg R
Tw	580.7	580.7	580.7	deg R
ROh	0.000	0.000	0.000	
REd	34745	13217	5748	
BUOY	0.0000	0.0000	0.0000	
Density	0.861	0.861	0.861	#/ft^3
Velocity	34.3	10.2	2.8	ft/sec
RPM	0	0	0	
Omega	0	0	0	rad/sec
d	0.175	0.223	0.360	in
area	0.000249	0.000835	0.003095	in^2
visc(mu)	1.24E-05	1.24E-05	1.24E-05	lb/sec-ft
k	0.0152	0.0152	0.0152	BTU/ft-hr-F

1.15 Full Scale Model  
High Coolant Flow Rate  
Stationary Model

Test # :	5.2 Date:			
Location	A	B	C	
Flowrate	0.0151	0.0151	0.0151	#/sec
Radius	19.0	19.0	16.5	in
H	0.127	0.127	0.196	in
W	0.283	0.950	2.280	in
Pc	161.0	161.0	161.0	psia
Tc	503.3	503.3	503.3	deg R
Tw	580.7	580.7	580.7	deg R
ROh	0.000	0.000	0.000	
REd	72196	27463	11943	
BUOY	0.0000	0.0000	0.0000	
Density	0.864	0.864	0.864	#/ft^3
Velocity	70.5	21.0	5.7	ft/sec
RPM	0	0	0	
Omega	0.0	0.0	0.0	rad/sec
d	0.175	0.223	0.360	in
area	0.000249	0.000835	0.003095	in^2
visc(mu)	1.23E-05	1.23E-05	1.23E-05	lb/sec-ft
k	0.0151	0.0151	0.0151	BTU/ft-hr-F

Test # :	7.1 Date:			
Location	A	B	C	
Flowrate	0.0149	0.0149	0.0149	#/sec
Radius	19.0	19.0	16.5	in
H	0.127	0.127	0.196	in
W	0.283	0.950	2.280	in
Pc	160.2	160.2	160.2	psia
Tc	504.6	504.6	504.6	deg R
Tw	581.8	581.8	581.8	deg R
ROh	0.0000	0.0000	0.0000	
REd	71033	27021	11750	
BUOY	0.0000	0.0000	0.0000	
Density	0.858	0.858	0.858	#/ft^3
Velocity	69.98	20.85	5.62	ft/sec
RPM	0	0	0	
Omega	0.0	0.0	0.0	rad/sec
d	0.175	0.223	0.360	in
area	0.00025	0.00083	0.00310	in^2
visc(mu)	1.23E-05	1.23E-05	1.23E-05	lb/sec-ft
k	0.0151	0.0151	0.0151	BTU/ft-hr-F

1.15 Full Scale Model  
Low Coolant Flow Rate  
450 rpm

Test # :	16.5 Date:			
Location	A	B	C	
Flowrate	0.0038	0.0038	0.0038	#/sec
Radius	19.0	19.0	16.5	in
H	0.127	0.127	0.196	in
W	0.283	0.950	2.280	in
Pc	165.3	165.3	165.3	psia
Tc	536.8	536.8	536.8	deg R
Tw	579.2	579.2	579.2	deg R
ROh	0.027	0.091	0.524	
REd	17642	6711	2918	
BUOY	0.0082	0.0919	1.6965	
Density	0.832	0.832	0.832	#/ft <sup>3</sup>
Velocity	18.2	5.4	1.5	ft/sec
RPM	450	450	450	
Omega	47.1	47.1	47.1	rad/sec
d	0.175	0.223	0.360	in
area	0.000249	0.000835	0.003095	in <sup>2</sup>
visc(mu)	1.25E-05	1.25E-05	1.25E-05	lb/sec-ft
k	0.0155	0.0155	0.0155	BTU/ft-hr-F

1.15 Full Scale Model  
Median Coolant Flow Rate  
450 rpm

Test # :	10.2 Date:			
Location	A	B	C	
Flowrate	0.0073	0.0073	0.0073	#/sec
Radius	19.0	19.0	16.5	in
H	0.127	0.127	0.196	in
W	0.283	0.950	2.280	in
Pc	164.2	164.2	164.2	psia
Tc	518.9	518.9	518.9	deg R
Tw	581.9	581.9	581.9	deg R
ROh	0.014	0.048	0.277	
REd	34650	13181	5732	
BUOY	0.0034	0.0379	0.6991	
Density	0.855	0.855	0.855	#/ft^3
Velocity	34.6	10.3	2.8	ft/sec
RPM	450	450	450	
Omega	47.1	47.1	47.1	rad/sec
d	0.175	0.223	0.360	in
area	0.000249	0.000835	0.003095	in^2
visc(mu)	1.24E-05	1.24E-05	1.24E-05	lb/sec-ft
k	0.0153	0.0153	0.0153	BTU/ft-hr-F
Test # :	16.4 Date:			
Location	A	B	C	
Flowrate	0.0074	0.0074	0.0074	#/sec
Radius	19.0	19.0	16.5	in
H	0.127	0.127	0.196	in
W	0.283	0.950	2.280	in
Pc	164.4	164.4	164.4	psia
Tc	528.5	528.5	528.5	deg R
Tw	580.3	580.3	580.3	deg R
ROh	0.014	0.047	0.268	
REd	34971	13303	5785	
BUOY	0.0026	0.0293	0.5415	
Density	0.840	0.840	0.840	#/ft^3
Velocity	35.7	10.6	2.9	ft/sec
RPM	450	450	450	
Omega	47.1	47.1	47.1	rad/sec
d	0.175	0.223	0.360	in
area	0.000249	0.000835	0.003095	in^2
visc(mu)	1.25E-05	1.25E-05	1.25E-05	lb/sec-ft
k	0.0154	0.0154	0.0154	BTU/ft-hr-F

1.15 Full Scale Model  
High Coolant Flow Rate  
450 rpm

Test # :	10.1 Date:			
Location	A	B	C	
Flowrate	0.0150	0.0150	0.0150	#/sec
Radius	19.0	19.0	16.5	in
H	0.127	0.127	0.196	in
W	0.283	0.950	2.280	in
Pc	159.2	159.2	159.2	psia
Tc	511.2	511.2	511.2	deg R
Tw	579.3	579.3	579.3	deg R
ROh	0.007	0.023	0.134	
REd	71036	27022	11751	
BUOY	0.0009	0.0096	0.1772	
Density	0.841	0.841	0.841	#/ft^3
Velocity	71.5	21.3	5.7	ft/sec
RPM	450	450	450	
Omega	47.1	47.1	47.1	rad/sec
d	0.175	0.223	0.360	in
area	0.000249	0.000835	0.003095	in^2
visc(mu)	1.23E-05	1.23E-05	1.23E-05	lb/sec-ft
k	0.0152	0.0152	0.0152	BTU/ft-hr-F

Test # :	16.1 Date:			
Location	A	B	C	
Flowrate	0.0151	0.0151	0.0151	#/sec
Radius	19.0	19.0	16.5	in
H	0.127	0.127	0.196	in
W	0.283	0.950	2.280	in
Pc	161.7	161.7	161.7	psia
Tc	512.7	512.7	512.7	deg R
Tw	581.8	581.8	581.8	deg R
ROh	0.007	0.023	0.134	
REd	71417	27167	11814	
BUOY	0.0009	0.0098	0.1808	
Density	0.852	0.852	0.852	#/ft^3
Velocity	71.2	21.2	5.7	ft/sec
RPM	450	450	450	
Omega	47.1	47.1	47.1	rad/sec
d	0.175	0.223	0.360	in
area	0.000249	0.000835	0.003095	in^2
visc(mu)	1.24E-05	1.24E-05	1.24E-05	lb/sec-ft
k	0.0152	0.0152	0.0152	BTU/ft-hr-F



1.15 Full Scale Model  
Low Coolant Flow Rate  
750 rpm

Test # :	12.3 Date:			
Location	A	B	C	
Flowrate	0.0039	0.0039	0.0039	#/sec
Radius	19.0	19.0	16.5	in
H	0.127	0.127	0.196	in
W	0.283	0.950	2.280	in
Pc	164.3	164.3	164.3	psia
Tc	546.4	546.4	546.4	deg R
Tw	581.8	581.8	581.8	deg R
ROh	0.043	0.144	0.824	
REd	18127	6896	2999	
BUOY	0.0168	0.1888	3.4866	
Density	0.812	0.812	0.812	#/ft^3
Velocity	19.3	5.8	1.6	ft/sec
RPM	750	750	750	
Omega	78.5	78.5	78.5	rad/sec
d	0.175	0.223	0.360	in
area	0.000249	0.000835	0.003095	in^2
visc(mu)	1.26E-05	1.26E-05	1.26E-05	lb/sec-ft
k	0.0156	0.0156	0.0156	BTU/ft-hr-F
Test # :	16.6 Date:			
Location	A	B	C	
Flowrate	0.0038	0.0038	0.0038	#/sec
Radius	19.0	19.0	16.5	in
H	0.127	0.127	0.196	in
W	0.283	0.950	2.280	in
Pc	165.2	165.2	165.2	psia
Tc	542.6	542.6	542.6	deg R
Tw	581.6	581.6	581.6	deg R
ROh	0.045	0.151	0.863	
REd	17556	6678	2904	
BUOY	0.0203	0.2285	4.2197	
Density	0.823	0.823	0.823	#/ft^3
Velocity	18.5	5.5	1.5	ft/sec
RPM	750	750	750	
Omega	78.5	78.5	78.5	rad/sec
d	0.175	0.223	0.360	in
area	0.000249	0.000835	0.003095	in^2
visc(mu)	1.26E-05	1.26E-05	1.26E-05	lb/sec-ft
k	0.0155	0.0155	0.0155	BTU/ft-hr-F

1.15 Full Scale Model  
Median Coolant Flow Rate  
750 rpm

Test # :

12.2 Date:

Location	A	B	C	
Flowrate	0.0075	0.0075	0.0075	#/sec
Radius	19.0	19.0	16.5	in
H	0.127	0.127	0.196	in
W	0.283	0.950	2.280	in
Pc	164.1	164.1	164.1	psia
Tc	533.9	533.9	533.9	deg R
Tw	581.0	581.0	581.0	deg R
ROh	0.023	0.076	0.438	
REd	35097	13351	5806	
BUOY	0.0063	0.0712	1.3146	
Density	0.830	0.830	0.830	#/ft^3
Velocity	36.3	10.8	2.9	ft/sec
RPM	750	750	750	
Omega	78.5	78.5	78.5	rad/sec
d	0.175	0.223	0.360	in
area	0.000249	0.000835	0.003095	in^2
visc(mu)	1.25E-05	1.25E-05	1.25E-05	lb/sec-ft
k	0.0154	0.0154	0.0154	BTU/ft-hr-F

Test # :

16.3 Date:

Location	A	B	C	
Flowrate	0.0074	0.0074	0.0074	#/sec
Radius	19.0	19.0	16.5	in
H	0.127	0.127	0.196	in
W	0.283	0.950	2.280	in
Pc	164.1	164.1	164.1	psia
Tc	529.0	529.0	529.0	deg R
Tw	580.8	580.8	580.8	deg R
ROh	0.023	0.078	0.446	
REd	34899	13275	5773	
BUOY	0.0072	0.0812	1.4991	
Density	0.838	0.838	0.838	#/ft^3
Velocity	35.7	10.6	2.9	ft/sec
RPM	750	750	750	
Omega	78.5	78.5	78.5	rad/sec
d	0.175	0.223	0.360	in
area	0.000249	0.000835	0.003095	in^2
visc(mu)	1.25E-05	1.25E-05	1.25E-05	lb/sec-ft
k	0.0154	0.0154	0.0154	BTU/ft-hr-F

1.15 Full Scale Model  
Median Coolant Flow Rate  
750 rpm

Test # :	14.3 Date:			
Location	A	B	C	
Flowrate	0.0074	0.0074	0.0074	#/sec
Radius	19.0	19.0	16.5	in
H	0.127	0.127	0.196	in
W	0.283	0.950	2.280	in
Pc	164.4	164.4	164.4	psia
Tc	542.0	542.0	542.0	deg R
Tw	584.1	584.1	584.1	deg R
ROh	0.023	0.077	0.439	
REd	34376	13076	5686	
BUOY	0.0056	0.0634	1.1708	
Density	0.819	0.819	0.819	#/ft^3
Velocity	36.3	10.8	2.9	ft/sec
RPM	750	750	750	
Omega	78.5	78.5	78.5	rad/sec
d	0.175	0.223	0.360	in
area	0.000249	0.000835	0.003095	in^2
visc(mu)	1.26E-05	1.26E-05	1.26E-05	lb/sec-ft
k	0.0156	0.0156	0.0156	BTU/ft-hr-F

1.15 Full Scale Model  
High Coolant Flow Rate  
750 rpm

Test # :	12.1 Date:			
Location	A	B	C	
Flowrate	0.0150	0.0150	0.0150	#/sec
Radius	19.0	19.0	16.5	in
H	0.127	0.127	0.196	in
W	0.283	0.950	2.280	in
Pc	163.6	163.6	163.6	psia
Tc	522.4	522.4	522.4	deg R
Tw	582.2	582.2	582.2	deg R
ROh	0.012	0.039	0.223	
REd	70633	26869	11684	
BUOY	0.0021	0.0234	0.4325	
Density	0.846	0.846	0.846	#/ft^3
Velocity	71.3	21.2	5.7	ft/sec
RPM	750	750	750	
Omega	78.5	78.5	78.5	rad/sec
d	0.175	0.223	0.360	in
area	0.000249	0.000835	0.003095	in^2
visc(mu)	1.24E-05	1.24E-05	1.24E-05	lb/sec-ft
k	0.0153	0.0153	0.0153	BTU/ft-hr-F
Test # :	16.2 Date:			
Location	A	B	C	
Flowrate	0.0151	0.0151	0.0151	#/sec
Radius	19.0	19.0	16.5	in
H	0.127	0.127	0.196	in
W	0.283	0.950	2.280	in
Pc	161.7	161.7	161.7	psia
Tc	516.3	516.3	516.3	deg R
Tw	581.3	581.3	581.3	deg R
ROh	0.012	0.039	0.222	
REd	71349	27141	11803	
BUOY	0.0022	0.0252	0.4654	
Density	0.846	0.846	0.846	#/ft^3
Velocity	71.7	21.4	5.8	ft/sec
RPM	750	750	750	
Omega	78.5	78.5	78.5	rad/sec
d	0.175	0.223	0.360	in
area	0.000249	0.000835	0.003095	in^2
visc(mu)	1.24E-05	1.24E-05	1.24E-05	lb/sec-ft
k	0.0153	0.0153	0.0153	BTU/ft-hr-F

1.15 Full Scale Model  
High Coolant Flow Rate  
750 rpm

Test # :	14.2 Date:			
Location	A	B	C	
Flowrate	0.0150	0.0150	0.0150	#/sec
Radius	19.0	19.0	16.5	in
H	0.127	0.127	0.196	in
W	0.283	0.950	2.280	in
Pc	161.9	145.0	145.0	psia
Tc	523.5	523.5	523.5	deg R
Tw	583.6	583.6	583.6	deg R
ROh	0.011	0.034	0.198	
REd	70508	26821	11664	
BUOY	0.0020	0.0184	0.3394	
Density	0.835	0.748	0.748	#/ft^3
Velocity	72.2	24.0	6.5	ft/sec
RPM	750	750	750	
Omega	78.5	78.5	78.5	rad/sec
d	0.175	0.223	0.360	in
area	0.000249	0.000835	0.003095	in^2
visc(mu)	1.25E-05	1.25E-05	1.25E-05	lb/sec-ft
k	0.0154	0.0154	0.0154	BTU/ft-hr-F

**9.3 Sample Data Table for Stationary Test Condition and Medium Flowrate  
(Test # 6.2, TC 2)**

Time	Tc	Tw	To	Tw	Q	H	NUR	NU	QW	ΔT	HR	Δp/p
0	119.9	120.7	119.9	0.000E+00	1.000E-02	1.000E-02	1.000E-02	1.000E-02	1.000E-02	8.020E-01	1.000E-02	-0.0014 *
1	115.5	120.6	119.4	-1.818E+03	3.020E+01	5.913E+00	3.209E+01	3.063E+01	3.133E+01	5.057E+00	6.195E+00	-0.0088
2	106.9	119.5	117.8	-4.499E+03	1.175E+02	9.319E+00	5.387E+01	4.863E+01	1.280E+02	1.240E+01	1.032E+01	-0.0217
3	97.2	118.0	115.1	-6.693E+03	2.390E+02	1.150E+01	6.559E+01	6.052E+01	2.539E+02	2.037E+01	1.246E+01	-0.0360
4	90.9	115.8	113.2	-5.995E+03	3.292E+02	1.320E+01	7.597E+01	6.994E+01	3.495E+02	2.437E+01	1.434E+01	-0.0433
5	85.4	113.9	111.3	-6.476E+03	3.888E+02	1.363E+01	7.769E+01	7.261E+01	4.064E+02	2.787E+01	1.458E+01	-0.0497
6	80.3	111.6	109.0	-6.638E+03	4.517E+02	1.440E+01	8.278E+01	7.717E+01	4.726E+02	3.060E+01	1.545E+01	-0.0549
7	77.5	109.9	107.5	-6.077E+03	4.960E+02	1.532E+01	8.732E+01	8.240E+01	5.119E+02	3.153E+01	1.624E+01	-0.0568
8	75.1	108.3	106.1	-5.548E+03	5.209E+02	1.571E+01	8.955E+01	8.477E+01	5.356E+02	3.227E+01	1.660E+01	-0.0583
9	72.8	106.9	104.7	-5.310E+03	5.406E+02	1.586E+01	9.021E+01	8.582E+01	5.530E+02	3.317E+01	1.667E+01	-0.0601
10	70.9	105.4	103.2	-4.933E+03	5.567E+02	1.614E+01	9.215E+01	8.755E+01	5.700E+02	3.356E+01	1.699E+01	-0.0610
11	69.6	104.1	102.1	-4.580E+03	5.667E+02	1.640E+01	9.361E+01	8.914E+01	5.786E+02	3.361E+01	1.722E+01	-0.0613
12	68.5	103.0	101.1	-4.372E+03	5.748E+02	1.670E+01	9.529E+01	9.093E+01	5.854E+02	3.346E+01	1.750E+01	-0.0612
13	67.5	101.9	100.1	-4.195E+03	5.829E+02	1.695E+01	9.681E+01	9.248E+01	5.928E+02	3.341E+01	1.775E+01	-0.0612
14	66.6	100.6	99.0	-4.109E+03	5.915E+02	1.739E+01	9.984E+01	9.505E+01	6.031E+02	3.302E+01	1.827E+01	-0.0607
15	65.9	99.5	98.2	-3.829E+03	5.975E+02	1.780E+01	1.021E+02	9.743E+01	6.075E+02	3.256E+01	1.866E+01	-0.0600
16	65.3	98.5	97.5	-3.630E+03	6.000E+02	1.806E+01	1.036E+02	9.897E+01	6.089E+02	3.221E+01	1.890E+01	-0.0595
17	64.6	97.6	96.7	-3.355E+03	6.001E+02	1.821E+01	1.045E+02	9.995E+01	6.083E+02	3.194E+01	1.905E+01	-0.0591
18	63.9	96.5	95.8	-3.257E+03	5.998E+02	1.842E+01	1.061E+02	1.012E+02	6.096E+02	3.156E+01	1.932E+01	-0.0585
19	63.4	95.6	95.2	-2.870E+03	5.985E+02	1.850E+01	1.064E+02	1.018E+02	6.041E+02	3.124E+01	1.934E+01	-0.0580
20	63.1	95.0	94.6	-2.752E+03	5.908E+02	1.852E+01	1.063E+02	1.020E+02	5.968E+02	3.091E+01	1.931E+01	-0.0575
21	62.7	94.3	94.0	-2.748E+03	5.895E+02	1.863E+01	1.070E+02	1.026E+02	5.954E+02	3.066E+01	1.942E+01	-0.0571
22	62.3	93.5	93.3	-2.616E+03	5.888E+02	1.886E+01	1.088E+02	1.041E+02	5.961E+02	3.022E+01	1.972E+01	-0.0564
23	62.0	92.8	92.8	-2.535E+03	5.871E+02	1.906E+01	1.099E+02	1.052E+02	5.935E+02	2.982E+01	1.990E+01	-0.0557
24	61.7	92.1	92.3	-2.388E+03	5.846E+02	1.922E+01	1.108E+02	1.062E+02	5.906E+02	2.944E+01	2.006E+01	-0.0551
25	61.4	91.4	91.9	-2.236E+03	5.803E+02	1.932E+01	1.116E+02	1.068E+02	5.867E+02	2.907E+01	2.018E+01	-0.0545
26	60.9	90.7	91.4	-2.195E+03	5.768E+02	1.934E+01	1.117E+02	1.070E+02	5.827E+02	2.886E+01	2.019E+01	-0.0542
27	60.6	90.2	90.9	-1.899E+03	5.706E+02	1.933E+01	1.116E+02	1.071E+02	5.757E+02	2.856E+01	2.016E+01	-0.0536
28	60.6	89.8	90.5	-1.768E+03	5.617E+02	1.922E+01	1.107E+02	1.065E+02	5.650E+02	2.828E+01	1.998E+01	-0.0531
29	60.4	89.4	90.1	-1.826E+03	5.569E+02	1.920E+01	1.106E+02	1.064E+02	5.603E+02	2.807E+01	1.996E+01	-0.0528
30	60.2	88.8	89.7	-1.771E+03	5.543E+02	1.943E+01	1.125E+02	1.078E+02	5.600E+02	2.760E+01	2.029E+01	-0.0520
31	60.2	88.3	89.3	-1.703E+03	5.506E+02	1.958E+01	1.132E+02	1.086E+02	5.549E+02	2.720E+01	2.040E+01	-0.0513
32	60.0	87.8	89.0	-1.755E+03	5.486E+02	1.972E+01	1.140E+02	1.094E+02	5.528E+02	2.691E+01	2.054E+01	-0.0508
33	59.8	87.3	88.6	-1.647E+03	5.465E+02	1.990E+01	1.154E+02	1.105E+02	5.515E+02	2.655E+01	2.077E+01	-0.0502
34	59.4	86.8	88.2	-1.615E+03	5.432E+02	1.978E+01	1.145E+02	1.099E+02	5.471E+02	2.656E+01	2.060E+01	-0.0502
35	59.3	86.4	87.9	-1.493E+03	5.393E+02	1.988E+01	1.152E+02	1.106E+02	5.431E+02	2.623E+01	2.071E+01	-0.0496
36	59.2	86.1	87.6	-1.427E+03	5.342E+02	1.984E+01	1.148E+02	1.104E+02	5.372E+02	2.603E+01	2.064E+01	-0.0493
37	59.0	85.7	87.3	-1.315E+03	5.288E+02	1.979E+01	1.146E+02	1.101E+02	5.319E+02	2.584E+01	2.059E+01	-0.0490
38	58.8	85.3	86.9	-1.397E+03	5.253E+02	1.987E+01	1.153E+02	1.107E+02	5.293E+02	2.556E+01	2.071E+01	-0.0485
39	58.8	84.9	86.7	-1.322E+03	5.230E+02	2.000E+01	1.160E+02	1.114E+02	5.264E+02	2.528E+01	2.083E+01	-0.0480
40	58.6	84.6	86.4	-1.223E+03	5.184E+02	1.995E+01	1.156E+02	1.112E+02	5.211E+02	2.512E+01	2.074E+01	-0.0477
41	58.5	84.2	86.1	-1.221E+03	5.141E+02	1.999E+01	1.161E+02	1.114E+02	5.177E+02	2.486E+01	2.082E+01	-0.0473
42	58.3	83.9	85.8	-1.132E+03	5.100E+02	1.987E+01	1.152E+02	1.108E+02	5.124E+02	2.482E+01	2.065E+01	-0.0472
43	58.3	83.6	85.5	-1.119E+03	5.056E+02	1.995E+01	1.158E+02	1.113E+02	5.084E+02	2.449E+01	2.076E+01	-0.0466
44	58.2	83.3	85.3	-1.167E+03	5.033E+02	2.003E+01	1.163E+02	1.118E+02	5.059E+02	2.428E+01	2.083E+01	-0.0462
45	58.1	83.0	85.1	-1.185E+03	5.024E+02	2.018E+01	1.173E+02	1.126E+02	5.055E+02	2.406E+01	2.101E+01	-0.0459
46	57.9	82.6	84.8	-1.083E+03	4.998E+02	2.025E+01	1.179E+02	1.131E+02	5.032E+02	2.384E+01	2.111E+01	-0.0455
47	57.8	82.3	84.6	-9.698E+02	4.945E+02	2.019E+01	1.173E+02	1.128E+02	4.971E+02	2.367E+01	2.100E+01	-0.0452
48	57.7	82.0	84.5	-9.076E+02	4.888E+02	2.010E+01	1.168E+02	1.123E+02	4.913E+02	2.350E+01	2.090E+01	-0.0449
49	57.6	81.8	84.2	-8.724E+02	4.837E+02	2.000E+01	1.162E+02	1.118E+02	4.858E+02	2.338E+01	2.078E+01	-0.0446
50	57.4	81.6	83.9	-7.856E+02	4.782E+02	1.975E+01	1.145E+02	1.104E+02	4.797E+02	2.342E+01	2.048E+01	-0.0447
51	57.5	81.4	83.7	-7.797E+02	4.729E+02	1.977E+01	1.148E+02	1.106E+02	4.749E+02	2.313E+01	2.053E+01	-0.0442
52	57.5	81.2	83.6	-7.692E+02	4.689E+02	1.973E+01	1.145E+02	1.103E+02	4.704E+02	2.299E+01	2.046E+01	-0.0439
53	57.4	81.0	83.4	-8.988E+02	4.676E+02	1.979E+01	1.149E+02	1.107E+02	4.694E+02	2.285E+01	2.055E+01	-0.0437
54	57.3	80.7	83.1	-9.489E+02	4.685E+02	2.001E+01	1.166E+02	1.120E+02	4.716E+02	2.263E+01	2.084E+01	-0.0433
55	57.2	80.4	83.0	-9.166E+02	4.680E+02	2.018E+01	1.175E+02	1.129E+02	4.704E+02	2.242E+01	2.098E+01	-0.0429
56	57.2	80.2	82.9	-9.125E+02	4.667E+02	2.030E+01	1.182E+02	1.137E+02	4.689E+02	2.221E+01	2.111E+01	-0.0426
57	57.1	79.9	82.7	-9.013E+02	4.654E+02	2.040E+01	1.189E+02	1.143E+02	4.677E+02	2.204E+01	2.122E+01	-0.0423
58	57.0	79.6	82.4	-8.588E+02	4.635E+02	2.048E+01	1.196E+02	1.148E+02	4.664E+02	2.186E+01	2.134E+01	-0.0419
59	56.9	79.4	82.3	-7.174E+02	4.592E+02	2.044E+01	1.191E+02	1.146E+02	4.612E+02	2.170E+01	2.126E+01	-0.0416
60	56.9	79.2	82.1	-7.829E+02	4.556E+02	2.044E+01	1.190E+02	1.146E+02	4.570E+02	2.153E+01	2.123E+01	-0.0413
61	56.9	79.1	81.9	-7.736E+02	4.541E+02	2.046E+01	1.191E+02	1.147E+02	4.555E+02	2.144E+01	2.125E+01	-0.0412
62	56.8	78.7	81.7	-7.501E+02	4.519E+02	2.057E+01	1.202E+02	1.153E+02	4.548E+02	2.121E+01	2.144E+01	-0.0408
63	56.7	78.5	81.6	-6.513E+02	4.481E+02	2.047E+01	1.193E+02	1.148E+02	4.498E+02	2.114E+01	2.128E+01	-0.0406
64	56.6	78.4	81.4	-5.626E+02	4.426E+02	2.031E+01	1.183E+02	1.139E+02	4.440E+02	2.105E+01	2.109E+01	-0.0405
65	56.5	78.2	81.2	-5.411E+02	4.375E+02	2.016E+01	1.174E+02	1.131E+02	4.387E+02	2.097E+01	2.092E+01	-0.0403
66	56.4	78.1	81.1	-5.620E+02	4.339E+02	2.002E+01	1.165E+02	1.123E+02	4.351E+02	2.095E+01	2.077E+01	-0.0403
67	56.4	78.0	80.9	-5.171E+02	4.305E+02	1.994E+01	1.161E+02	1.119E+02	4.318E+02	2.087E+01	2.069E+01	-0.0401

68	56.3	77.9	80.8	-3.976E+02	4.249E+02	1.968E+01	1.143E+02	1.105E+02	4.252E+02	2.088E+01	2.037E+01	-0.0401
69	56.5	77.8	80.7	-5.041E+02	4.209E+02	1.969E+01	1.145E+02	1.105E+02	4.216E+02	2.068E+01	2.039E+01	-0.0397
70	56.4	77.7	80.5	-6.535E+02	4.219E+02	1.979E+01	1.153E+02	1.111E+02	4.233E+02	2.061E+01	2.054E+01	-0.0396
71	56.3	77.4	80.4	-5.239E+02	4.210E+02	1.994E+01	1.165E+02	1.120E+02	4.233E+02	2.041E+01	2.074E+01	-0.0393
72	56.3	77.3	80.3	-6.696E+02	4.200E+02	2.004E+01	1.168E+02	1.126E+02	4.211E+02	2.025E+01	2.079E+01	-0.0390
73	56.3	77.1	80.1	-6.430E+02	4.208E+02	2.026E+01	1.183E+02	1.138E+02	4.227E+02	2.007E+01	2.106E+01	-0.0387
74	56.3	76.9	79.9	-5.712E+02	4.189E+02	2.033E+01	1.188E+02	1.142E+02	4.209E+02	1.991E+01	2.114E+01	-0.0384
75	56.2	76.7	79.8	-4.873E+02	4.151E+02	2.027E+01	1.183E+02	1.139E+02	4.164E+02	1.978E+01	2.105E+01	-0.0381
76	56.3	76.6	79.7	-4.861E+02	4.115E+02	2.027E+01	1.183E+02	1.139E+02	4.129E+02	1.961E+01	2.105E+01	-0.0378
77	56.2	76.5	79.6	-4.742E+02	4.089E+02	2.018E+01	1.175E+02	1.134E+02	4.093E+02	1.958E+01	2.090E+01	-0.0378
78	56.3	76.4	79.4	-5.279E+02	4.074E+02	2.022E+01	1.179E+02	1.137E+02	4.083E+02	1.947E+01	2.098E+01	-0.0376
79	56.2	76.2	79.4	-6.012E+02	4.078E+02	2.035E+01	1.189E+02	1.144E+02	4.092E+02	1.935E+01	2.114E+01	-0.0374
80	56.1	76.2	79.3	-6.022E+02	4.083E+02	2.036E+01	1.187E+02	1.145E+02	4.090E+02	1.937E+01	2.112E+01	-0.0374
81	56.0	75.8	79.2	-5.820E+02	4.077E+02	2.054E+01	1.205E+02	1.155E+02	4.107E+02	1.916E+01	2.143E+01	-0.0370
82	55.8	75.7	79.1	-5.246E+02	4.058E+02	2.038E+01	1.191E+02	1.147E+02	4.072E+02	1.923E+01	2.117E+01	-0.0372
83	55.7	75.5	79.0	-5.599E+02	4.043E+02	2.043E+01	1.196E+02	1.150E+02	4.062E+02	1.911E+01	2.126E+01	-0.0369
84	55.6	75.3	78.8	-5.169E+02	4.030E+02	2.046E+01	1.196E+02	1.152E+02	4.041E+02	1.903E+01	2.124E+01	-0.0368
85	55.8	75.3	78.7	-4.422E+02	3.999E+02	2.054E+01	1.199E+02	1.156E+02	4.006E+02	1.880E+01	2.131E+01	-0.0364
86	55.8	75.1	78.6	-4.566E+02	3.971E+02	2.053E+01	1.200E+02	1.156E+02	3.982E+02	1.868E+01	2.132E+01	-0.0361
87	55.8	75.0	78.5	-3.559E+02	3.937E+02	2.045E+01	1.195E+02	1.152E+02	3.946E+02	1.859E+01	2.123E+01	-0.0360
88	55.7	74.9	78.4	-3.779E+02	3.900E+02	2.031E+01	1.186E+02	1.144E+02	3.909E+02	1.855E+01	2.107E+01	-0.0359
89	55.5	74.8	78.2	-4.184E+02	3.885E+02	2.015E+01	1.179E+02	1.135E+02	3.899E+02	1.863E+01	2.093E+01	-0.0360
90	55.4	74.6	78.1	-3.230E+02	3.857E+02	2.008E+01	1.173E+02	1.131E+02	3.866E+02	1.857E+01	2.082E+01	-0.0359
91	55.4	74.6	78.0	-2.835E+02	3.814E+02	1.989E+01	1.160E+02	1.121E+02	3.816E+02	1.854E+01	2.059E+01	-0.0359
92	55.4	74.5	77.9	-2.646E+02	3.776E+02	1.972E+01	1.151E+02	1.111E+02	3.782E+02	1.852E+01	2.042E+01	-0.0358
93	55.4	74.5	77.9	-2.809E+02	3.747E+02	1.962E+01	1.144E+02	1.105E+02	3.751E+02	1.847E+01	2.031E+01	-0.0357
94	55.4	74.4	77.8	-3.251E+02	3.731E+02	1.960E+01	1.144E+02	1.104E+02	3.739E+02	1.841E+01	2.030E+01	-0.0356
95	55.4	74.3	77.8	-4.563E+02	3.741E+02	1.981E+01	1.157E+02	1.116E+02	3.750E+02	1.826E+01	2.053E+01	-0.0354
96	55.4	74.2	77.7	-4.069E+02	3.748E+02	1.997E+01	1.168E+02	1.125E+02	3.759E+02	1.814E+01	2.072E+01	-0.0351
97	55.4	74.0	77.5	-4.100E+02	3.737E+02	2.006E+01	1.176E+02	1.131E+02	3.756E+02	1.800E+01	2.086E+01	-0.0349
98	55.4	73.9	77.4	-3.032E+02	3.711E+02	2.006E+01	1.173E+02	1.131E+02	3.720E+02	1.788E+01	2.080E+01	-0.0347
99	55.5	73.8	77.3	-3.888E+02	3.692E+02	2.012E+01	1.175E+02	1.134E+02	3.697E+02	1.774E+01	2.085E+01	-0.0344
100	55.5	73.7	77.2	-3.530E+02	3.685E+02	2.022E+01	1.183E+02	1.140E+02	3.697E+02	1.762E+01	2.098E+01	-0.0342
101	55.3	73.7	77.1	-3.127E+02	3.662E+02	1.998E+01	1.166E+02	1.126E+02	3.665E+02	1.772E+01	2.068E+01	-0.0344
102	55.4	73.6	77.1	-3.583E+02	3.647E+02	2.007E+01	1.174E+02	1.132E+02	3.656E+02	1.756E+01	2.081E+01	-0.0341
103	55.3	73.5	77.0	-2.434E+02	3.622E+02	1.996E+01	1.167E+02	1.125E+02	3.630E+02	1.755E+01	2.069E+01	-0.0340
104	55.3	73.4	76.9	-3.775E+02	3.607E+02	1.996E+01	1.167E+02	1.126E+02	3.616E+02	1.747E+01	2.070E+01	-0.0339
105	55.3	73.2	76.8	-3.524E+02	3.611E+02	2.013E+01	1.180E+02	1.135E+02	3.625E+02	1.733E+01	2.091E+01	-0.0336
106	55.2	73.1	76.7	-2.657E+02	3.586E+02	1.995E+01	1.167E+02	1.125E+02	3.593E+02	1.738E+01	2.068E+01	-0.0337
107	55.2	73.1	76.6	-1.670E+02	3.540E+02	1.977E+01	1.154E+02	1.115E+02	3.541E+02	1.731E+01	2.045E+01	-0.0336
108	55.2	73.1	76.5	-2.148E+02	3.505E+02	1.965E+01	1.148E+02	1.109E+02	3.511E+02	1.725E+01	2.035E+01	-0.0335
109	55.2	73.0	76.5	-1.851E+02	3.482E+02	1.946E+01	1.134E+02	1.098E+02	3.482E+02	1.732E+01	2.011E+01	-0.0336
110	55.2	73.0	76.4	-2.271E+02	3.462E+02	1.944E+01	1.135E+02	1.097E+02	3.467E+02	1.723E+01	2.012E+01	-0.0334
111	55.1	72.9	76.3	-2.903E+02	3.460E+02	1.945E+01	1.137E+02	1.098E+02	3.468E+02	1.721E+01	2.015E+01	-0.0334
112	55.1	72.9	76.2	-3.322E+02	3.467E+02	1.946E+01	1.135E+02	1.098E+02	3.467E+02	1.724E+01	2.012E+01	-0.0334
113	55.2	72.7	76.1	-4.062E+02	3.481E+02	1.989E+01	1.168E+02	1.123E+02	3.502E+02	1.692E+01	2.070E+01	-0.0329
114	55.0	72.6	76.0	-3.604E+02	3.488E+02	1.991E+01	1.166E+02	1.124E+02	3.497E+02	1.694E+01	2.065E+01	-0.0329
115	55.0	72.5	75.9	-3.445E+02	3.479E+02	1.989E+01	1.165E+02	1.123E+02	3.489E+02	1.691E+01	2.063E+01	-0.0328
116	55.0	72.4	75.9	-3.560E+02	3.473E+02	1.993E+01	1.166E+02	1.125E+02	3.480E+02	1.685E+01	2.065E+01	-0.0327
117	55.0	72.3	75.8	-3.126E+02	3.462E+02	2.001E+01	1.172E+02	1.130E+02	3.473E+02	1.673E+01	2.076E+01	-0.0325
118	54.9	72.2	75.7	-2.528E+02	3.438E+02	1.987E+01	1.163E+02	1.122E+02	3.445E+02	1.673E+01	2.060E+01	-0.0325
119	54.9	72.1	75.7	-2.851E+02	3.419E+02	1.987E+01	1.162E+02	1.122E+02	3.423E+02	1.664E+01	2.057E+01	-0.0323
120	54.9	72.1	75.6	-3.240E+02	3.417E+02	1.990E+01	1.163E+02	1.124E+02	3.421E+02	1.661E+01	2.060E+01	-0.0323
121	55.0	72.0	75.5	-4.100E+02	3.430E+02	2.022E+01	1.186E+02	1.142E+02	3.443E+02	1.639E+01	2.100E+01	-0.0319
122	54.9	71.8	75.5	-4.385E+02	3.450E+02	2.036E+01	1.194E+02	1.150E+02	3.461E+02	1.637E+01	2.114E+01	-0.0319
123	54.8	71.7	75.4	-2.946E+02	3.438E+02	2.033E+01	1.193E+02	1.149E+02	3.449E+02	1.634E+01	2.112E+01	-0.0318
124	54.8	71.6	75.3	-2.329E+02	3.400E+02	2.018E+01	1.182E+02	1.140E+02	3.407E+02	1.628E+01	2.092E+01	-0.0317
125	54.9	71.5	75.2	-2.746E+02	3.379E+02	2.026E+01	1.188E+02	1.145E+02	3.387E+02	1.611E+01	2.102E+01	-0.0314
126	54.8	71.5	75.1	-1.671E+02	3.352E+02	2.009E+01	1.176E+02	1.135E+02	3.357E+02	1.613E+01	2.082E+01	-0.0314
127	54.9	71.5	75.1	-1.658E+02	3.316E+02	1.994E+01	1.165E+02	1.127E+02	3.314E+02	1.607E+01	2.062E+01	-0.0313
128	54.9	71.5	75.0	-1.230E+02	3.285E+02	1.980E+01	1.158E+02	1.119E+02	3.287E+02	1.604E+01	2.049E+01	-0.0312
129	54.9	71.5	75.0	-1.585E+02	3.261E+02	1.967E+01	1.149E+02	1.111E+02	3.260E+02	1.603E+01	2.033E+01	-0.0312
130	54.9	71.4	75.0	-2.783E+02	3.266E+02	1.971E+01	1.154E+02	1.114E+02	3.271E+02	1.602E+01	2.042E+01	-0.0312
131	54.8	71.3	74.9	-2.879E+02	3.279E+02	1.986E+01	1.166E+02	1.122E+02	3.292E+02	1.596E+01	2.062E+01	-0.0311
132	54.7	71.2	74.9	-3.084E+02	3.283E+02	1.994E+01	1.168E+02	1.127E+02	3.289E+02	1.591E+01	2.067E+01	-0.0310
133	54.8	71.1	74.8	-2.690E+02	3.279E+02	2.017E+01	1.185E+02	1.140E+02	3.292E+02	1.571E+01	2.096E+01	-0.0306
134	54.7	71.0	74.7	-1.726E+02	3.252E+02	1.994E+01	1.168E+02	1.127E+02	3.258E+02	1.577E+01	2.066E+01	-0.0307
135	54.6	71.0	74.6	-1.619E+02	3.221E+02	1.974E+01	1.155E+02	1.116E+02	3.223E+02	1.578E+01	2.042E+01	-0.0307
136	54.7	70.9	74.6	-1.913E+02	3.205E+02	1.970E+01	1.153E+02	1.114E+02	3.209E+02	1.573E+01	2.040E+01	-0.0306



137	54.7	70.9	74.5	-9.681E+01	3.179E+02	1.953E+01	1.141E+02	1.104E+02	3.178E+02	1.575E+01	2.018E+01	-0.0307
138	54.7	70.9	74.4	-1.440E+02	3.153E+02	1.947E+01	1.139E+02	1.101E+02	3.156E+02	1.567E+01	2.014E+01	-0.0305
139	54.7	70.9	74.3	-2.480E+02	3.158E+02	1.959E+01	1.147E+02	1.108E+02	3.163E+02	1.560E+01	2.028E+01	-0.0304
140	54.7	70.8	74.2	-3.249E+02	3.181E+02	1.979E+01	1.159E+02	1.119E+02	3.184E+02	1.554E+01	2.049E+01	-0.0303
141	54.9	70.6	74.2	-3.718E+02	3.206E+02	2.036E+01	1.199E+02	1.151E+02	3.225E+02	1.521E+01	2.121E+01	-0.0297
142	54.7	70.5	74.2	-3.068E+02	3.212E+02	2.031E+01	1.192E+02	1.148E+02	3.221E+02	1.528E+01	2.107E+01	-0.0298
143	54.5	70.4	74.1	-2.303E+02	3.193E+02	2.007E+01	1.177E+02	1.135E+02	3.200E+02	1.538E+01	2.081E+01	-0.0300
144	54.5	70.4	74.1	-2.605E+02	3.179E+02	2.000E+01	1.172E+02	1.131E+02	3.184E+02	1.537E+01	2.072E+01	-0.0300
145	54.6	70.3	74.0	-2.215E+02	3.168E+02	2.014E+01	1.182E+02	1.140E+02	3.176E+02	1.520E+01	2.089E+01	-0.0297
146	54.5	70.2	74.0	-1.541E+02	3.143E+02	2.000E+01	1.172E+02	1.131E+02	3.147E+02	1.519E+01	2.072E+01	-0.0296
147	54.6	70.2	73.9	-1.226E+02	3.112E+02	1.983E+01	1.160E+02	1.122E+02	3.111E+02	1.517E+01	2.051E+01	-0.0296
148	54.6	70.2	73.8	-1.761E+02	3.096E+02	1.975E+01	1.155E+02	1.117E+02	3.096E+02	1.516E+01	2.042E+01	-0.0296
149	54.6	70.1	73.8	-2.568E+02	3.103E+02	2.000E+01	1.174E+02	1.132E+02	3.112E+02	1.499E+01	2.076E+01	-0.0293
150	54.5	70.1	73.8	-2.739E+02	3.115E+02	2.005E+01	1.176E+02	1.135E+02	3.121E+02	1.501E+01	2.079E+01	-0.0293

Where:

Time	Seconds past start of transient portion of the test
Tc	Average coolant inlet temperature, °F
Tw	Wall temperature, F
To	Average coolant outlet temperature, °F
Tw'	Temporal derivative of the wall temperature variation, °F/hr
Q	Heat flux without paint correction, Btu/ft <sup>2</sup> /hr
H	Heat transfer coefficient without paint correction, Btu/ft <sup>2</sup> /hr/°F
NUR	Nusselt number with paint correction based on d=1 inch, HR*d/k
NU	Nusselt number without paint correction based on d=1 inch, HR*d/k
QW	Heat flux with paint correction, Btu/ft <sup>2</sup> /hr
ΔT	Temperature difference with paint correction, Tw-Tc, °F
HR	Heat transfer coefficient with paint correction, Btu/ft <sup>2</sup> /hr/°F
Δρ/ρ	Density ratio, $-(\rho_b - \rho_w)/\rho_b = -(T_w - T_b)/T_w$

## **9.4 Adjusted Thermocouple Results**

Re = 13,000

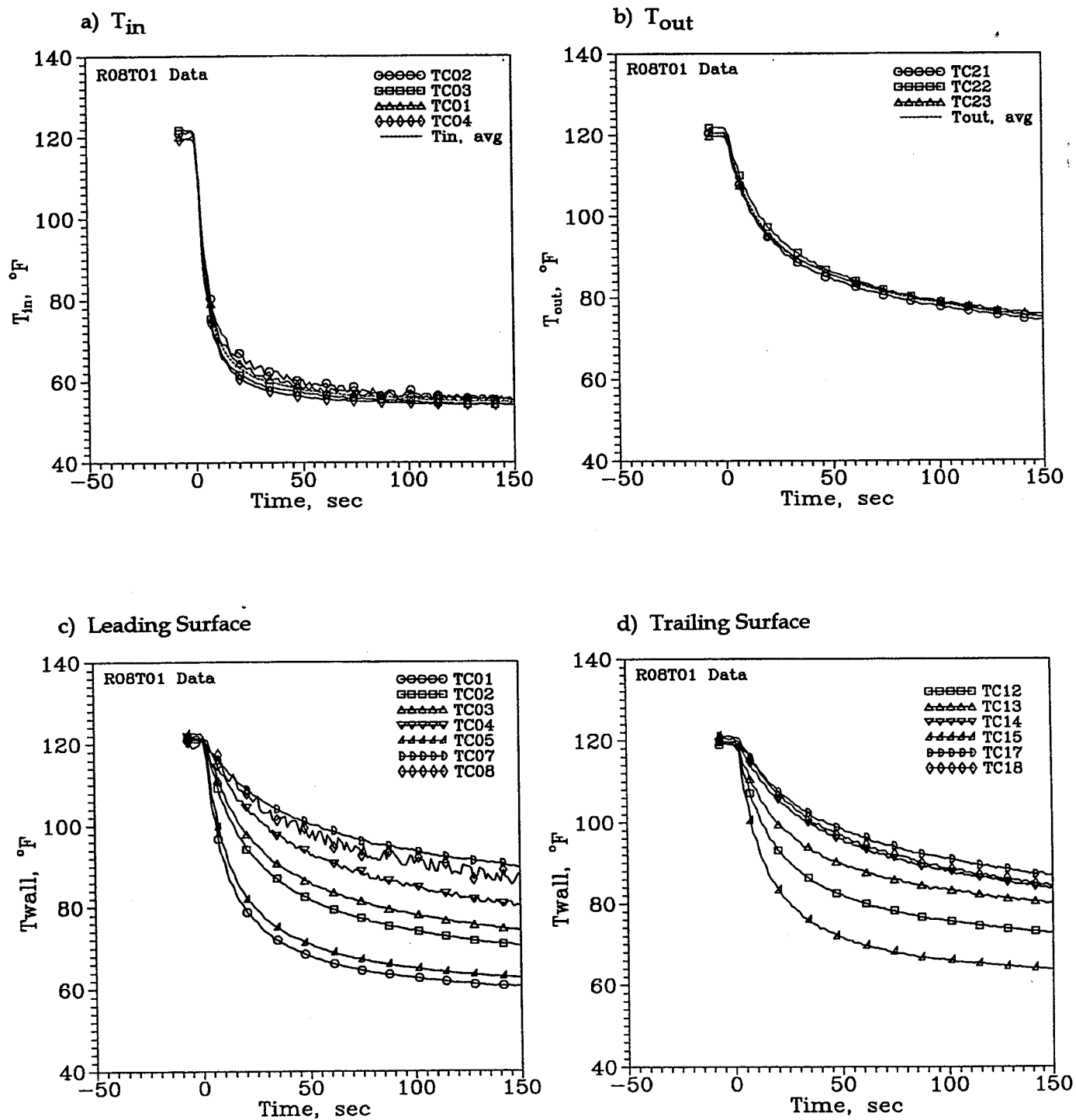


Figure 9.4-1. Thermocouple Data for Liquid Crystal Test on Leading Surface  
With  $\Omega = 0$  rpm.

Re = 13,000

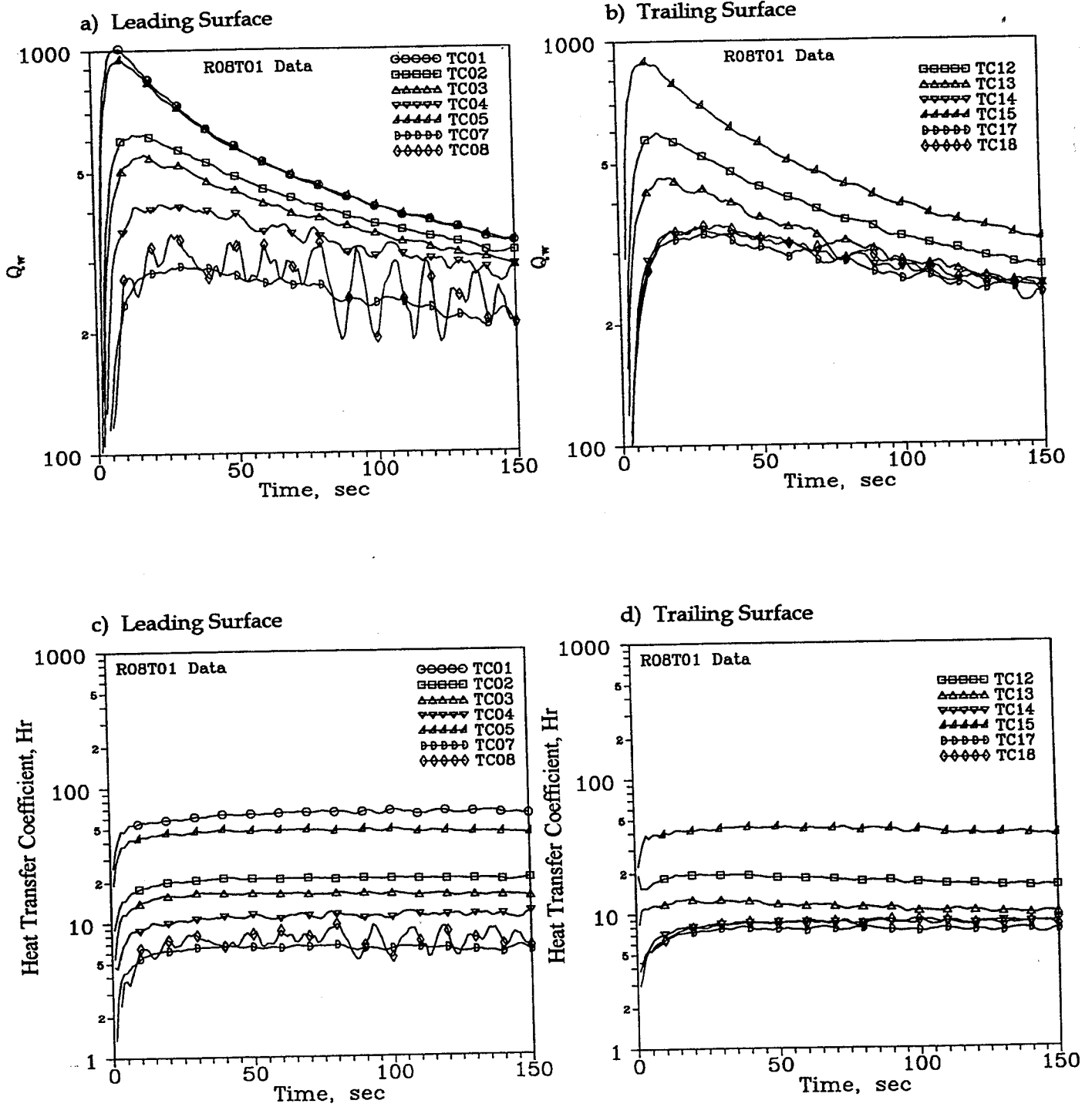


Figure 9.4-2. Results From Thermocouple Data for Liquid Crystal Test on Leading Surface With  $\Omega = 0$  rpm.

Re = 13,000

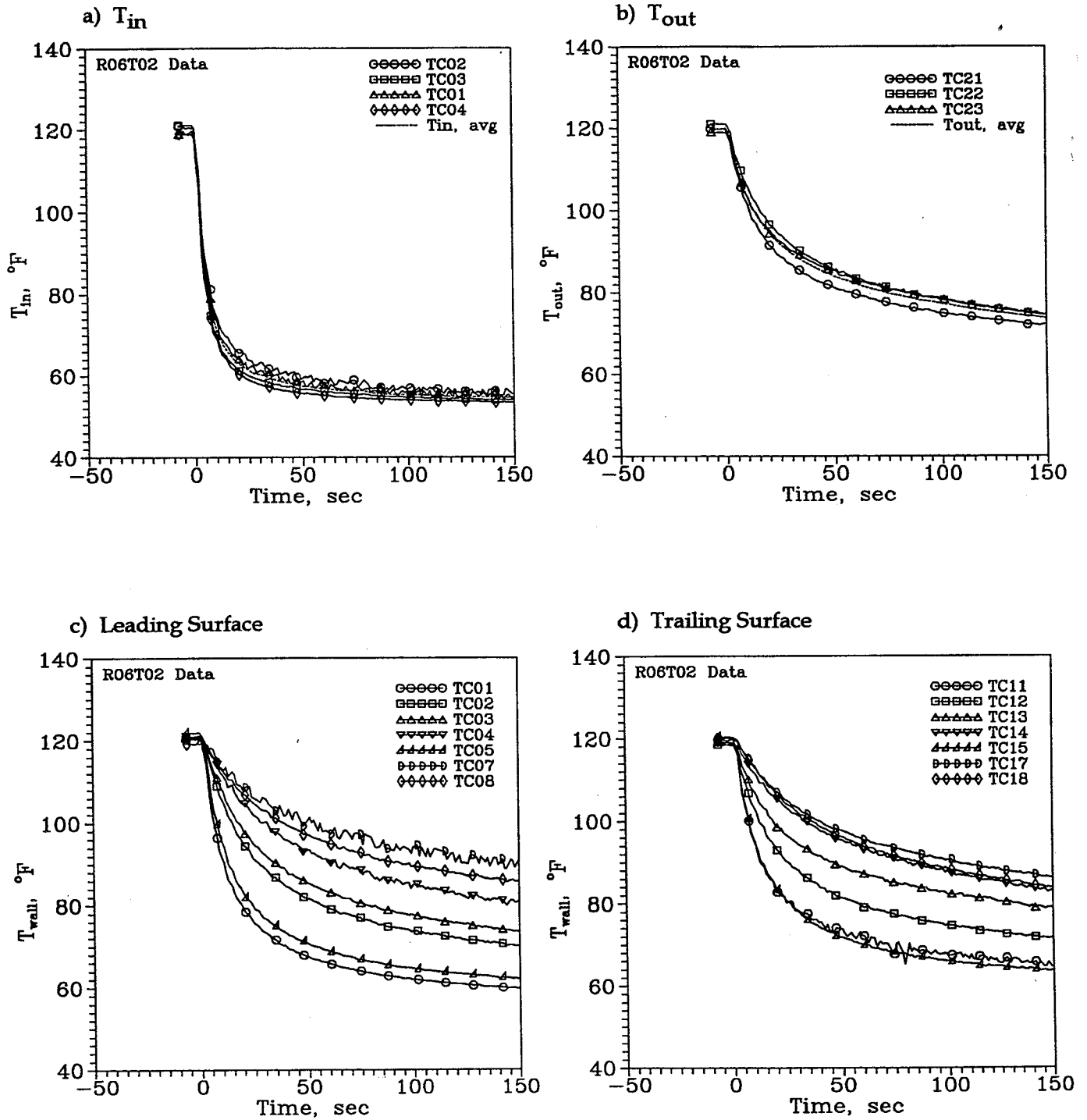


Figure 9.4-3. Thermocouple Data for Liquid Crystal Test on Trailing Surface With  $\Omega = 0$  rpm.

Re = 13,000

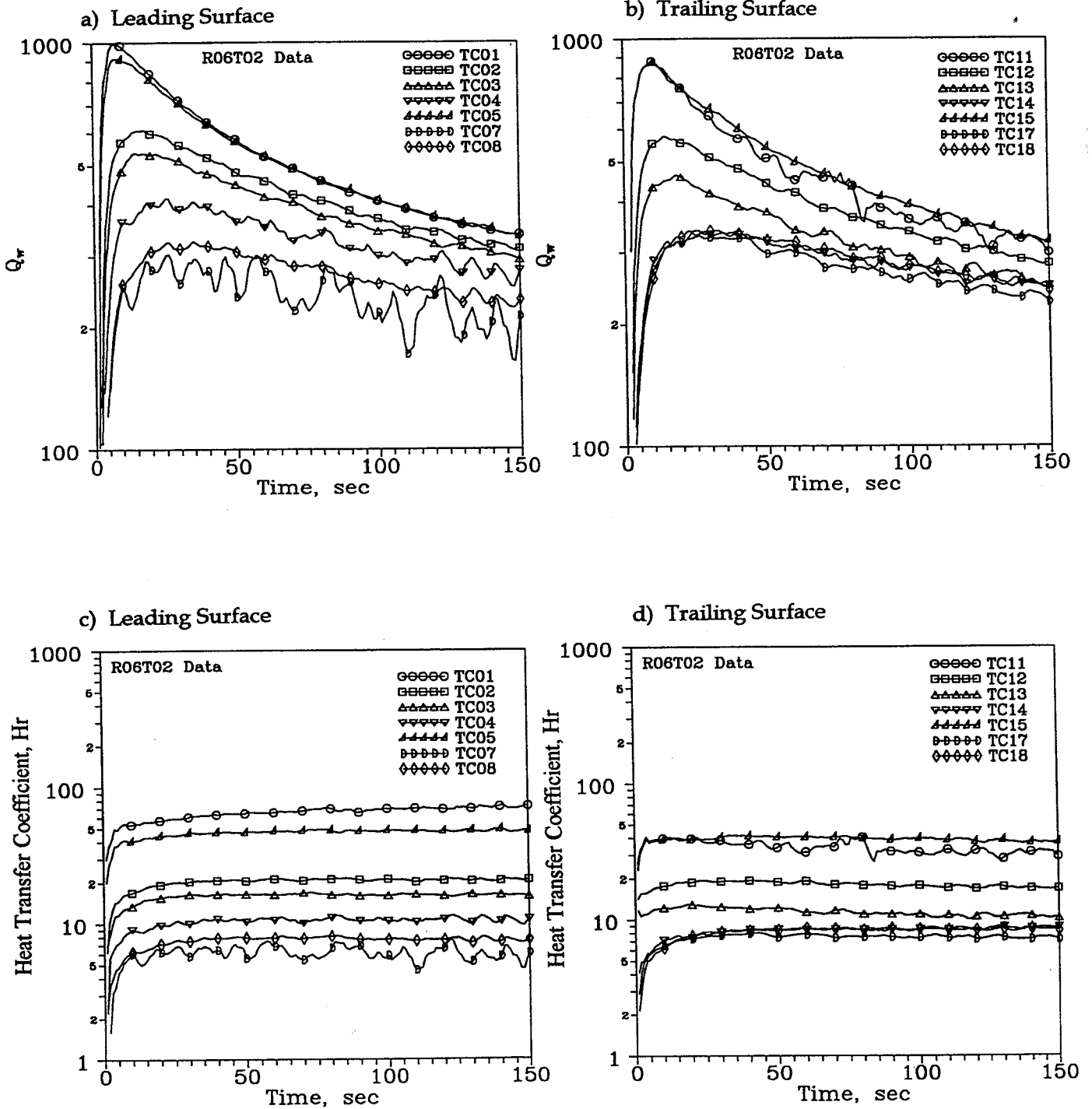
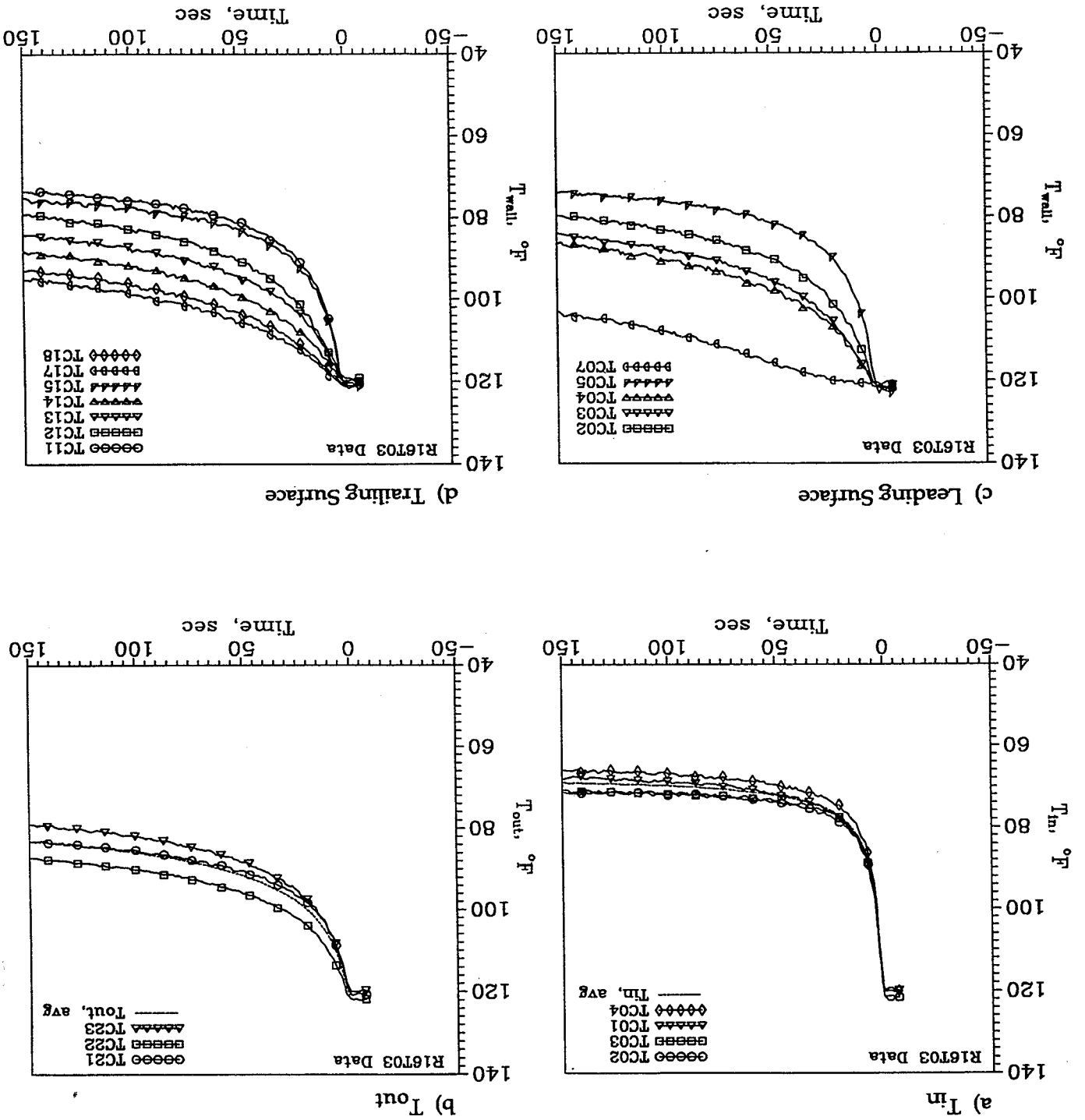


Figure 9.4-4. Results From Thermocouple Data for Liquid Crystal Test on Trailing Surface With  $\Omega = 0$  rpm.

Re = 13,000



Re = 13,000

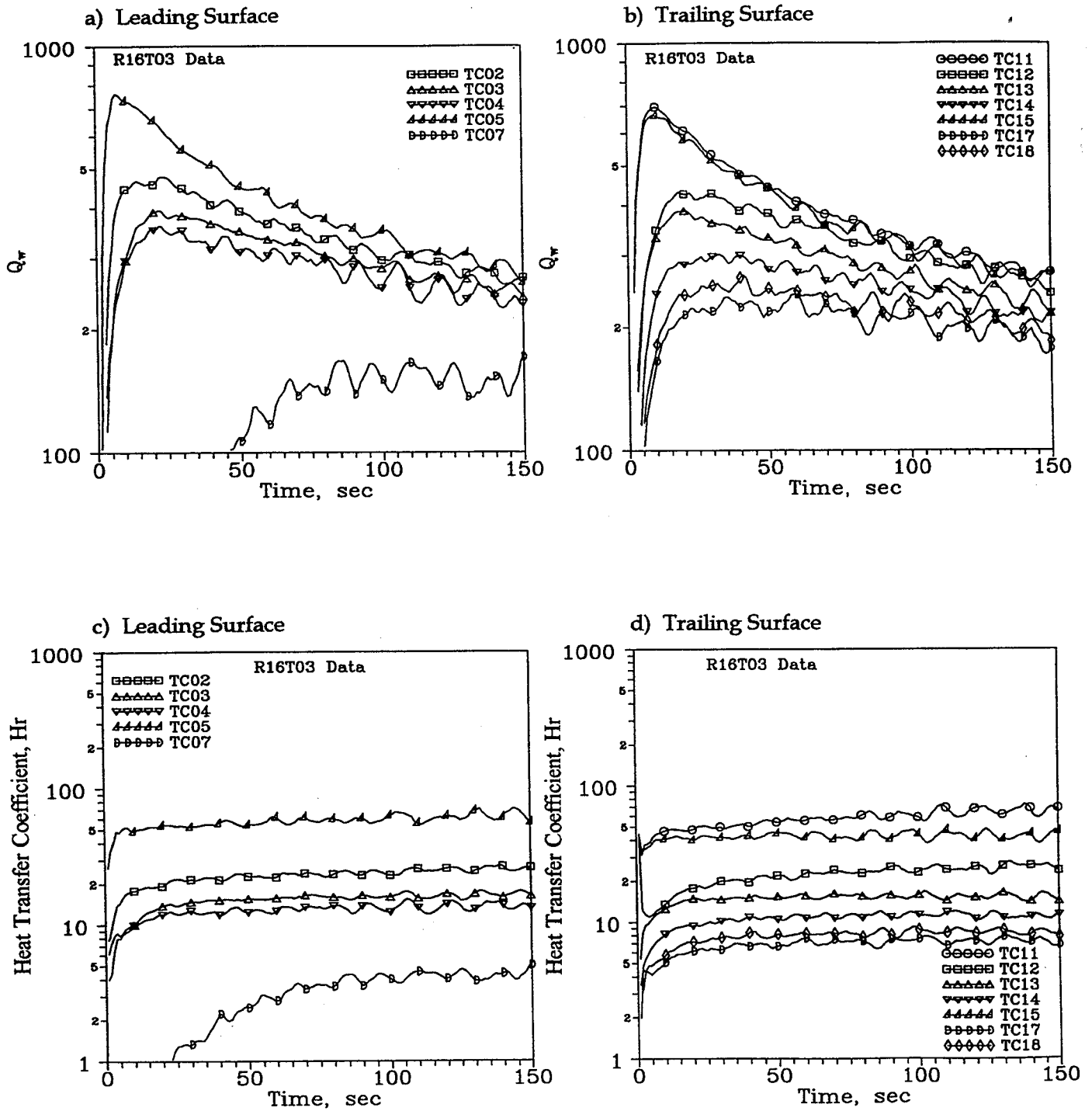


Figure 9.4-6. Results From Thermocouple Data for Liquid Crystal Test on Leading Surface With  $\Omega = 450$  rpm.



Re = 13,000

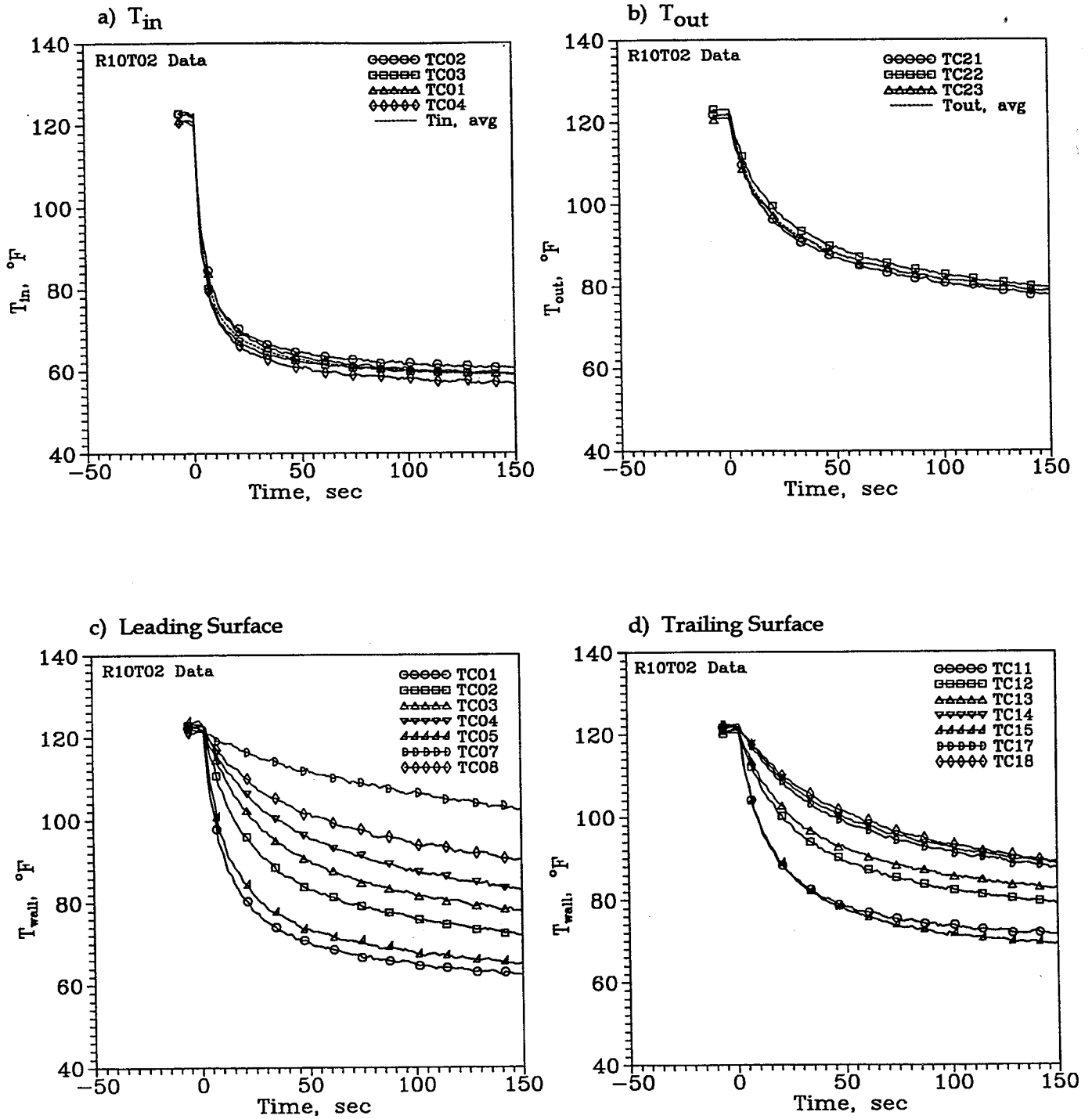


Figure 9.4-7. Thermocouple Data for Liquid Crystal Test on Trailing Surface  
With  $\Omega = 450$  rpm.

Re = 13,000

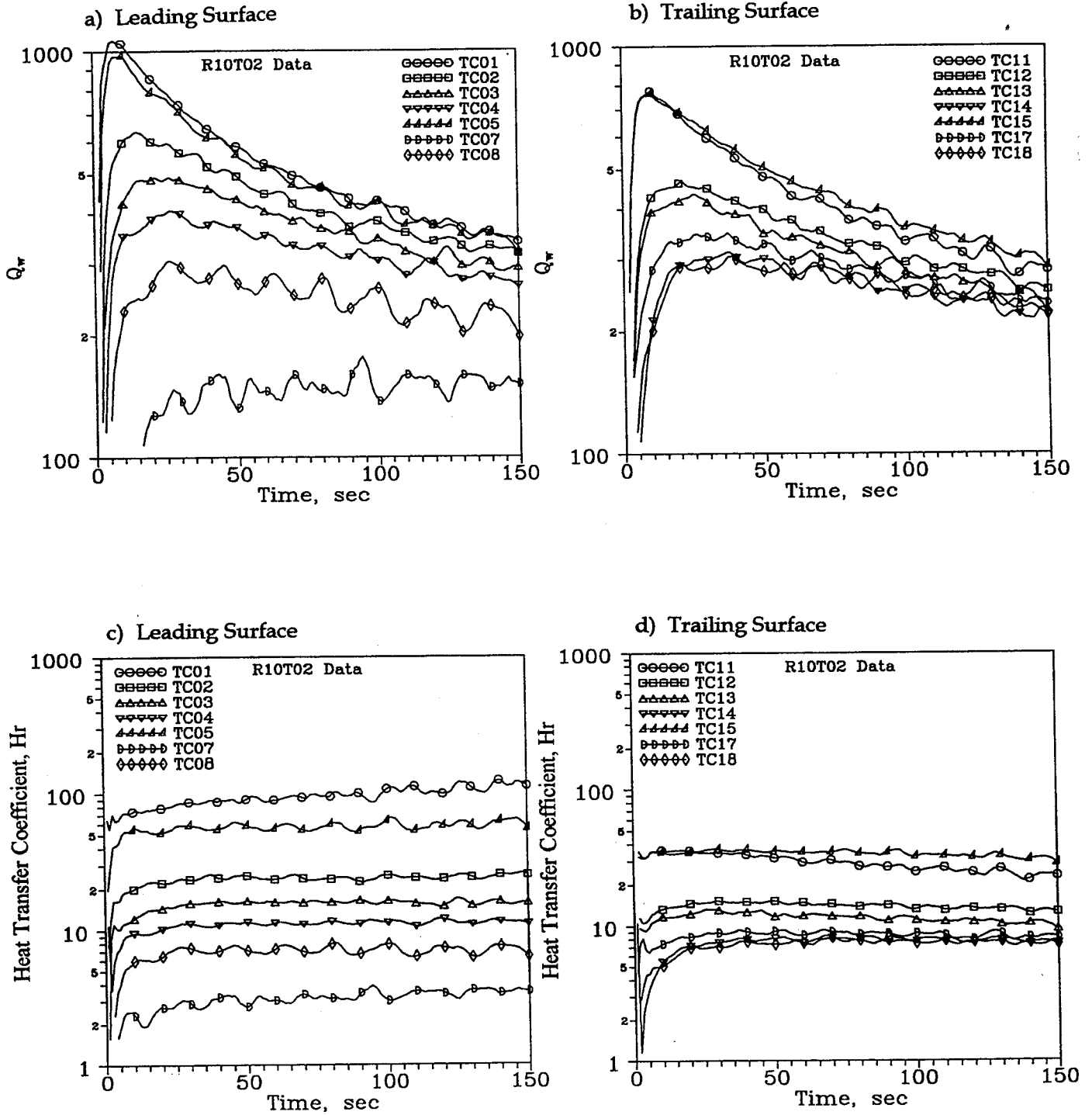


Figure 9.4-8. Results From Thermocouple Data for Liquid Crystal Test on Trailing Surface With  $\Omega = 450$  rpm.

Re = 13,000

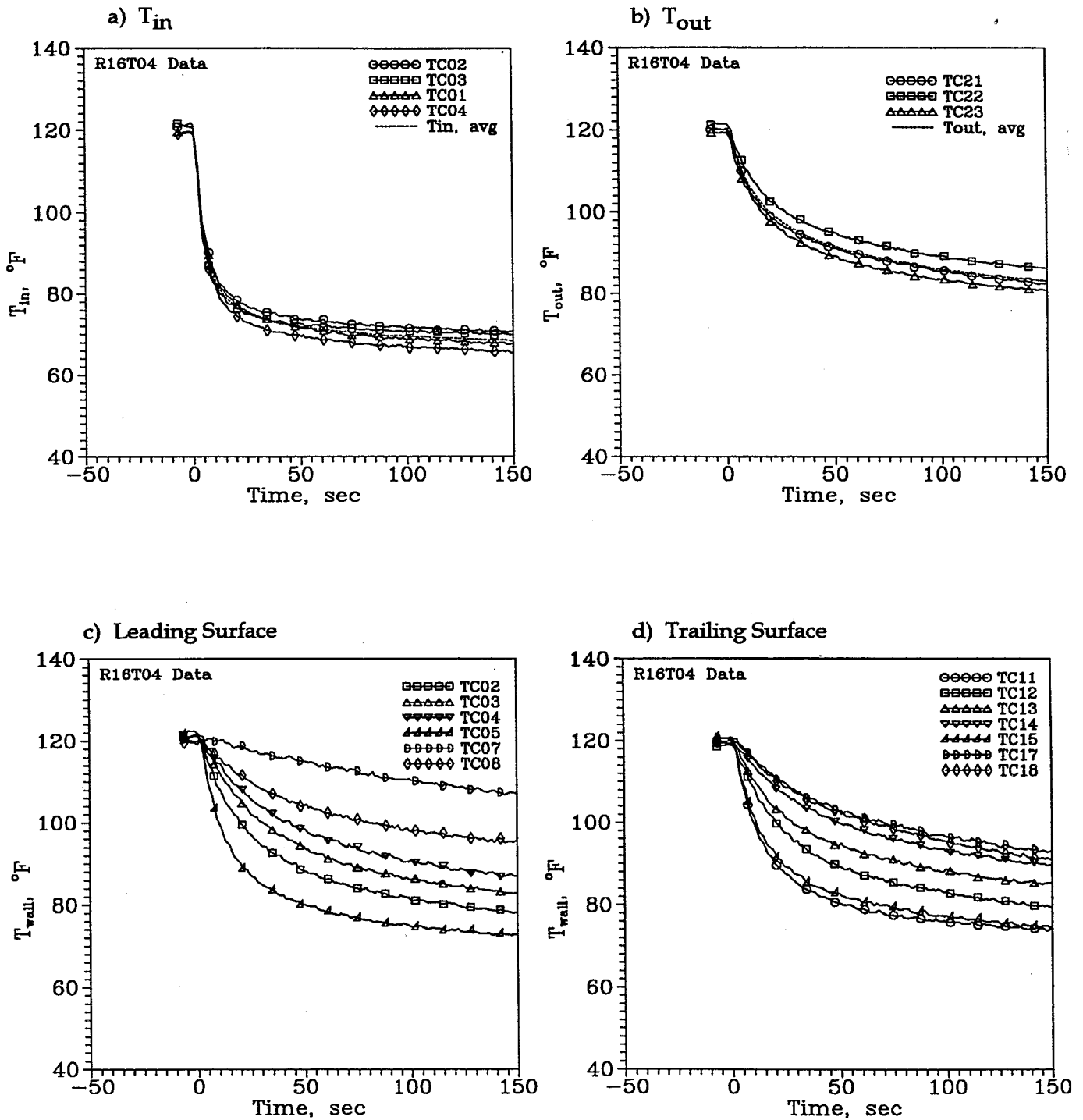


Figure 9.4-9. Thermocouple Data for Liquid Crystal Test on Leading Surface  
With  $\Omega = 750$  rpm.

Re = 13,000

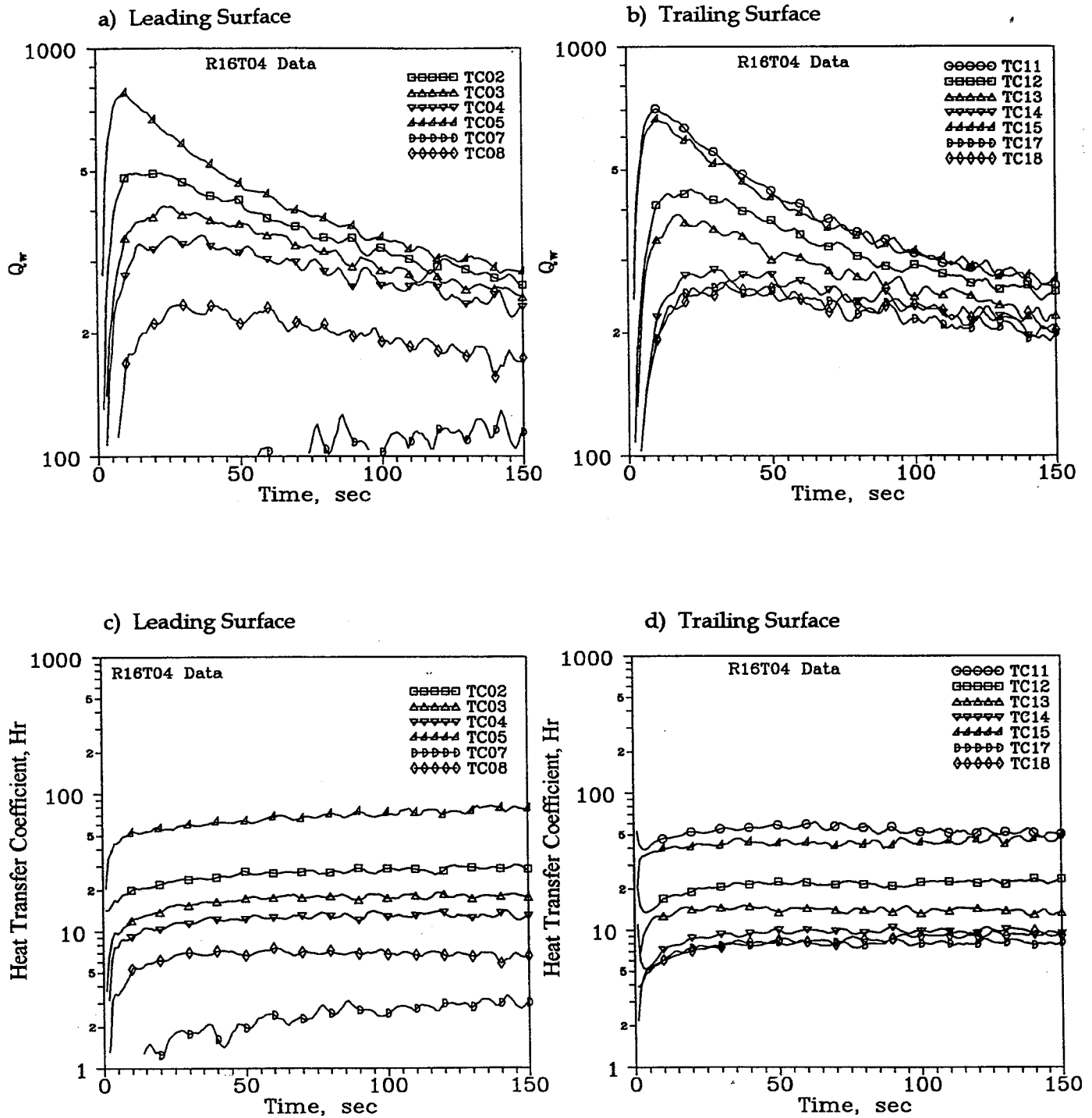


Figure 9.4-10. Results From Thermocouple Data for Liquid Crystal Test on Leading Surface With  $\Omega = 750$  rpm.

Re = 13,000

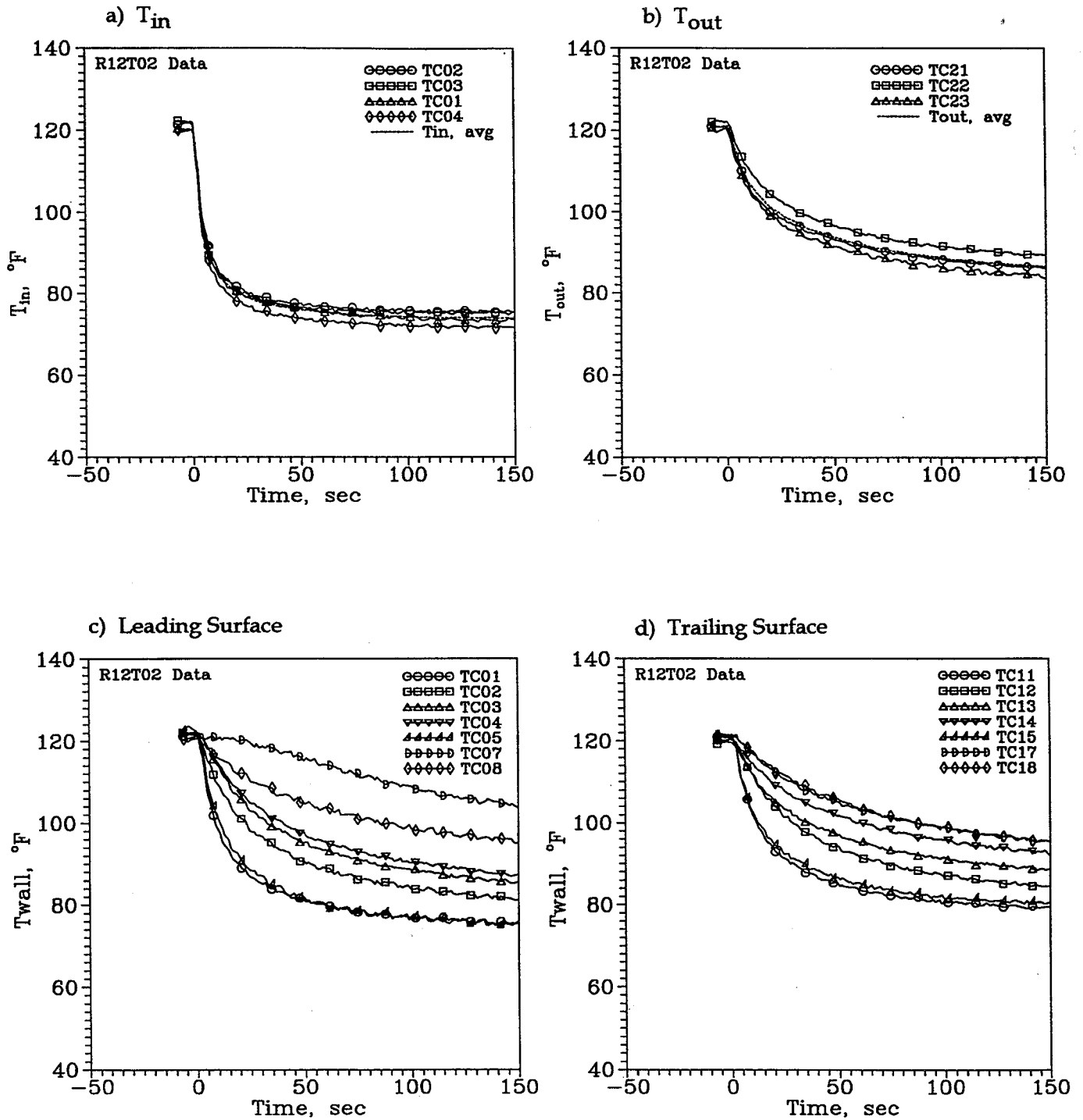


Figure 9.4-11. Thermocouple Data for Liquid Crystal Test on Trailing Surface With  $\Omega = 750$  rpm.

Re = 13,000

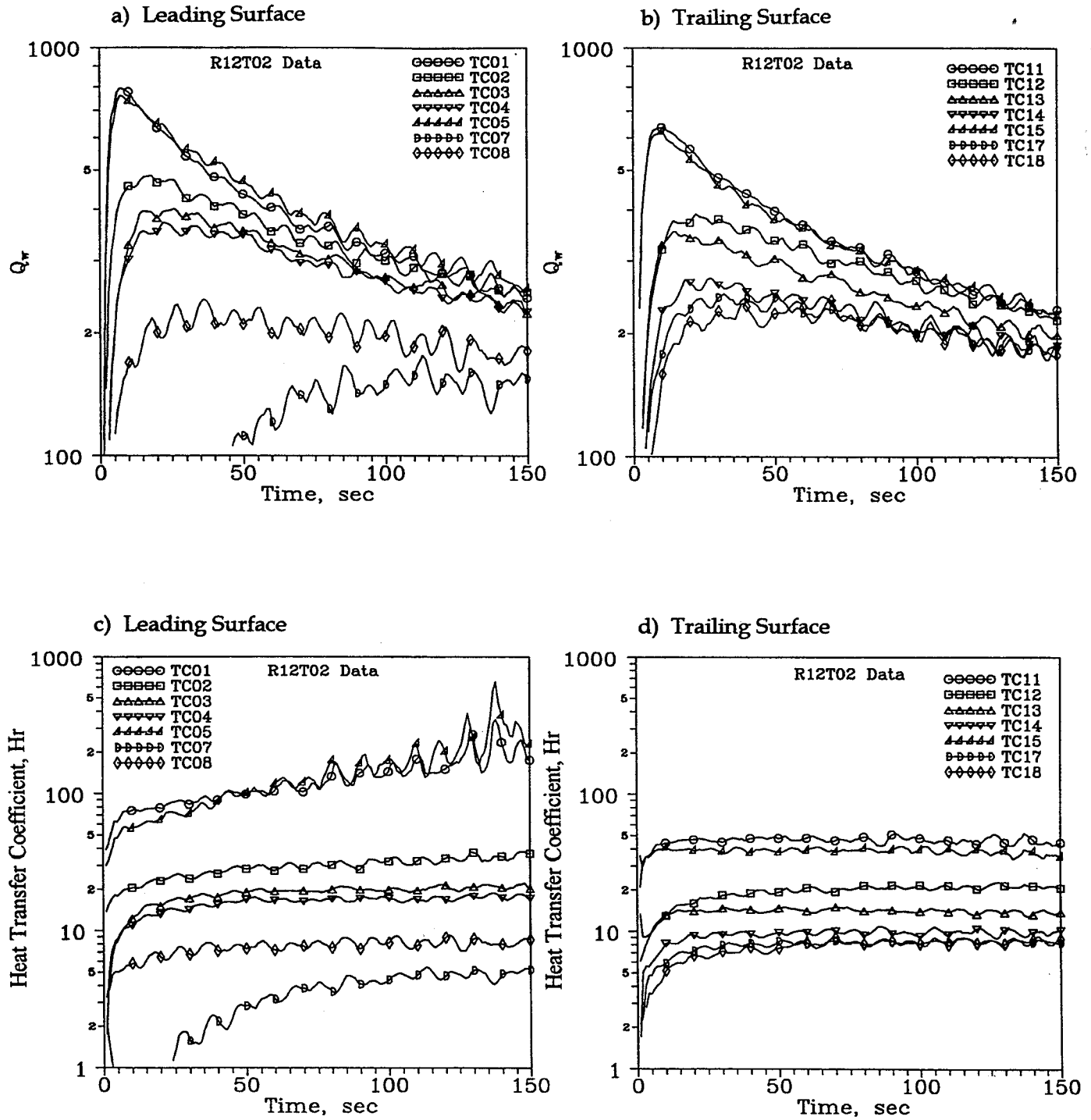


Figure 9.4-12. Results From Thermocouple Data for Liquid Crystal Test on Trailing Surface With  $\Omega = 750$  rpm.

REPORT DOCUMENTATION PAGE			Form Approved OMB No. 0704-0188	
Public reporting burden for this collection of information is estimated to average 1 hour per response, including the time for reviewing instructions, searching existing data sources, gathering and maintaining the data needed, and completing and reviewing the collection of information. Send comments regarding this burden estimate or any other aspect of this collection of information, including suggestions for reducing this burden, to Washington Headquarters Services, Directorate for Information Operations and Reports, 1215 Jefferson Davis Highway, Suite 1204, Arlington, VA 22202-4302, and to the Office of Management and Budget, Paperwork Reduction Project (0704-0188), Washington, DC 20503.				
1. AGENCY USE ONLY (Leave blank)		2. REPORT DATE May 1996		3. REPORT TYPE AND DATES COVERED Final Contractor Report
4. TITLE AND SUBTITLE Heat Transfer Experiments in the Internal Cooling Passages of a Cooled Radial Turbine Rotor			5. FUNDING NUMBERS  WU-505-62-10 C-NAS3-25952	
6. AUTHOR(S)  B.V. Johnson and J.H. Wagner				
7. PERFORMING ORGANIZATION NAME(S) AND ADDRESS(ES)  United Technologies Research Center Silver Lane East Hartford, Connecticut			8. PERFORMING ORGANIZATION REPORT NUMBER  E-10155	
9. SPONSORING/MONITORING AGENCY NAME(S) AND ADDRESS(ES)  National Aeronautics and Space Administration Lewis Research Center Cleveland, Ohio 44135-3191			10. SPONSORING/MONITORING AGENCY REPORT NUMBER  NASA CR-198472	
11. SUPPLEMENTARY NOTES  Project Manager, Kestutis C. Civinskas, Propulsion Systems Division, NASA Lewis Research Center, organization code 2760, (216) 433-3944.				
12a. DISTRIBUTION/AVAILABILITY STATEMENT  Unclassified - Unlimited Subject Category 07  This publication is available from the NASA Center for AeroSpace Information, (301) 621-0390.			12b. DISTRIBUTION CODE	
13. ABSTRACT (Maximum 200 words)  An experimental study was conducted (1) to experimentally measure, assess and analyze the heat transfer within the internal cooling configuration of a radial turbine rotor blade and (2) to obtain heat transfer data to evaluate and improve CFD procedures and turbulent transport models of internal coolant flows. A 1.15 times scale model of the coolant passages within the NASA LeRC High Temperature Radial Turbine was designed, fabricated of Lucite and instrumented for transient heat transfer tests using thin film surface thermocouples and liquid crystals to indicate temperatures. Transient heat transfer tests were conducted for Reynolds numbers of one-fourth, one-half, and equal to the operating Reynolds number for the NASA Turbine. Tests were conducted for stationary and rotating conditions with rotation numbers in the range occurring in the NASA Turbine. Results from the experiments showed the heat transfer characteristics within the coolant passage were affected by rotation. In general, the heat transfer increased and decreased on the sides of the straight radial passages with rotation as previously reported from NASA-HOST-sponsored experiments. The heat transfer in the tri-passage axial flow region adjacent to the blade exit was relatively unaffected by rotation. However, the heat transfer on one surface, in the transitional region between the radial inflow passage and axial, constant radius passages, decreased to approximately 20 percent of the values without rotation. Comparisons with previous 3-D numerical studies indicated regions where the heat transfer characteristics agreed and disagreed with the present experiment.				
14. SUBJECT TERMS  Radial turbine; Cooling; Internal cooling; Cooling passages; Heat transfer			15. NUMBER OF PAGES 118	
			16. PRICE CODE A06	
17. SECURITY CLASSIFICATION OF REPORT Unclassified	18. SECURITY CLASSIFICATION OF THIS PAGE Unclassified	19. SECURITY CLASSIFICATION OF ABSTRACT Unclassified	20. LIMITATION OF ABSTRACT	

National Aeronautics and  
Space Administration

**Lewis Research Center**  
21000 Brookpark Rd.  
Cleveland, OH 44135-3191

Official Business  
Penalty for Private Use \$300

POSTMASTER: If Undeliverable — Do Not Return